STUDIES ON BILATERAL CONTROL OF TELEOPERATOR UNDER TIME DELAY

TAKASHI IMAIDA

Laboratory for Dynamics in Aeronautics and Astronautics
Department of Aeronautics and Astronautics
Kyoto University

Acknowledgement

During the course of his thesis research, the author has received the valuable assistance from many people and organizations. In Particular, the author expresses his sincere gratitude to his thesis adviser, Professor Kei Senda of Kyoto University, for his patient guidance and constant encouragement.

The author would also like to express his thanks to Professor Kenji Fujimoto of Kyoto University and Professor Fumitoshi Matsuno of Kyoto University for their careful reviews and valuable suggestions.

The author also wishes to express his appreciation to Professor Yasuyoshi Yokokohji of Kobe University, Professor Tsuneo Yoshikawa of Kyoto University and Professor Kazuo Tsuchiya of Kyoto University for their guidance and suggestions.

The author is grateful to Dr. Shinya Aoi and Dr. Naoto Yokoyama for their valuable assistance and suggestions.

The author expresses as well his appreciation to Professor Mitsushige Oda of Tokyo Institute of technology, Mr.Toshitsugu Doi of Toshiba Corporation, Dr. Ryo Kikuue of Kyushu University, Mr. Yukihiro Iida at Kyoto University and the members of Laboratory for Dynamics in Aeronautics and Astronautics of Kyoto University for helpful discussions and their cooperation in the use of the robot facilities which allowed the author to carry out the experiments given in this thesis.

Finally, the author is grateful to his parents Yutaka and Kimiko Imaida, and his wife Kazuno for their support and encouragement.

Contents

Chapter 1

Introduction

1.1 Purpose of the thesis research

Bilateral teleoperation provides important force information on a remote environment to an operator. The time line of teleoperation originates in 1945, according to Sheridan, when Goertz built the first mechanically controlled master slave teleoperator [34] [9]. Continuous teleoperation in earth orbit or deep space by human operators on the earth's surface is seriously impeded by signal transmission delays imposed by limits on the speed of light and computer processing at sending and receiving stations and satellite relay stations.

In the following, some of the difficulties will be pointed out and the present status of investigation to overcome these difficulties will be described briefly.

1. *Problem of stability due to time delay*

   It is well known, that even small communication delays may destabilize the system with conventional bilateral control methods, such as symmetric position servo and force-reflecting servo [35]. Anderson and Spong [1] proposed a bilateral control law that maintains stability under communication delays by using the scattering theory. Niemeyer and Slotine [21] studied further on this problem.

   Besides the above well-known approaches, there are several other approaches. Leung *et al.* [17] proposed a bilateral controller for time delays based on the H∞-optimal control and μ-synthesis framework. Seo, *et al.* [33] proposed a bilateral teleoperator with an energy-bounding algorithm. Oboe, *et al.* [28],

Nuno, *et al.* [24] and Lee, *et al.* [16] dealt with this problem by using a proportional derivative (PD) controller.

However, there are some problems with these approaches. With the control law by Leung, we have to assume known environment impedance. With the control law by Oboe and Fiorini, they assume the slave arm is not contact with the environment and in free motion.

2. *Problem of Validity of bilateral control under long time delay of several seconds*
   As the time delay increases, the maneuverability of the teleoperator degrades. With the control law by Anderson, Spong, Niemeyer and Slotine, the apparent inertia of the teleoperator become large as the time delay increases. With PD-control, the damping gain become higher as the time delay increases.

   It has been assumed that bilateral control methods would not be effective when the time delay becomes longer than about 1 s [11][14][8]. Therefore, the bilateral control would not be applicable to in earth orbit teleoperation in which the round trip delay becomes several seconds [34].

3. *Difficulties of proper and quantitative evaluation of bilateral teleoperator performance under time delay*
   Ordinary transparency analysis, to compare the mechanical impedance felt by the operator to the impedance of the environment can not be applied to the bilateral teleoperator with time delay, because the effect of delay cannot be evaluated by this scheme.

4. *Low performance and maneuverability of bilateral control law with long time delay*
   The performance of bilateral control scheme which is stable under time delay is not adequate under long time delay, because of strong damping or inertia. Obviously there is a need to greatly improve the control laws to apply bilateral control to practical teleoperation under time delay.

The objective of the present thesis is to overcome these difficulties to make the theory of bilateral control applicable to practical systems, and demonstrate through real experiments. Namely;

1. to derive the stability condition of PD-based bilateral control law with any passive slave environment,
2. to demonstrate the validity of bilateral control using in-orbit robot systems,
3. to improve the PD-based bilateral control law by introducing relative damping, high pass filter and derive the stability condition,
4. to measure the performance of bilateral control law quantitatively,
5. to demonstrate the improvement of PD-based control law by simulation and real on-ground experiment

1.2 Scope of the thesis

This thesis is divided into six chapters.

Chapter 1 explains the problems on the bilateral control of teleoperator under time delay and the purpose of this thesis.

Chapter 2 develops the PD-based bilateral control law. The stability condition for any passive operator and environment is derived. The teleoperator is modeled as a electric circuit. The stability condition is derived using the stability criterion for two-terminal-pair networks.

Chapter 3 describes a bilateral teleoperation experiment with Engineering Test Satellite 7 (ETS-VII). A bilateral teleoperation experiment with ETS-VII was conducted on November 22, 1999. Round-trip time for communication between the National Space Development Agency of Japan ground station and the ETS-VII was approximately seven seconds. We constructed a bilateral teleoperator that is stable, even under such a long time delay. Several experiments, such as slope-tracing task and peg-in-hole task, were carried out. Task performance was compared between the bilateral mode and the unilateral mode with force telemetry data visually displayed on a screen. All tasks were possible by bilateral control without any visual information. Experimental results showed that kinesthetic force feedback to the operator is helpful even under such a long time delay, and improves the performance of the task.

Chapter 4 proposes PD controller with grounded and relative damping. First, we study a PD control law with relative damping gain and its stabilizing effect that

previously has not been studied quantitatively. A stable condition is derived with this PD-based controller with relative damping gain. Next, teleoperator performance by the PD control law with relative damping is evaluated and compared to PD control laws with only grounded damping using transparency analysis with a hybrid matrix. We showed that, the performance of the PD-based controller can be improved by introducing relative damping gain into the controller. As a controller design example, numerical simulations and 1-DOF experiments were conducted. Finally, peg-in-hole experiments and performance evaluations in realistic multi-DOF environments were conducted to demonstrate performance improvements by introducing the relative damping. A controller design that guarantees both stability and performance was achieved by iterating stable gain setting and performance evaluation.

Chapter 5 develops PD controller with high pass filter. The performance improvement by introducing a HPF into grounded damper in a PD-based teleoperator with time delay has been studied. First, we derived the stability condition of a PD-based controller with HPF. Second, performance evaluation was conducted using a hybrid matrix. As a result, we showed that introducing HPF into a PD-based controller improved the performance of the teleoperator. Third, to evaluate teleoperator performance, we conducted 1-DOF simulations and 2-DOF peg-in-hole experiments. The teleoperator performance was evaluated using these simulations and experiments.

Finally, chapter 6 provides a summary of results obtained from the thesis research.

Chapter 2

Stability of the PD-control teleoperator

2.1 Introduction

One of the well-known approaches to dealing with time delays in bilateral teleoperation is to use scattering transformation, as it was proposed by Anderson and Spong [1]. This approach was studied further by Niemeyer and Slotine [21], who introduced the notion of " wave variable. " Besides this wave-variable approach, there are several other approaches which are less popular. For example, Leung et al. [17] proposed a bilateral controller for time delays based on the H_∞-optimal control and the μ-synthesis framework. Oboe and Fiorini [28] dealt with the time-varying delay problem over the Internet by using a simple PD-type controller. However, there are many problems with their approach. With the control law by Anderson, Spong, Niemeyer and Spong, the apparent inertia become large when the time delay is long. With the control law by Leung, we have to assume known environment impedance. With the control law by Fiorini, they assume the master slave is not contact with the environment and in free motion. In this chapter, we derive the stability condition of PD-based bilateral controller with the concept of passivity of two-terminal-pair networks. First, the bilateral teleoperator is expressed by the hybrid matrix of two-terminal-pair networks. Then, the stability gain condition is derived with a stability criterion for two-terminal-pair networks (Llewellyn's criteria).

2.2 Dynamics of the teleoperator system

We studied the stability of a single degree of freedom teleoperation system composed of a pair of manipulators with a time delay as shown in Fig. 2.1. The springs and dampers in the "control" area of the dashed line box in Fig. 2.1 are not the real mechanisms. They are mechanical expressions of the control law. The block diagram of the teleoperator system is shown in Fig. 2.2. The dynamics of master and slave arms can be formulated as follows:

$$\tau_m + f_m = m_m \ddot{x}_m + b_m \dot{x}_m \tag{2.1}$$

$$\tau_s - f_s = m_s \ddot{x}_s + b_s \dot{x}_s \tag{2.2}$$

where x_m and x_s denote the respective positions of the master and slave arms, τ_m and τ_s are the actuator driving forces, and b_m and b_s represent the viscous coefficients of the driving mechanism. f_m is the force the operator applies to the master arm, and f_s is the force the slave arm exerts on the environment.

The generalized mass-dashpot-spring models that are used to represent the operator and the task are

$$\tau_{op} = m_{op} \ddot{x}_m + b_{op} \dot{x}_m + c_{op} x_m + f_m \tag{2.3}$$

$$f_s = m_w \ddot{x}_s + b_w \dot{x}_s + c_w x_s \tag{2.4}$$

where τ_{op} is the force generated by the operator's muscles. In the preceding equations, m, b, and c are the inertia, damping, and stiffness parameters. Subscript op is the operator and w is the task.

In this paper, the development of an analytical framework is complemented by the modeling of an actual teleoperator system. The modeling approach transforms the teleoperator system model into an electrical circuit. The teleoperator system can be replaced by an electric circuit, see Fig. 2.3. Replacing velocity and force in physical systems with current and voltage in circuits, the dynamic characteristics of the master and the slave arm, the operator, and the environment are represented by impedance Z_m, Z_s, Z_{op}, and Z_e, respectively. The V_m, V_s, V_{op}, I_m, and I_s correspond to $f_m, f_s, f_{op}, \dot{x}_m$, and $\dot{x}_s$, respectively. The U_m and U_s are the actuator drive forces τ_m and τ_s.

The Z_m, Z_s, Z_{op}, and Z_e are

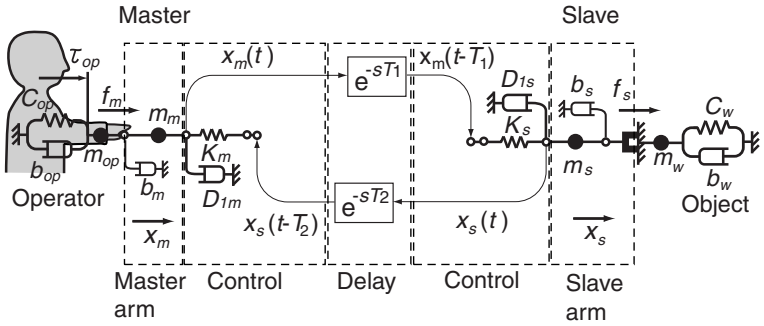

Figure 2.1: Bilateral master slave system with PD controller with only grounded damping gain.

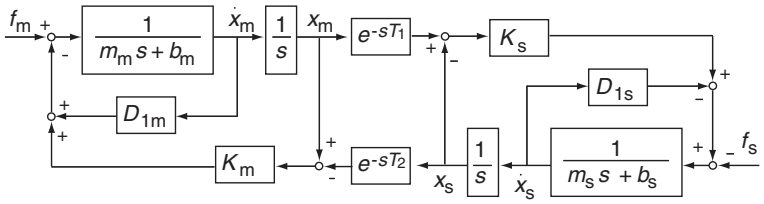

Figure 2.2: Block diagram of bilateral master slave system with PD controller with only grounded damping gain.

$$Z_m = \frac{m_m s^2 + b_m s}{s} \tag{2.5}$$

$$Z_s = \frac{m_s s^2 + b_s s}{s} \tag{2.6}$$

$$Z_{op} = \frac{m_{op} s^2 + b_{op} s + c_{op}}{s} \tag{2.7}$$

$$Z_e = \frac{m_w s^2 + b_w s + c_w}{s} \ . \tag{2.8}$$

Using these electric circuit representations, the teleoperator system is expressed by

$$\begin{bmatrix} V_m \\ V_s \end{bmatrix} = \begin{bmatrix} z_{11} & z_{12} \\ z_{21} & z_{22} \end{bmatrix} \begin{bmatrix} I_m \\ -I_s \end{bmatrix} \tag{2.9}$$

where $\boldsymbol{Z} = [z_{ij}]$ is the impedance matrix of the teleoperator [31].

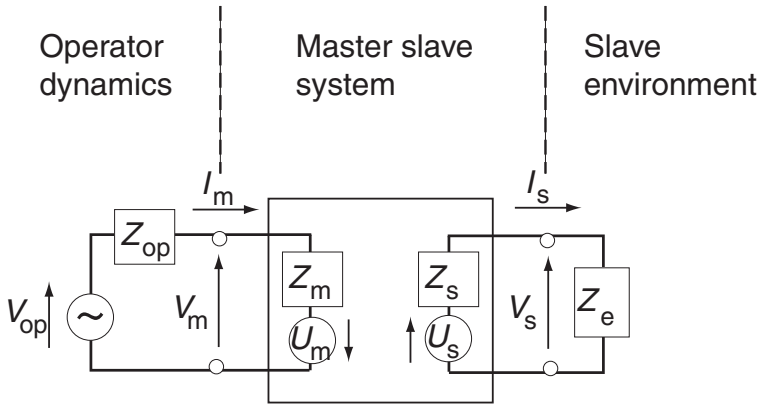

Figure 2.3: Electrical circuit expression of master-slave system, operator and environment.

2.3 A stability criterion for two-terminal-pair non-reciprocal networks (Llewellyn's criteria)

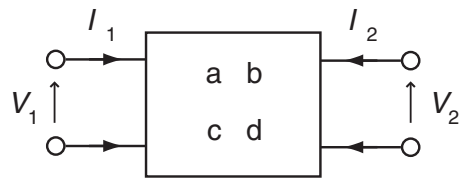

Figure 2.4: Two-terminal-pair network

With the notations of Fig.2.4, we have,

$$\begin{aligned} V_1 &= aV_2 - bI_2 \\ I_1 &= aV_2 - dI_2 \end{aligned} \tag{2.10}$$

Dividing, we obtain

$$Z_1 = \frac{aZ_2 + b}{cZ_2 + d} \tag{2.11}$$

$$\begin{aligned} Z_1 &= \frac{V_1}{I_1} \\ Z_2 &= -\frac{V_2}{I_2} \end{aligned} \tag{2.12}$$

We can also write

$$
\begin{aligned}
V_1 &= Z_{11}I_1 + Z_{12}I_2 \\
V_2 &= Z_{21}I_1 + Z_{22}I_2
\end{aligned} \tag{2.13}
$$

(2.10) and (2.13) yield

$$
\begin{aligned}
a &= \frac{Z_{11}}{Z_{21}} && \text{(14a)} \\
b &= \frac{Z_{11}Z_{22} - Z_{12}Z_{21}}{Z_{21}} && \text{(14b)} \\
c &= \frac{1}{Z_{21}} && \text{(14c)} \\
d &= \frac{Z_{22}}{Z_{21}} && \text{(14d)}
\end{aligned}
$$

so that

$$
Z_1 = \frac{Z_{11}Z_2 + (Z_{11}Z_{22} - Z_{12}Z_{21})}{Z_2 + Z_{22}} \tag{2.15}
$$

Letting $Z_1 = R_1 + jX_1, Z_2 = R_2 + jX_2$ and so on, we have

$$
R_1 = \frac{(R_2^2 + X_2^2)A + BR_2 + CX_2 + D}{(R_2 + R_{22})^2 + (X_2 + X_{22})^2} = \frac{H}{N^2} \tag{2.16}
$$

where

$$
\begin{aligned}
A &= R_{11} \\
B &= 2R_{11}R_{22} - R_{12}R_{21} + X_{12}X_{21} \\
C &= 2R_{11}X_{22} - R_{12}X_{21} - X_{12}R_{21} \\
D &= R_{22}(R_{11}R_{22} - R_{12}R_{21}) \\
&\quad -X_{22}(R_{12}X_{21} + X_{12}R_{21}) + R_{22}X_{12}X_{21} + R_{11}X_{22}^2
\end{aligned} \tag{2.17}
$$

The expression

$$
H = AR_2^2 + AX_2^2 + BR_2 + CX_2 + D \tag{2.18}
$$

can be written

$$
H = A(R_2 + \frac{B}{2A})^2 + A(X_2 + \frac{C}{2A})^2 + \frac{4AD - B^2 - C^2}{4A} \tag{2.19}
$$

We are interested in the values of R_1 for which $R_2 \geq 0$. The denominator of (2.16) is always positive, so that we need only consider (2.18). For H =constant, (2.18) represents, for a fixed frequency, a circle in a plane above the $R_2 - X_2$ plane at a distance that is equal to the constant H value. If the frequency varies and H takes all values ≥ 0 for $R_1 \geq 0$, (2.18) represents a moving paraboloid of revolution. This is also evident from (2.19). Since $R_2 \geq 0$, only the values of the paraboloid that correspond to the shaded area in Fig.2.5 can be used. For $R_2 = 0$,(2.18) and (2.19) become:

$$H = AX_2^2 + CX_2 + D \tag{2.20}$$

$$H = A(X_2 + \frac{C}{2A})^2 + \frac{4AD - C^2}{4A} \tag{2.21}$$

$$H = AX_2^2 + CX_2 + D \tag{2.22}$$

$$H = A(X_2 + \frac{C}{2A})^2 + \frac{4AD - C^2}{4A} \tag{2.23}$$

This is the equation of the parabola cut out from the paraboloid by the $H - X_2$ plane (See Figs. 2.6 and 2.7). It is evident that the vertex of this parabola has to stay above the X_2 axis. This means that

$$\begin{aligned} A &\geq 0 \\ 4AD - C^2 &\geq 0 \end{aligned} \tag{2.24}$$

With the use of (2.17), we obtain

$$\begin{gathered} R_{11} \geq 0 \\ R_{22} \geq 0 \\ 4(R_{11}R_{22} + X_{12}X_{21})(R_{11}R_{22} - R_{12}R_{21}) - (R_{12}X_{21} - R_{21}X_{12})^2 \geq 0 \end{gathered} \tag{2.25}$$

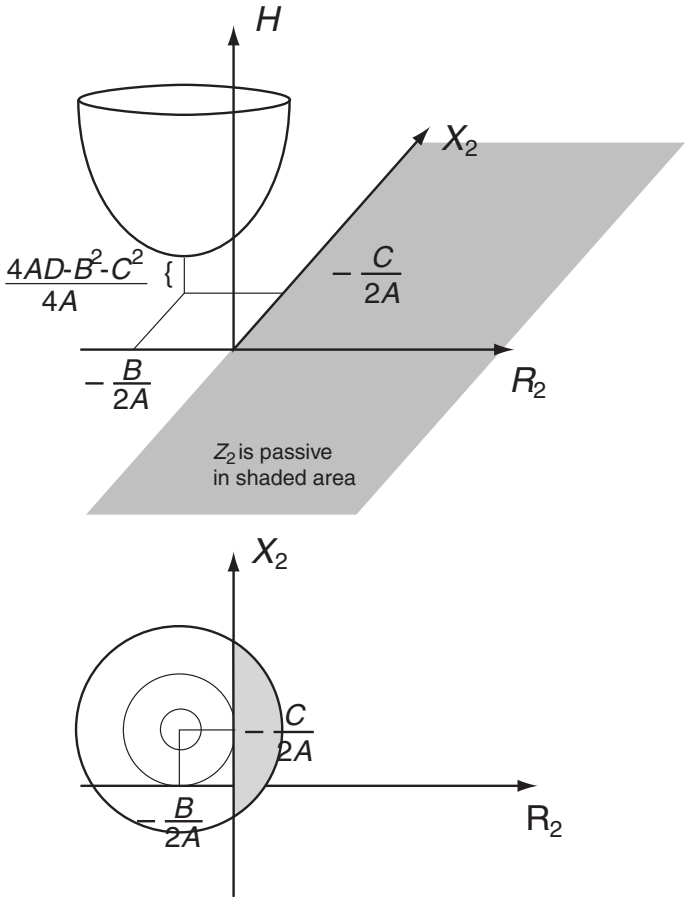

Figure 2.5: Geometric representation of (2.18) and (2.19) according to Gewertz.

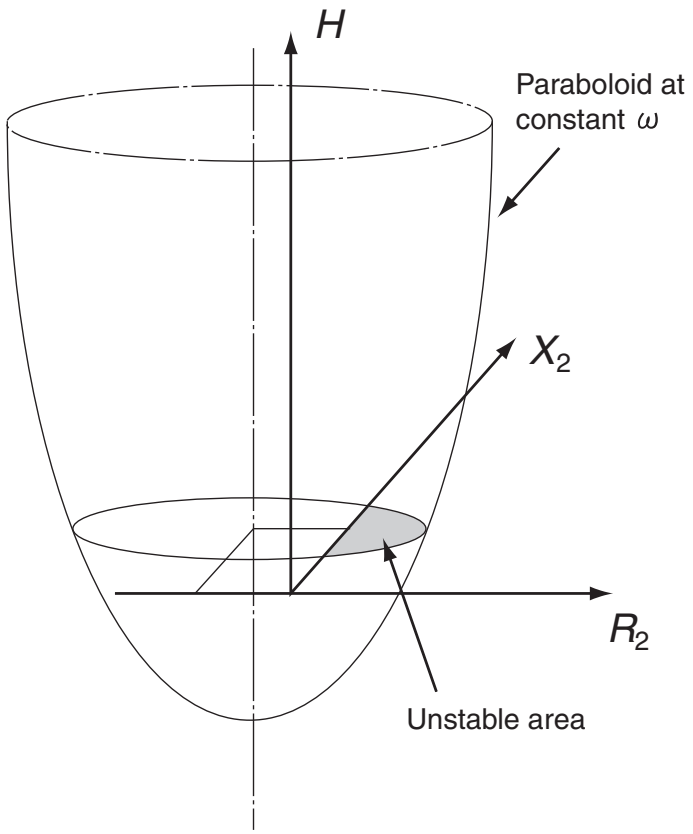

Figure 2.6: Example of paraboloid with unstable area. Unstable area is shown in the shaded area.

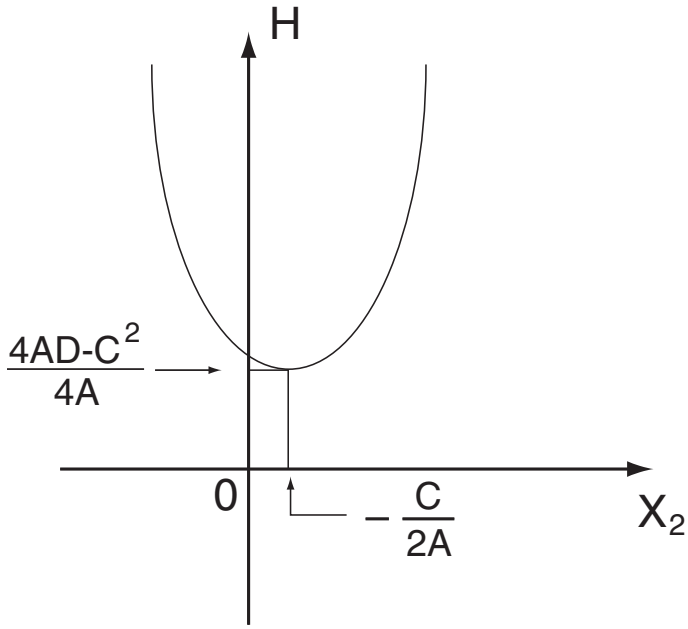

Figure 2.7: Parabola cut out of the paraboloid by the $H - X_2$ plane.

2.4 Stability of PD-based bilateral controller with grounded damping

We derive bilateral PD controller stability with only grounded damping. The PD controller is expressed by the following equations:

$$\tau_m = -K_m(x_m(t) - x_s(t - T_2)) - D_{1m}\dot{x}_m \tag{2.26}$$

$$\tau_s = K_s(x_m(t - T_1) - x_s(t)) - D_{1s}\dot{x}_s \tag{2.27}$$

where K_m and K_s are position gains and D_{1m} and D_{1s} are grounded damping gains. T_1 and T_2 are time delays from the master to the slave and from the slave to the master, respectively. The physical interpretation of this controller is shown in Fig. 2.1.

The impedance matrix of the teleoperator is as follows [3]:

$$\boldsymbol{Z} = \begin{bmatrix} m_m s + b_m + D_{1m} + \frac{Km}{s} & K_m e^{-sT_2}/s \\ K_s e^{-sT_1}/s & m_s s + b_s + D_{1s} + \frac{Ks}{s} \end{bmatrix}. \tag{2.28}$$

We derived stability for any passive terminations by applying Llewellyn's stability criteria (2.25) [2] [18] to (2.28). The teleoperator is stable for all passive terminations if the following conditions are satisfied for all frequencies:

$$D_{1m} + b_m \geq 0 \tag{2.29}$$

$$D_{1s} + b_s \geq 0 \tag{2.30}$$

$$(D_{1m} + b_m)(D_{1s} + b_s) \geq \frac{K_m K_s}{\omega^2} \sin^2 \frac{\omega(T_1 + T_2)}{2} \ . \tag{2.31}$$

Rewriting the right-hand side of (2.31), using the relationship $\sin(\omega(T_1 + T_2)/2) < \omega(T_1 + T_2)/2$, $\forall \ \ \omega, T_1, T_2 > 0$, we get the following inequality:

$$(D_{1m} + b_m)(D_{1s} + b_s) \geq \frac{K_m K_s (T_1 + T_2)^2}{4} \ . \tag{2.32}$$

If we consider a symmetrical system, i.e., $K_m = K_s = K, D_{1m} = D_{1s} = D_1, T_1 = T_2 = T, b_m = b_s = b$, then (2.31) and (2.32) become (2.33) and (2.34), respectively.

$$(D_1 + b)^2 \geq (\frac{K}{\omega} \sin \omega T)^2 \tag{2.33}$$

$$D_1 + b \geq KT \tag{2.34}$$

2.5 Conclusion

In this chapter, we analyzed the stability of PD control bilateral teleoperator. Stability condition was derived. With the gain settings of the proposed stability condition, the teleoperator is stable with any passive operator and any passive slave side environment. In the analysis, we assume the time delay is constant and known value.

Chapter 3

Ground-Space Bilateral Teleoperation of ETS-VII Robot Arm by Direct Bilateral Coupling Under 7-s Time Delay Condition

3.1 Introduction

Bilateral control provides important force information on a remote environment to an operator. It is well known, however, that even small communication delays may destabilize the system with conventional bilateral control methods, such as symmetric position servo and force-reflecting servo [35]. Anderson and Spong [1] proposed a bilateral control law that maintains stability under communication delays by using the scattering theory. Niemeyer and Slotine [21] studied further on this problem. It has been assumed, however, that bilateral control methods would not be effective when the time delay becomes longer than about 1 s. For example, Kim et al. [11], who conducted an experiment of peg-in-hole tasks using a force-reflecting servo under a time-delay condition, described it as, " $\cdots$However, this force-reflection technique can be utilized only up to an approximately 0.5- to 1-s communication time delay, since a long time delay in the force feedback loop causes the system to be unstable."Lawn et al. [14] performed one-degree-of-freedom (DOF) tasks such as pushing and positioning with time delay. They used a bilat-

eral control law based on the scattering theory and reported, “ The passivity-based laws were not tested for delays of 1 s since their performance was very poor due to extremely low stiffness. ”Hirzinger et al. [8] mentioned that, “ In ROTEX, the loop delays varied from 5-7 s. Predictive computer graphics seems to be the only way to overcome this problem. ”As Penin et al. [29], [30] did, we also summarized previous works on teleoperation with force feedback under certain communication time delays in Table 3.1 [1]. All of them showed the results of real experiments. These previous works can be divided into two groups: 1) direct bilateral teleoperation without any models of the remote site and 2) model-based teleoperation with pseudo force feedback from a local model of the remote environment. From the table, it seems that when the time delay is longer than about 1 s, the model-based approach would be the only solution. However, we have been doubtful about this “ 1-s limitation ” for the following reasons.

- Some of the observations came from the results using a conventional bilateral controller, for which stability is not guaranteed under the time-delay condition. Probably, 1 s would be the limitation to stabilize such an unstable system by human operators.

- The bilateral control based on the scattering theory guarantees the stability of the system for any time delay. However, it loses its stiffness and tends to be sticky as the time delay becomes large [22]. Again, 1-2 s would be the limitation for an operator to maneuver such a system comfortably [14]. However, the scattering theory is not the only solution to the time-delay problem, and some other types of bilateral controller can also guarantee the stability.

Instead of exactly drawing the limitation line at 1 s, our claim is, in a sense, quite natural as follows. The time-delay limitation depends on the difficulty of the task. Even if the time delay becomes longer than 1 s, some tasks could be performed by direct bilateral teleoperation. Actually, Ferrell [4] investigated the effect of time delays longer than 1 s in bilateral control. Although the tasks he conducted were simple positioning with force feedback, he tested several time delays up to 3 s. In this paper, the results of a ground-space teleoperation experiment using a robot arm mounted on the Engineering Test Satellite 7 (ETS-VII) are shown. The experiment

Table 3.1: AMOUNT OF TIME DELAY IN PREVIOUS WORKS ON TELEOPERATION WITH FORCE FEEDBACK

	Author(s)	Model -based?	Time Delay for Round Trip	Feature
[1]	Anderson & Spong(1989)	No	80ms,400ms,4s	Scattering Theory
[21]	Niemeyer & Slotine(1991)	No	1s	Wave Variables
[11]	Kim *et al.*(1992)	No	1s	Shared Compliant Control
[14]	Lawn & Hannaford(1993)	No	up to 1s	Comparison between Scattering Theory and Others
[12]	Kosuge *et al.*(1996)	No	1.4s	Virtual Time Delay
[28]	Oboe & Fiorini(1998)	No	320ms	PD-type
[16]	Lee *et al.*(2006)	No	1s,3s	PD-type
[27]	Nuno *et al.*(2009)	No	600ms	PD-type
[13]	Kotoku(1992)	Yes	1s	Predictive Display with Force Feedback
[5]	Funda *et al.*(1992)	Yes	3s	Teleprogramming
[36]	Tsumaki *et al.*(1996)	Yes	5s	Velocity/Damping Control

was conducted on November 22, 1999. Round-trip time for communication between the National Space Development Agency (NASDA) of Japan ground station and the ETS-VII was between 6-7 s. We constructed a bilateral teleoperator using a proportional derivative (PD)-type controller that is stable even under such a long time delay. Several tasks, such as slope tracing and peg-in-hole, were carried out. All the tasks could be completed by direct bilateral control, even without using visual information. The experimental results demonstrate that kinesthetic force feedback to the operator is helpful, even under such a long time delay. To the best of the authors ' knowledge, there have not been any studies on ground-space teleoperation with direct force feedback yet. We would like to emphasize that what we used in the experiment was not the simulated force feedback based on a model of the remote environment, but the real force feedback from the slave side.

3.2 Overview of the experiment

3.2.1 Purpose of the Experiment

In this section, the purpose of the experiment is summarized. A more detailed description of the experiment can be found in Section IV. We focus on the following three aspects:

1. check the basic performance of the PD-type bilateral controller under the condition of 5-7 s time delay;
2. check the performance of various tasks:
   (a) accuracy of applied forces commanded from the ground (pushing task);
   (b) accuracy of recognizing constraint surface shapes (slope-tracing task);
   (c) accuracy of recognizing contact state transitions (peg-in-hole task);
   (d) accuracy of recognizing unknown constraint directions (slide-handle task);
3. investigate the cognitive aspect and the skill level of the operators.

3.2.2 Experimental System

Fig. 3.1 shows the experimental robot system on the ETS-VII. It has a 6-DOF 2-m long robotic arm, which can be controlled remotely from the ground station. Fig. 3.2 illustrates the task board on the ETS-VII, which contains several experimental facilities used in the experiment. Fig. 3.3 shows the configuration of the experimental system. The command signal from the master handle is transmitted to the ETS-VII through the NASDA 's operation equipment at a time interval of 250 ms. The controller of the master handle receives the telemetry data from the satellite, also at a time interval of 250 ms. Fig. 3.4(a) shows the overview of the ground control station. A 2-DOF force-feedback joystick (Impulse Engine 2000 by Immersion Co., San Jose, CA) shown in Fig. 3.4(b) was used as the master handle. A six-axis force/torque sensor (MICRO 5/50 by BL Autotech, Ltd., Kobe, Japan) is attached to the joystick so that the force applied by the operator can be measured. The maximum force that can be generated at the top of the master handle is approximately 3.2 N, and the stroke is approximately 15 cm in both x

and y directions. The master handle is controlled by a target computer (Pentium II 450 MHz) with the VxWorks realtime operating system, and its sampling time is 1 ms.

3.2.3 Modified Bilateral Controller

The PD-type bilateral controller discussed in Section II assumes a grounded damper at both master and slave sides. Due to the limitation of the on-board arm controller specification of the ETS-VII, however, we could not implement such a grounded damper at the slave side. Instead, we reluctantly used a compliant controller where the damping term is relative, as shown in Figs. 3.5 and 3.6. Let this relative damping gain be denoted by D'_s. We derived the stability condition for this modified controller. To guarantee the stability, the following inequality must be satisfied for all $\omega > 0$ and at $\omega \to 0$:

$$(D_m+b_m)D'_s \geq \frac{1}{2}(\sqrt{\frac{K_m^2K_s^2}{\omega^4}+\frac{K_m^2D_s'^2}{\omega^2}}-(\frac{K_mK_s}{\omega^2}\cos\omega(T_1+T_2)+\frac{K_mD'_s}{\omega}\sin\omega(T_1+T_2))). \tag{3.1}$$

The derivation of this condition is described in Appendix B. Unfortunately, the condition is not simple like (5), and we need to check the above inequality for all frequencies. Fig. 3.7 illustrates left and right sides of this inequality with appropriate controller gains. One can see that checking at low frequencies, including , $\omega \to 0$is sufficient. Table 3.2 shows the gains that satisfy this condition.

Although we know that the modified controller can ensure the system stability for any passive environment and operator dynamics by applying enough damping gain, shown in Table 3.2, we could not increase the damping gain at the master side large enough due to the hardware limitation of the master handle (mainly due to the low encoder resolution). The largest damping gain that could be achieved on our master handle was $D_m = 10$ Ns/m, which is far below the required value $D_m = 90$ Ns/m by the stability condition.

Since we know that the passivity condition is sometimes conservative, we studied whether or not we could perform the experiment with $D_m = 10$ Ns/m as follows. First, we modeled the operator and the environment by linear models (spring, mass, and damper). Next, we simulated the overall system response using representative

parameters of the operator and the environment (corresponding to free motion and hard contact). Then, we confirmed that the system is stable, even with $D_m = 10$ Ns/m. Of course, this confirmation is not perfect, because we did not check all possible combinations of operator dynamics and environments. To make sure that this underdamped controller is acceptable, we checked what parameter combination makes the overall system unstable with $D_m = 10$ Ns/m. As a result, we found that the system becomes unstable only when the operator 's mass is more than 1.0 $\times 10^6$ kg, which is an unrealistic value. From the results of these considerations, we concluded that the system is stable, even with $D_m = 10$ Ns/m under the condition of the planned experiments and decided to perform the experiments with this underdamped controller. In the experimental setup, the command signal and the telemetry data is transmitted at a 250-ms time interval. However, control signals for the master handle and the robot joints are updated at a higher sampling rate (about 1000 Hz). The stability analysis mentioned above was based on the framework of continuous time systems. It is one of our future works to analyze the system stability in the framework of discrete time systems with multisampling rate.

3.2.4 Specific Conditions of the Space Experiment and Preliminary Experiment on the Ground

Specific conditions of our experiment are as follows.

- Any hardware and software trouble that leads to system malfunction is not permissible. The reliability of the experimental system must be strictly assured.

- The experiment time assigned to us was limited, and it was approximately 240 min in total. The assigned time was divided into six slots called " path, " corresponding to the duration time (about 40 min) when the tracking data relay satellite (TDRS) on the geostationary orbit is visible from the ETS-VII (ETS-VII itself is orbiting around the earth, 550 km above the ground). Since we need about 10 min to open and close the experiment sessions (e.g., resuming/returning the robot from/to the standby condition), a series of experiments must be completed within 30 min.

Table 3.2: GAINS THAT SATISFY THE STABILITY CONDITION

Slave velocity gain: D'_s	3795 Ns/m
Slave position gain: K_s	200 N/m
Master velocity gain: D_m	90 Ns/m
Master position gain: K_m	40 N/m

- The command signals to the robot are always monitored and checked by the NASDA operation equipment, and the maximum operating speed of the robot tip is restricted to 2.0 mm/s for safety reasons.

To check the operation of our experimental system, we performed simulation experiments over the Internet, connecting our master controller in Kyoto and the robot simulator, which was developed by NASDA, in Tsukuba before the real space experiment was carried out. The distance between Tsukuba and Kyoto is about 600 km. The NASDA simulator can simulate the motion of the robot arm mounted on the ETS-VII. However, we could simulate only the tasks on the tracing slope, and not the peg-in-hole task nor the slide-handle task, because the NASDA simulator could not handle the complex contact dynamics of these tasks. Therefore, the preliminary experiment could not cover all tasks planned in the real experiment. This was one of the limitations of the preliminary experiment on the ground. In addition, it was also difficult to simulate the real communication link exactly in the preliminary experiment, since the connection was established over the Internet.

The maximum speed of 2.0 mm/s is very slow, compared with normal operations on the ground. Theoretically speaking, there is no relationship between operating speed and stability. Practically speaking, however, the operator must move the master arm very slowly or take “ move and wait ” strategy under such a long time-delay condition.

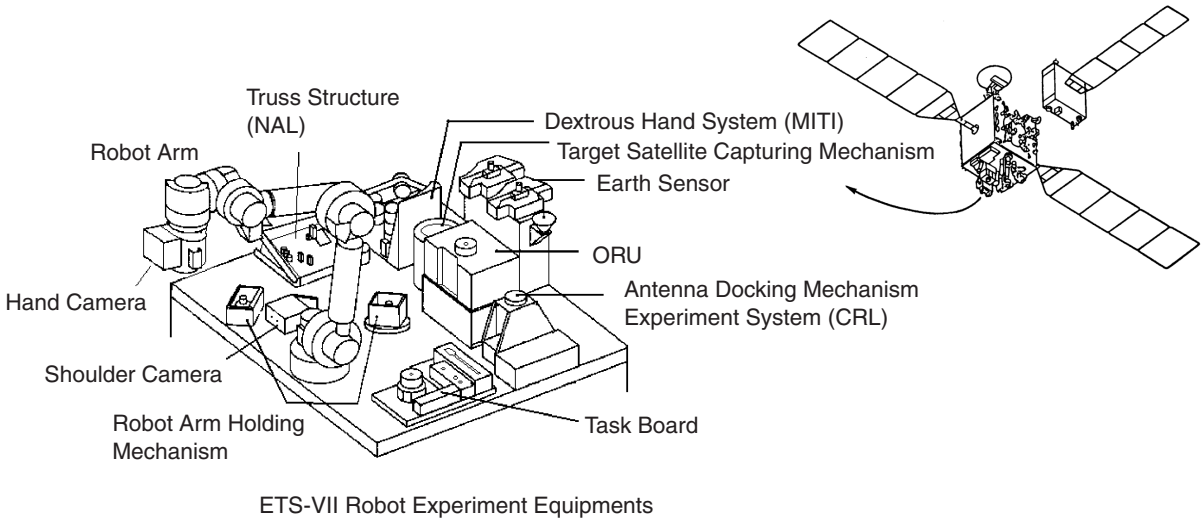

Figure 3.1: Robot system on ETS-VII.

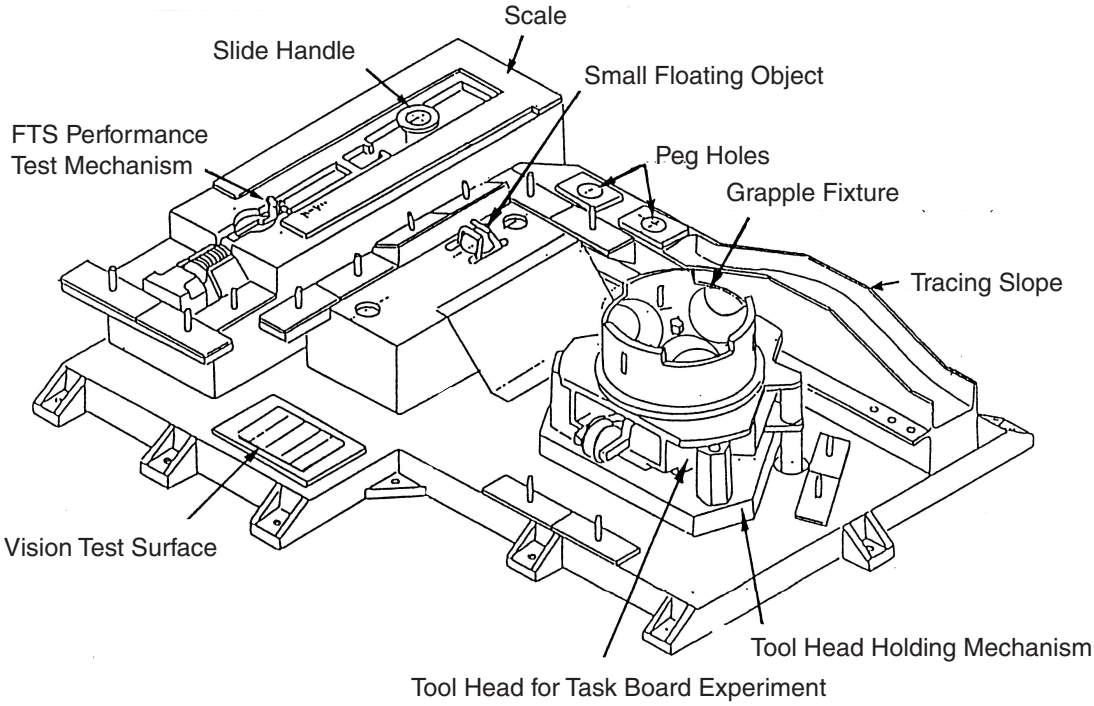

Figure 3.2: Task board on ETS-VII.

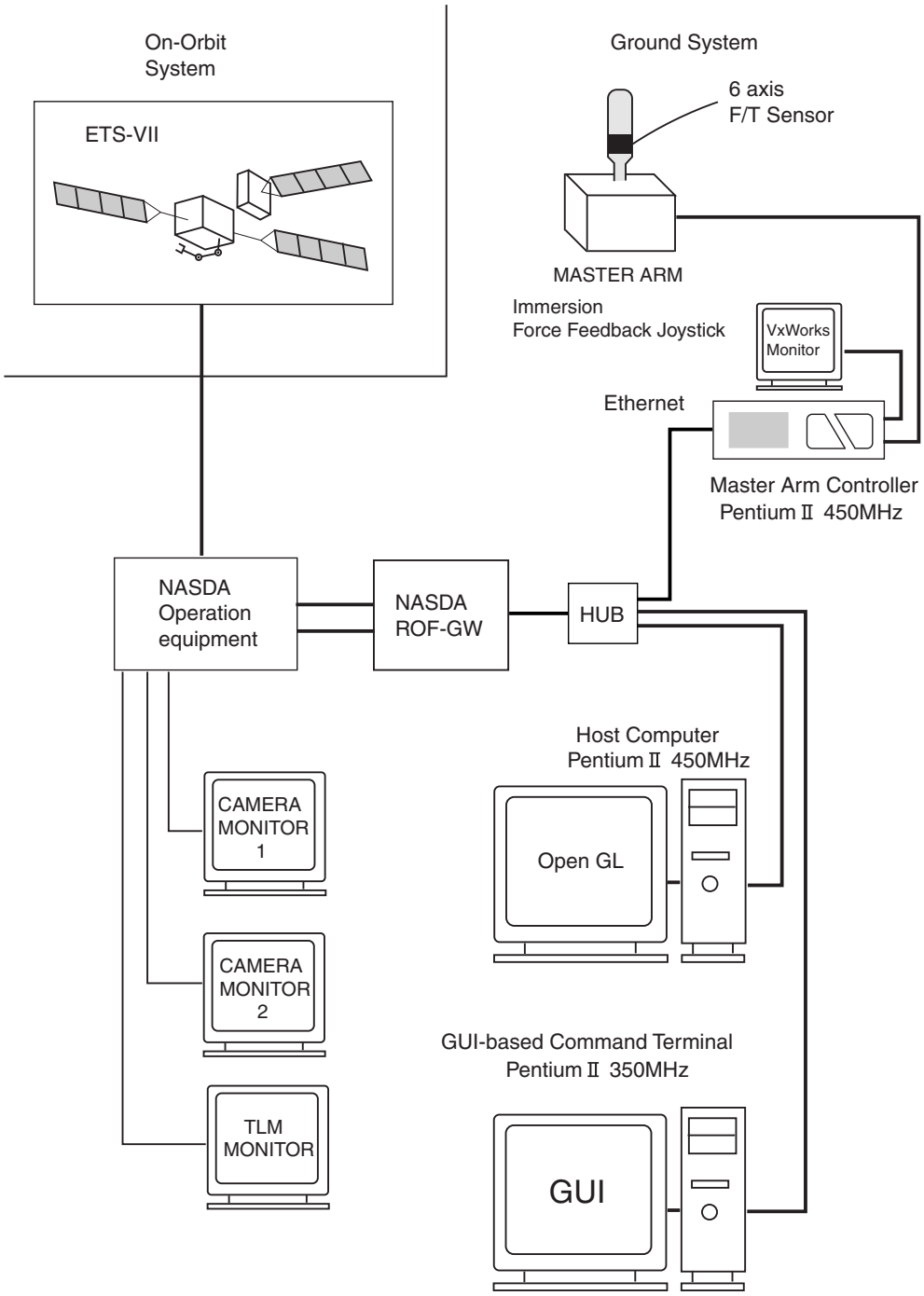

Figure 3.3: Configuration of the experimental system.

(a) control station

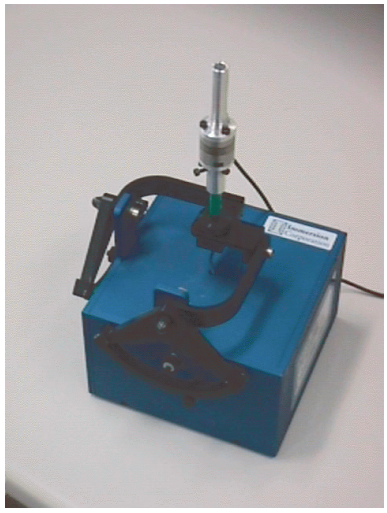

(b) master handle

Figure 3.4: Experimental system.

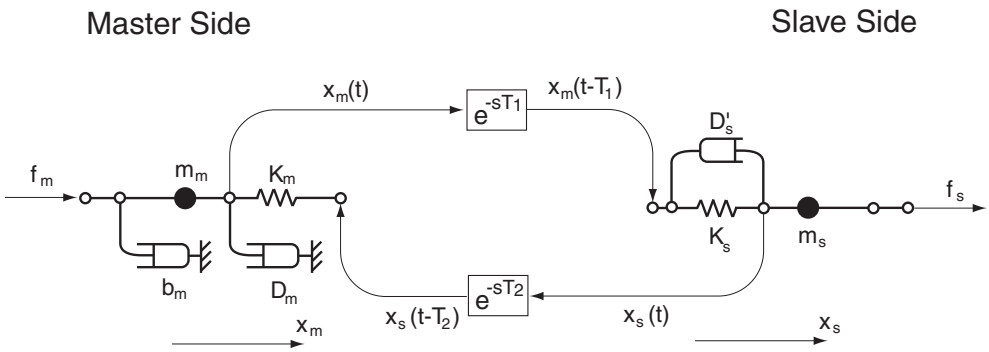

Figure 3.5: Modified bilateral controller.

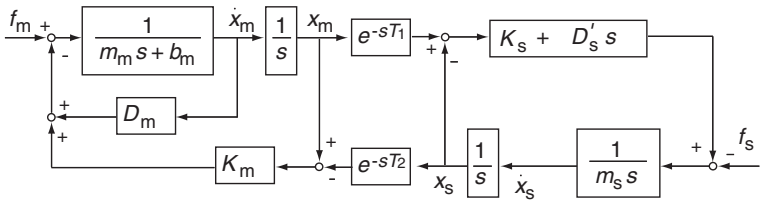

Figure 3.6: Block diagram of modified bilateral controller.

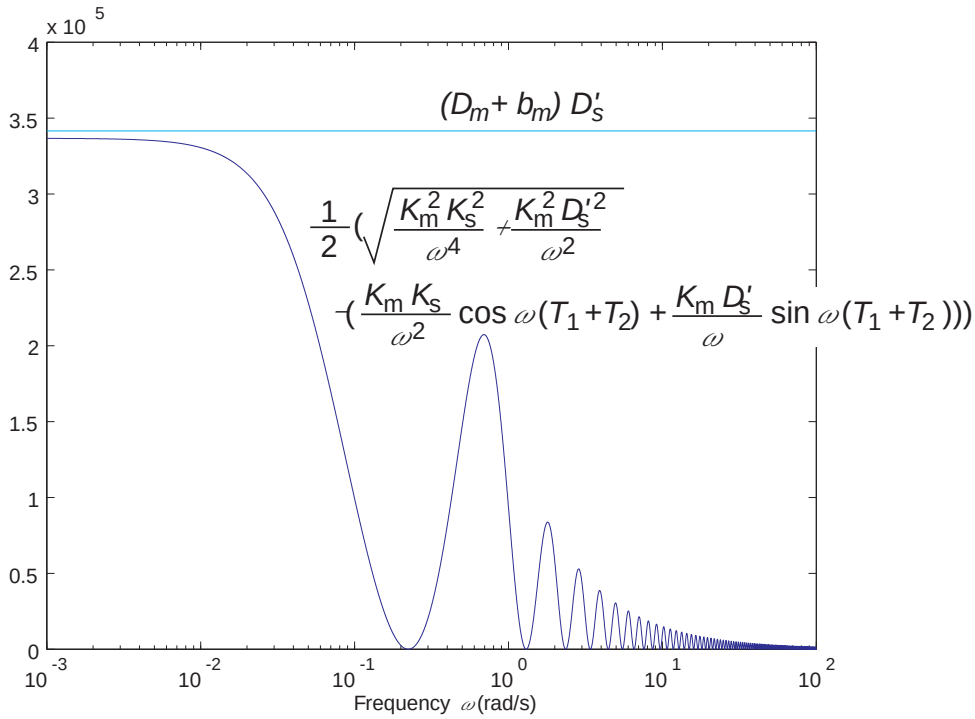

Figure 3.7: Plot of stability condition.

3.3 Detailed contents of the experiment

In this section, each experiment task will be described in detail. During the experiment, one can monitor two real images taken from the shoulder camera and the hand camera as shown in Figs. 3.8 and 3.9, respectively. As we describe in the following sections, the operators need to estimate the shape of the constraint surface, the instant of contact state transitions, and the direction of the constraint in the tasks. Since the operators must estimate those things without monitoring real scenes, we placed two masking boards in the control station so that these two real images are shielded from the operator 's position, as shown in Fig. 3.4(a). In the following tasks, only the computer screen showing telemetry force data or nothing (depending on the experimental conditions) is visible to the operators.

3.3.1 Pushing Task

In the pushing task, the operator brings the tip of the robot arm into contact with the surface of the tracing slope (the location of the tracing slope is shown in Fig. 3.2). Then, he applies a rectangle force pattern 5N $\rightarrow$ 15N $\rightarrow$ 5N downwards without moving the arm in tangential directions. Since the force-scaling factor between master and slave is five, the force pattern that the operator should actually apply to the master is 1N $\rightarrow$ 3N $\rightarrow$ 1N. Settling time and errors were evaluated in the following three cases.

Case B+T (bilateral mode + force telemetry graph): The operator can feel force feedback from the master handle. At the same time, he can monitor the telemetry force data displayed on the screen, as shown in Fig. 3.10.

Case B (bilateral mode): The operator must operate with force feedback alone and no visual information is provided.

Case U+T (unilateral mode + force telemetry graph): No force feedback is provided from the master handle. The telemetry force data on the screen is the only information fed back to the operator.

3.3.2 Slope-Tracing Task

In the slope-tracing task, the operator lets the robot arm contour the sinusoidal slope, while exerting a constant force (5 N). As shown in Fig. 3.8, a peg is attached to the tip of the robot arm. The starting point, which was not told to the operator, was chosen among points A, B, and C, shown in Fig. 3.11. The operator was asked to move the arm down to the surface until the tip of the arm comes into contact with the surface, then to move 150 mm left, and to move back to the starting point. Depending on the starting point, the resultant trajectory will be one of the patterns shown in Fig. 3.12.

In order to compare the task performance under equal conditions, the operators were asked to complete this task preferably in three minutes and within the maximum of four minutes. The following two cases were tested:

Case B+T (bilateral mode + force telemetry graph);

Case U+T (unilateral mode + force telemetry graph).

Completion time and force errors were evaluated. In addition, the operator had to answer which starting point was selected after he finished each trial.

3.3.3 Peg-in-Hole Task

In the peg-in-hole task, the robot arm was initially placed at point D in Fig. 3.11, 30 mm left from the peg hole. The same peg used in the slope-tracing task was used again in this task. The diameter of the peg is 18 mm, and the hole has 0.4 mm clearance. For smooth insertion, the peg tip is rounded and the hole is chamfered. The operator brings the peg into contact with the top surface, slides it horizontally until it reaches the hole entrance (10 mm below point E), and then inserts the peg into the hole. The operator was asked to avoid lateral force as much as possible when inserting the peg. He was also asked to identify the transition of the contact state, i.e., the instants when the peg starts to enter the hole and when it reaches the bottom of the hole, respectively. The following three cases were tested:

Case B+T (bilateral mode + force telemetry graph);

Case B (bilateral mode);

Case U+T (unilateral mode + force telemetry graph).

Completion time, the amount of lateral force during the insertion, and accuracy of recognizing the transition of the contact state were evaluated. In fact, we were not sure if this peg-in-hole task was possible under such a long time delay.

For the above three tasks (pushing, tracing, and peg-in-hole), two-dimensional (2-D) horizontal motions of the master handle were assigned to 2-D translational motions of the robot arm in the vertical plane across the contouring slope and peg holes. The orientation of the arm and the remaining translational component were fixed by the on-board position controller.

3.3.4 Slide-Handle Task

In the slide-handle task, the slide handle in the slide guide, which can be seen in Fig. 3.2, was used. 2-D horizontal motions of the master handle were assigned to 2-D translational motions in the horizontal plane, including the sliding direction. To make the sliding direction unknown to the operator, a certain amount of rotational coordinate transformation around the normal axis of the horizontal plane was introduced.

At the initial stage, the peg attached to the tip of the robot arm was already inserted in the hole of the slide handle, and this handle was placed at the center of the slider guide. The operator should estimate the unknown sliding direction by probing the master handle. Then, he should move the robot to one end of the slider guide, then to the other end, and finally move back to the center. The operator was asked to minimize lateral forces (perpendicular to the sliding direction) as much as possible when moving the slide handle.

The operator should complete the task within three minutes. To complete the task, he must estimate the correct sliding direction and recognize the end of the slider guide as fast as possible. After the task, the operator should report his estimation of the sliding direction. The following three cases were tested:

Case B+T (bilateral mode + force telemetry graph);

Case B (bilateral mode);

Case U+T (unilateral mode + force telemetry graph).

Completion time, the amount of lateral force during the sliding motion, and accuracy of the estimated sliding direction were evaluated. Here, we were also uncertain whether or not this task was possible under such a long time-delay condition before the experiment.

3.3.5 Skill Level and Other Cognitive Factors

Due to the limited time assigned to us, most of the experiments were carried out by a single operator, who was accustomed to the system operation using the master handle. To investigate the effect of skill level, two other operators conducted some tasks. One was a NASDA operator, who had been accustomed to the operation of the ETS-VII robot arm by NASDA 's teleoperation facilities, but was not familiar with the master handle used in this experiment. The other one was a novice operator, who had not been trained with any device, but had a background of teleoperation.

To investigate cognitive factors, such as mental load and their attention points during the tasks, the operators were asked to fill out a questionnaire after the experiment.

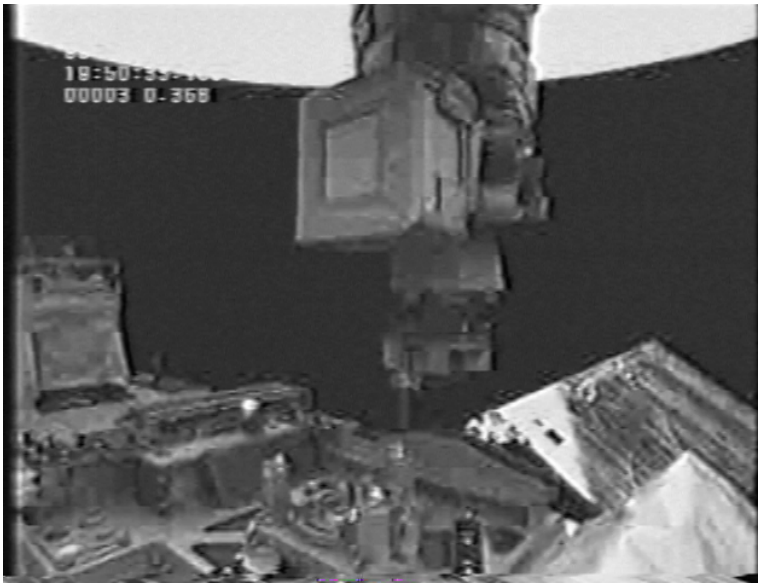

Figure 3.8: Shoulder camera image (slope-tracing task).

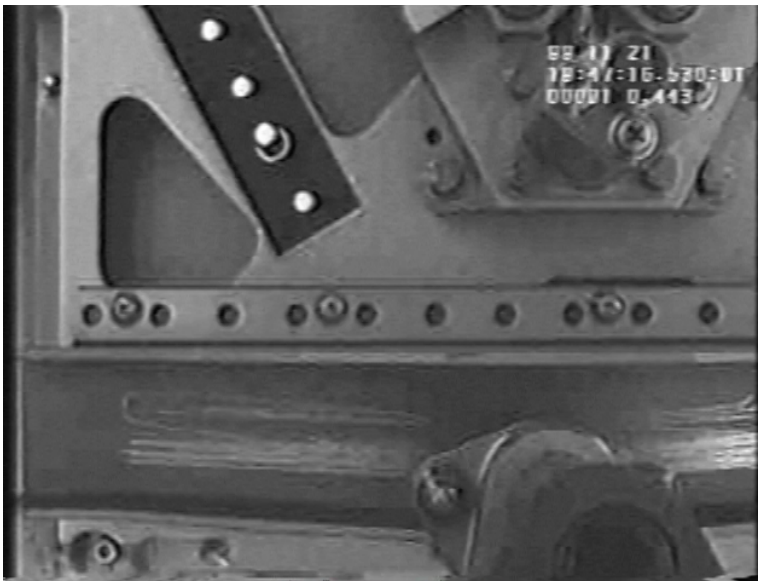

Figure 3.9: Hand camera image (slope-tracing task).

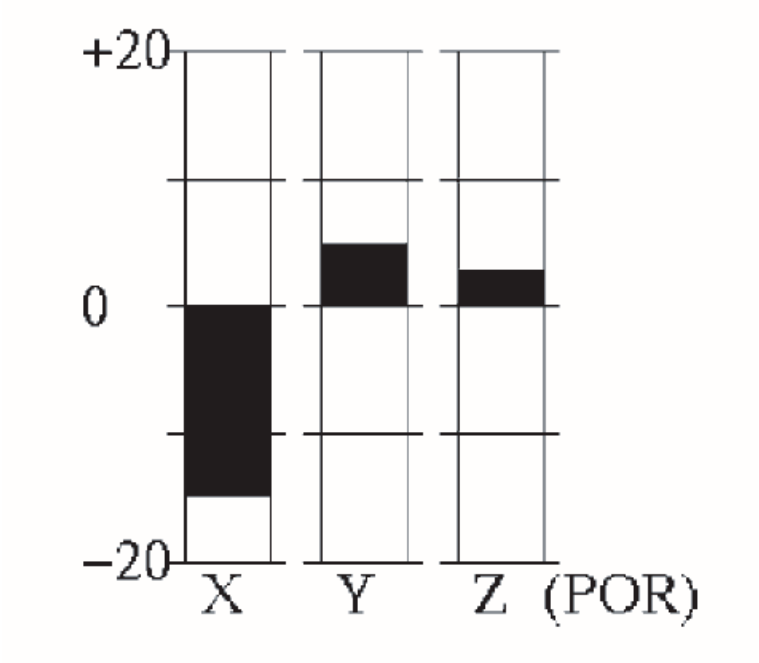

Figure 3.10: Bar graph of force telemetry.

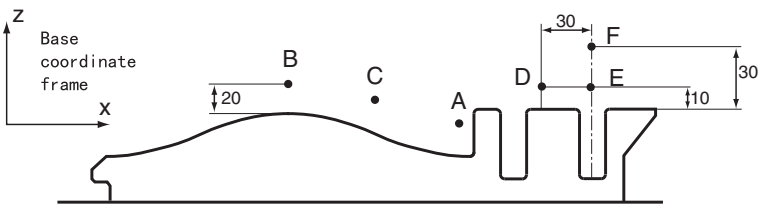

Figure 3.11: Starting points for slope-tracing and peg-in-hole tasks.

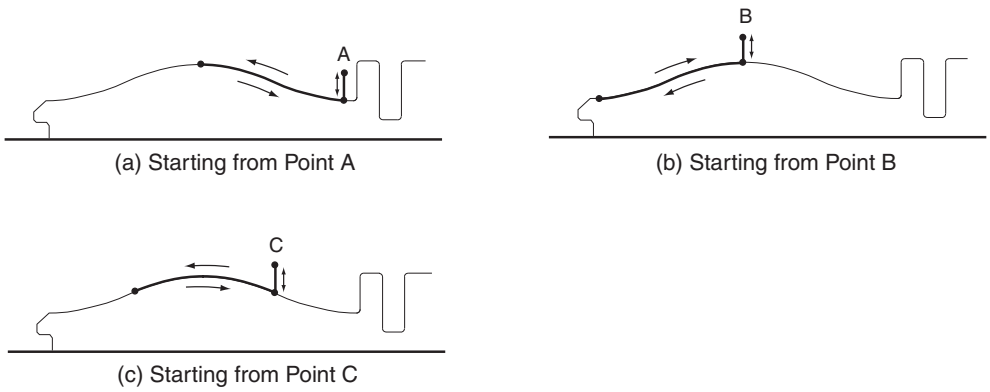

Figure 3.12: Three trajectory patterns in slope-tracing task.

3.4 Experimental results

The experiment was conducted on November 22, 1999. Round-trip time for communication between the control station at the NASDA Tsukuba Space Center and the ETS-VII, flying at an orbit 550 km above the ground, was approximately 6-7 s. Fig. 3.13 shows the measured time delay at each " path. " One can see that time delay differs between each path, but does not fluctuate so much within each path. Figs. 3.8 and 3.9 are snapshots taken during the slope-tracing task experiment.

3.4.1 Pushing Task

Fig. 3.14 shows two typical examples of the force response during the pushing tasks with the bilateral mode and unilateral- plus-telemetry mode, respectively. One can see that the bilateral mode reaches the desired force more quickly and accurately than the unilateral mode. Fig. 3.15 summarizes the results of the pushing task.

3.4.2 Slope-Tracing Task

Table 3.3 shows the results of the estimation of the starting points by the operators. Except for Task 1, the operators, including the NASDA operator, could estimate the starting points correctly. We cannot clearly explain why the operator failed in Task 1. One possibility would be due to some psychological factors such as stress for the first trial or not being accustomed to the experiment. It should be noted, however, that in the bilateral mode, the shape estimation became confident from the beginning with only a little movement of the handle, whereas in the unilateral mode, the estimation was quite uncertain, even after the entire movement. Fig. 3.16 can help to understand the reason for this observation. This figure shows typical arm trajectories (top) and force responses (bottom) in the bilateral mode and unilateral-plus-telemetry mode, respectively. In the bilateral mode, the trajectory of the master handle reproduces the slope shape, while in the unilateral mode, it is difficult to estimate the slope shape from the master handle trajectory. From the force response, one can see that in the unilateral mode, sometimes the

robot arm loses contact with the tracing slope. It means that tracing the slope was difficult in the unilateral mode.

Fig. 3.17 summarizes the experimental results of the tracing task. The stroke in the task with the unilateral mode had to be reduced to 130 mm, 20-mm shorter than the initial plan, to go back to the starting point within the time limit. Like the pushing task, with the bilateral mode, one could adjust the applied forces to the desired value more accurately and complete the task faster than with the unilateral mode. It is interesting to notice that the performance of Task 1 (i.e., the task when the operator failed to estimate the correct starting point) was not bad. Of course, the correct answers of the starting points were disclosed only after all trials were executed.

We should also note that the task performance of the NASDA operator, who used this system for the first time, was comparable to that of the skilled operator.

3.4.3 Peg-in-Hole Task

Fig. 3.18 shows the arm trajectories of the peg-in-hole task. In the figure, the actual position of the peg, which corresponds to the timing when the operator judged the starting point of the insertion, is also drawn. One can see that in the bilateral mode, the operator could identify the transition of contact state accurately only using the force-feedback information. On the other hand, the recognition of a new contact when the peg reached the bottom of the hole was better when using only telemetry data, rather than using force feedback from the master handle. The times when the operator declared the bottom-reaching were 18, 15, and 5 s after the peg had actually reached the bottom in Task 1, Task 2, and Task 3, respectively. Fig. 3.19 summarizes the results of the peg-in-hole task. In contrast to what we expected, the unilateral mode gave smaller lateral forces than the bilateral mode did. Our explanation of this observation is that the operator moved the master arm carefully in the unilateral mode, while he moved the master arm relying on the reaction force from the hole in the bilateral mode. The trajectory of the master handle in Fig. 3.18 supports this explanation. One can see that the position deviation of the master from the centerline of the hole is smaller in the unilateral mode than in the bilateral mode.

3.4.4 Slide-Handle Task

Table 3.4 shows the results of the estimation of the sliding direction in the slide-handle task. In all cases, the operators could estimate the sliding direction with reasonable accuracy. It should be noted, however, that in the bilateral mode, the operator was already confident at a very early stage of the task. Only a little movement of the handle was sufficient for them to identify the sliding direction. In the unilateral mode, they were quite uncertain about their estimation, even after the entire movement. This observation is similar to the previous observation drawn from the slope-tracing task. Fig. 3.20 shows a typical example of the hand trajectory of the slide-handle task with the bilateral mode. In the figure, the inserted rotational transformation was canceled, so ideally the master and slave trajectories should coincide. One can see that the operator moved the handle in the wrong direction at the beginning, but shifted to the correct direction later, feeling the force feedback from the handle.

All operators, including the NASDA operator and the novice operator, could complete the task in the bilateral mode. In the unilateral mode, however, the operator should stop moving the handle only halfway and could not complete the task within the assigned time. The NASDA operator performed only the probing task to estimate the sliding direction.

Fig. 3.21 summarizes the results of the slide-handle task. In contrast to what we expected, the amount of lateral forces could not be reduced in the bilateral mode. This is because the operator exerted large lateral forces when probing the sliding direction at the beginning of the task. This observation is similar to the previous observation in the peg-in-hole task. After the direction was estimated, the lateral forces became small.

3.4.5 Discussion

From the questionnaire survey after each task, the following observations were obtained.

- All three operators paid most of their attention to the force feedback from the master handle, even when the telemetry force data was displayed on the screen.

- Using the kinesthetic force-feedback information, the operators could recognize the shape of the contouring slope as well as the entrance of the peg hole with just a small movement. As for the instant of the contact with the environment (e.g., when the peg reached the bottom of the hole), however, it was difficult to recognize for the operator only from the kinesthetic force feedback, due to the low position gain of the bilateral controller.

- The telemetry force data was noisy and difficult to use for shape recognition. The data should have been passed through a lowpass filter.

- Even a novice operator could complete the task, showing that no specific skill level is required to use this teleoperation system.

It was surprising, even for us, that the kinesthetic force-feedback information was useful and could improve the task performance, even under such a long time delay. Of course, the task should be performed slowly, and the maneuverability is lower than the case without time delay. However, this experiment does prove that it is possible to complete some tasks by direct bilateral control, even under 6-7 s time-delay conditions.

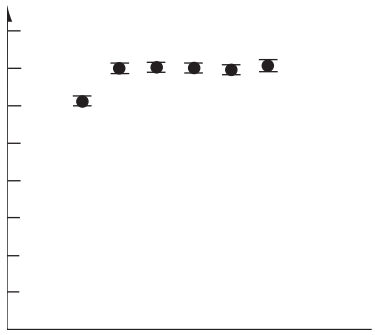

Figure 3.13: Measured time delay for round trip.

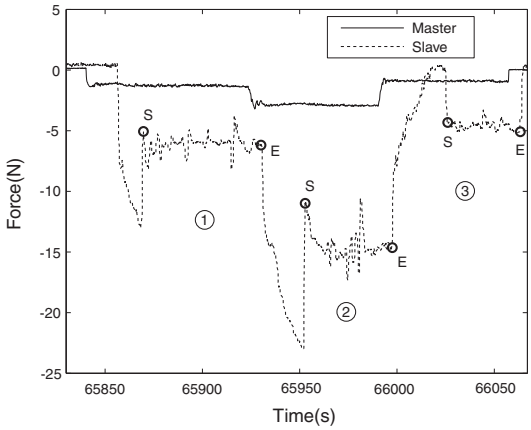

(a) Bilateral

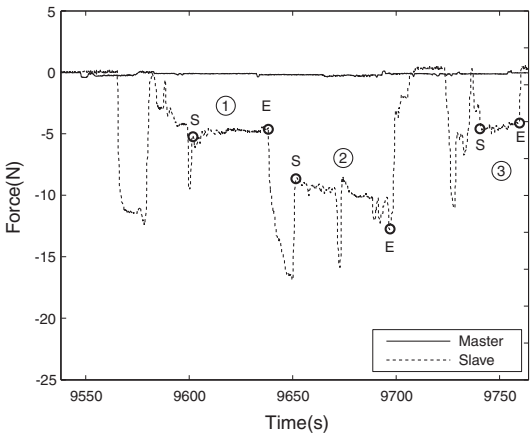

(b) Unilateral + Telemetry

Figure 3.14: Force responses in pushing task.

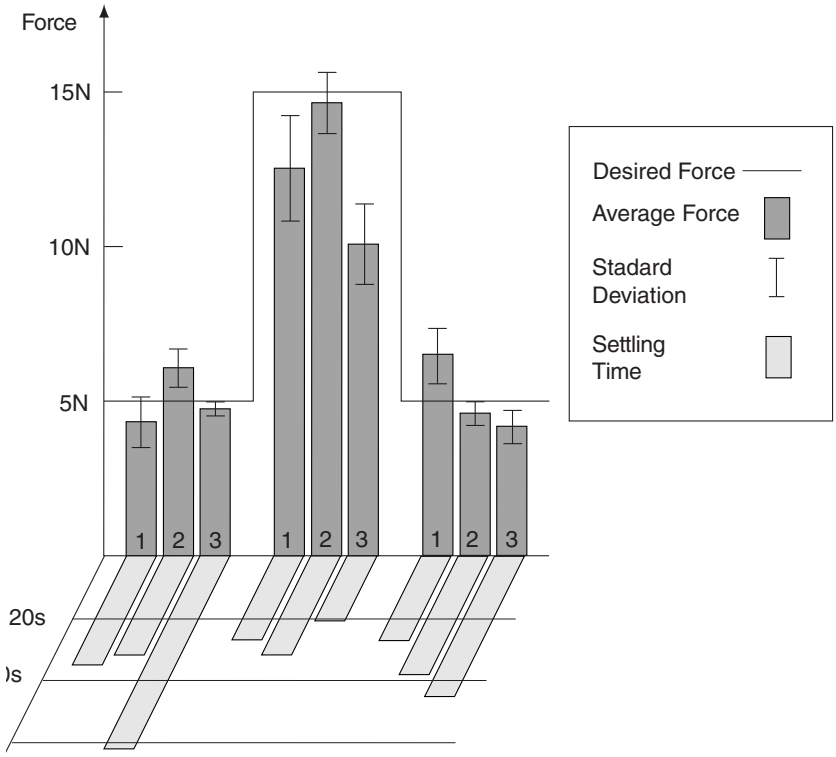

Figure 3.15: Result of pushing task (Task 1: B+T, Task 2: B, Task 3: U+T).

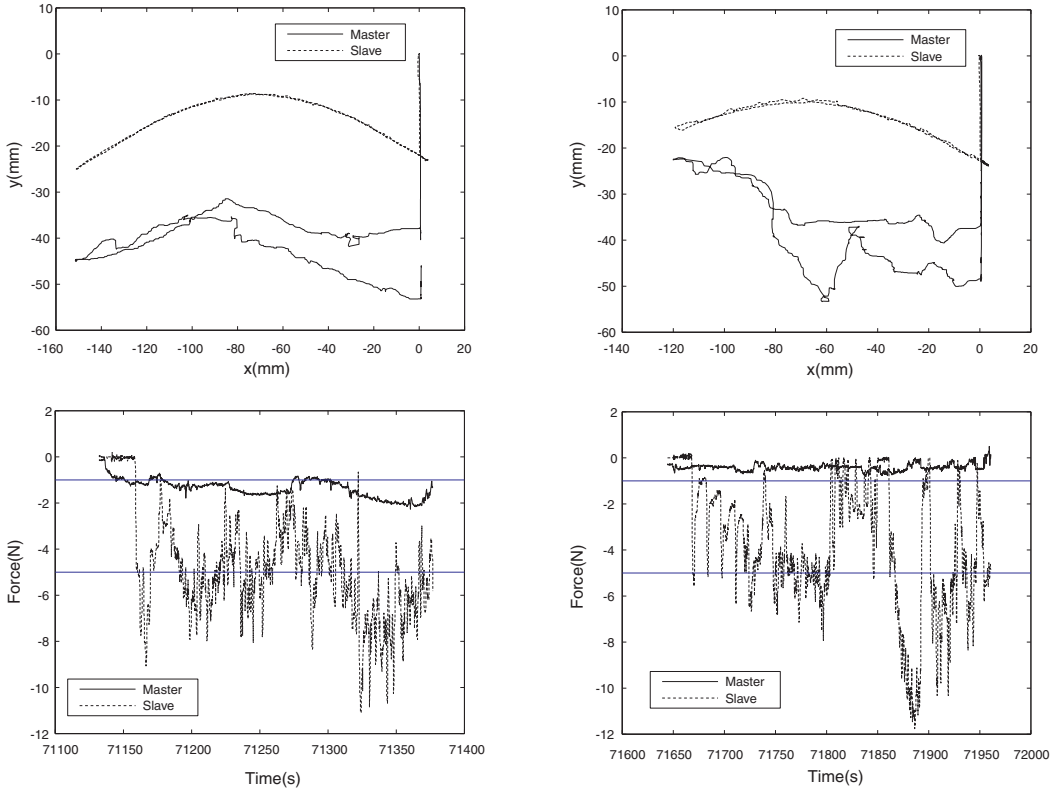

(a) Bilateral (b) Unilateral + Telemetry

Figure 3.16: Typical arm trajectories and force responses in slope-tracing task.

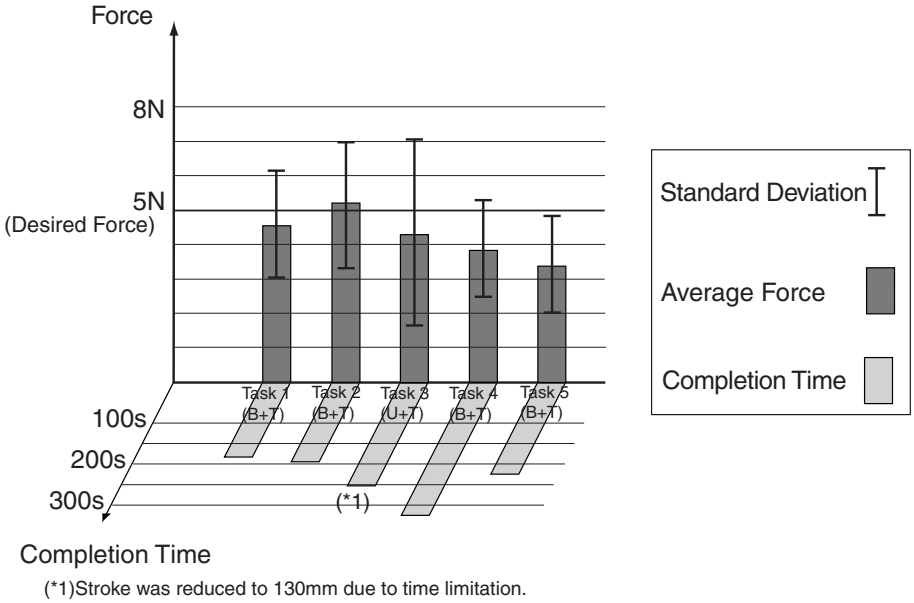

Figure 3.17: Result of slope-tracing task (task numbers correspond to those in Table 3.3).

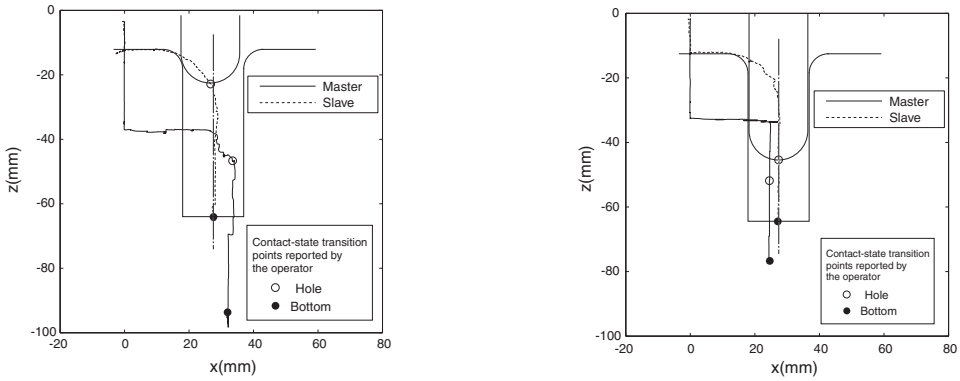

(a) Bilateral (b) Unilateral + Telemetry

Figure 3.18: Arm trajectories during the peg-in-hole task.

Table 3.3: ACTUAL STARTING POINTS AND DECLARED POINTS BY THE OPERATORS

Task Condition	Starting Point	Declared Point	Judgement
Task 1 (Bilateral + Telemetry)	A	C	×
Task 2 (Bilateral + Telemetry)	C	C	○
Task 3 (Unilateral + Telemetry)	C	C	○
Task 4 (NASDA Operator) (Bilateral + Telemetry)	C	C	○
Task 5 (longer operation time) (Bilateral + Telemetry)	B	B	○

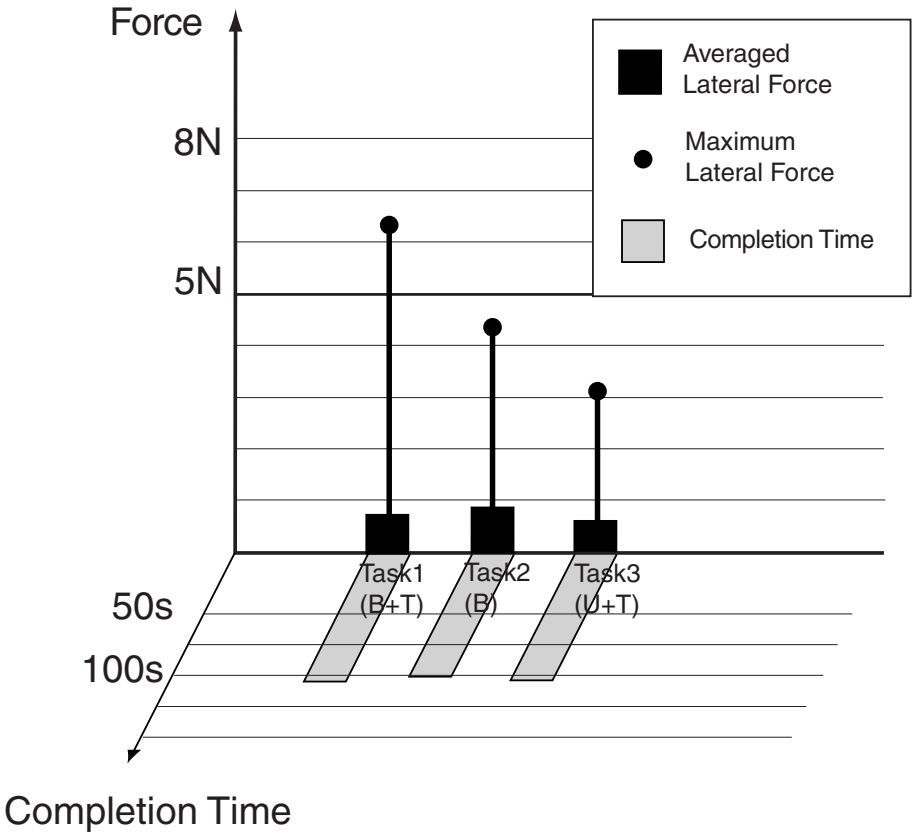

Figure 3.19: Result of peg-in-hole task (Task 1: B+T, Task 2: B, Task 3: U+T).

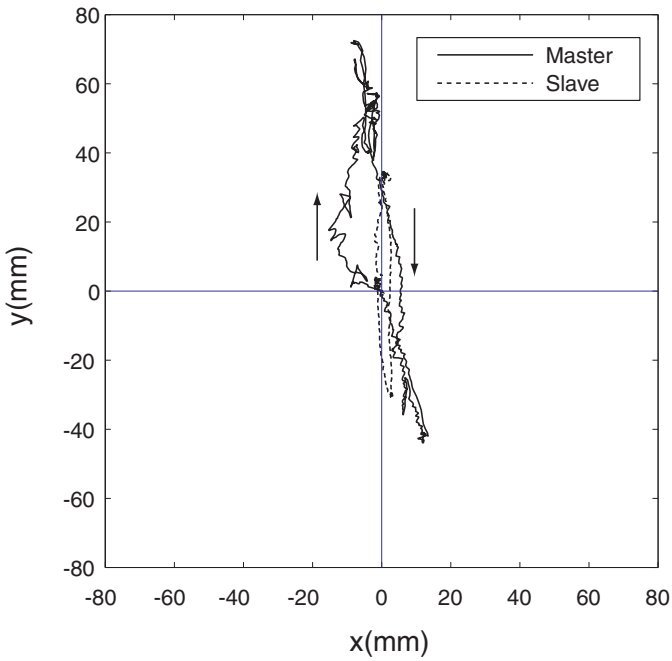

Figure 3.20: Typical arm trajectory in slide handle task (Task 1: Bilateral mode, rotated -75deg).

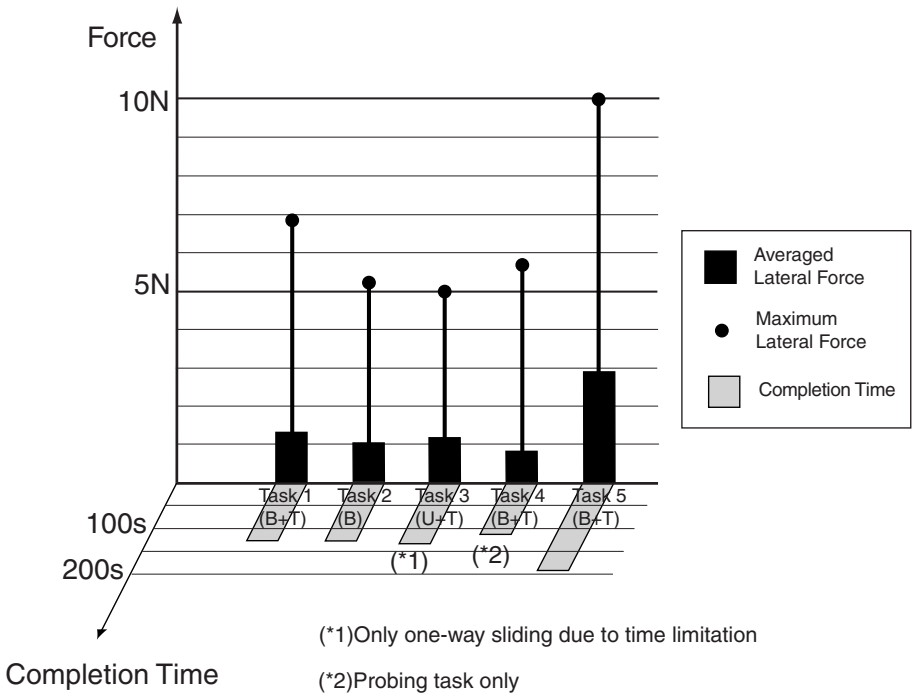

Figure 3.21: Result of slide-handle task (task numbers correspond to those in Table 3.4).

Table 3.4: SLIDING DIRECTIONS AND DECLARED DIRECTIONS

Task	Rotation angle[deg]	Declared angle[deg]
Task 1 (Bilateral + Telemetry)	-75	-65
Task 2 (Bilateral)	0	0
Task 3 (Unilateral + Telemetry)	20	30
Task 4 (NASDA Operator) (Bilateral + Telemetry)	60	45
Task 5 (Novice operator) (Bilateral + Telemetry)	-60	-45

3.5 Conclusion

In this chapter, the results of a ground-space teleoperation experiment using a robot arm mounted on the ETS-VII were shown. Due to the limitation of the onboard robot controller of the ETS-VII, the controller in the previous chapter was modified, and also a modified stability condition was derived. Several tasks, such as a slope-tracing task and a peg-in-hole task, were carried out under 6-7 s time-delay conditions. All the tasks were possible by using the direct bilateral control, even without using any visual information. The experimental results demonstrate that force feedback to the operator is still helpful, even under such a long time delay. To the best of the authors ' knowledge, this experiment is the first ground-space teleoperation by direct bilateral control. Since the number of experiments was limited, and also, only a few subjects joined the experiments, we need further experiments to confirm the obtained results.

In this paper, we have only shown the possibility of performing some tasks under 6-7 s time delays. Please note, however, that we are not claiming that bilateral control under 6-7 s conditions is practically useful. It is needless to say that a shorter time delay gives better maneuverability. Although the ETS-VII is orbiting just 550 km above the earth, the amount of delayed time (6-7 s) is considerably large. Since most of the time delay is due to the data transmission in the computer network on the ground, it is technically possible to make the delay time 1-2 s or less, even if the data is relayed through a satellite on the geostationary orbit.

So far, we have been trying to manage a given time delay on existing data communication infrastructures. These infrastructures were designed without considering the use of direct bilateral teleoperation from the ground. However, if we could expect a breakthrough to improve the maneuverability of teleoperation with a time delay shorter than 6-7 s, we could take a completely new approach, i.e., we would first define the time-delay limitation for given tasks, and then construct a communication link to achieve this time delay. This point is what we really want to emphasize in this paper. To proceed with this approach, we need to investigate the relationship between the task complexity and the allowable time delay in more detail. For this purpose, laboratory experiments, where delay time can be changed easily, would be appropriate. As a benchmark test, the LEGO block assembly, which was proposed by the authors [38], might be useful to evaluate the

task complexity.

Appendix 3A Derivation of stability condition (3.1)

With the modified bilateral controller, the impedance matrix becomes

$$\boldsymbol{Z} = \begin{bmatrix} m_m s + b_m + D_m + \frac{K_m}{s} & K_m e^{-sT_2}/s \\ K_s e^{-sT_1}/s + D'_s e^{-sT_1} & m_s s + D'_s + \frac{K_s}{s} \end{bmatrix}. \tag{3.2}$$

Applying Llewellyn 's stability criterion [18] to (3.2), the following three conditions must be satisfied at all frequencies:

$$B_m \geq 0 \tag{3.3}$$

$$D'_s \geq 0 \tag{3.4}$$

and

$$\begin{aligned} &4(B_m D'_s + \frac{K_m}{\omega}\cos\omega T_2(\frac{K_s}{\omega}\cos\omega T_1 + D'_s \sin\omega T_1)) \\ &\times(B_m D'_s + \frac{K_m}{\omega}\sin\omega T_2(D'_s\cos\omega T_1 - \frac{K_s}{\omega}\sin\omega T_1)) \\ &-(\frac{K_m}{\omega}\sin\omega T_2(\frac{K_s}{\omega}\cos\omega T_1 + D'_s\sin\omega T_1) \\ &+(D'_s\cos\omega T_1 - \frac{K_s}{\omega}\sin\omega T_1)\frac{K_m}{\omega}\cos\omega T_2)^2 \geq 0 \end{aligned} \tag{3.5}$$

where we again set $B_m = b_m + D_m$.

Modifying (3.5), we get

$$\begin{aligned} 4B_m^2 D'_s + 4B_m D'_s(\frac{K_m K_s}{\omega^2}\cos\omega(T_1+T_2) + \frac{K_m D'_s}{\omega}\sin\omega(T_1+T_2)) - \\ (\frac{K_m K_s}{\omega^2}\sin\omega(T_2+T_2) - \frac{K_m D'_s}{\omega}\cos\omega(T_1+T_2))^2 \geq 0. \end{aligned} \tag{3.6}$$

Solving (3.6) for $B_m B_s$, we get

$$B_m D'_s \geq \frac{1}{2}(\sqrt{\frac{K_m^2 K_s^2}{\omega^4} + \frac{K_m^2 D'^2_s}{\omega^2}} - (\frac{K_m K_s}{\omega^2}\cos\omega(T_1+T_2) + \frac{K_m D'_s}{\omega}\sin\omega(T_1+T_2))) \tag{3.7}$$

or

$$B_m D'_s \leq -\frac{1}{2}(\sqrt{\frac{K_m^2 K_s^2}{\omega^4} + \frac{K_m^2 D_s'^2}{\omega^2}} + (\frac{K_m K_s}{\omega^2}\cos\omega(T_1+T_2) + \frac{K_m D'_s}{\omega}\sin\omega(T_1+T_2))). \tag{3.8}$$

From (3.3) and (3.4), we need $B_m D'_s \geq 0$. Therefore, only (3.7) needs to be satisfied. This condition inequality corresponds to (3.1).

We can analytically derive that the left-hand side (LHS) of (3.7) goes to $(K_m K_s/4)((D'_s/K_s)-(T_1+T_2))^2$ as $\omega \to 0$. Unlike the case in Section 2.4, the value of the LHS of (3.7) may exceed this limit. Therefore, we have to check (3.7) until we reach sufficiently small , and check whether $B_m D'_s \geq (K_m K_s/4)((D'_s/K_s) - (T_1+T_2))^2$ is satisfied.

Chapter 4

Performance improvement of the PD-based bilateral teleoperators with time delay by introducing relative D-control

4.1 Introduction

In chapter 2, we derived the stable PD controller conditions with grounded damping. The PD bilateral controller has two designs for adding derivative controller gain, grounded damping, and relative damping. The term "relative damping" means the damping force is proportional to the difference between master velocity and slave velocity. "Grounded damping" means the damping force is proportional to the absolute arm velocity. The characteristics of grounded damping gain and relative damping gain were not studied. Lee, et al [16] studied the PD controller. In their analysis they separately discussed the passivity of a proportional gain - grounded damping gain system and the passivity of a relative damping gain system. They achieved a sufficiently stable teleoperator. However, they did not explain the point how the two types of damping gain effect each other, stability and performance. Nuno, et al [24] [25] [26] [27] studied PD controllers. In their research, they stabilized a teleoperator system with a grounded damper gain and relative damper gain. At the end of their study[25], they noticed that relative

damping gain had a stabilizing effect, but their control law was only stabilized by a grounded damping gain, not with a relative damping gain. The PD controller with only grounded damping and the PD controller with grounded and relative damping have been commonly used in delayed bilateral master-slave applications [10] [32], but a comparison of these two controllers has not been conducted. The effect of the addition of relative damping has not been clarified.

This chapter studies the teleoperator stability of a PD controller with both types of damping. A stability condition is derived. We will show that the introduction of relative damping maintains the stability of a system with attenuated grounded damping and improves performance. The teleoperator performance is studied by a transparency analysis using hybrid matrices and simulations. A controller design procedure that guarantees both stability and performance is proposed. The stability, performance evaluation method, controller design method and controller performance are evaluated with 1-DOF numerical simulations. Finally, peg-in-hole experiments are conducted to evaluate the validity of these methods in a realistic multi-DOF condition.

In this chapter, we assume the delay is constant, the delay value is known, and the delay from master to slave and the delay from slave master are equal. The stability under other delay conditions are discussed in Appendix 4D.

4.2 Stability of PD-based bilateral controller with grounded and relative damping

We derive bilateral PD controller stability with grounded damping and relative damping. The physical interpretation of this controller is shown in Fig. 4.1. The block diagram of the teleoperator is shown in Fig. 4.2.

As shown in Fig. 4.1, we added relative damping gains D_{2m} and D_{2s} in addition to grounded damping gains D_{1m} and D_{1s}.

This type of PD controller is expressed by the following equations:

$$\begin{aligned} \tau_m &= -K_m(x_m(t) - x_s(t - T_2)) \\ &\quad -D_{2m}(\dot{x}_m(t) - \dot{x}_s(t - T_2)) - D_{1m}\dot{x}_m \end{aligned} \tag{4.1}$$

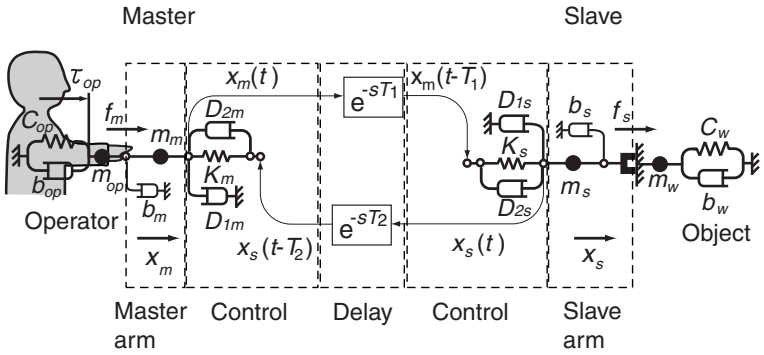

Figure 4.1: Master slave system with PD controller with grounded and relative damping gain.

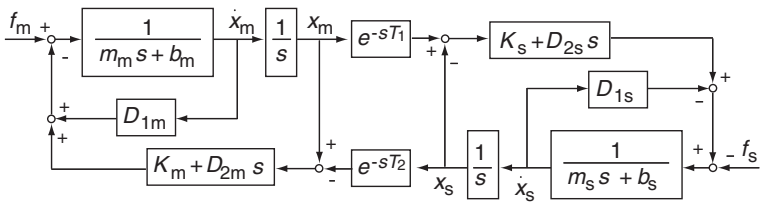

Figure 4.2: Block diagram of master slave system with PD controller with grounded and relative damping gain.

$$\begin{aligned}\tau_s &= K_s(x_m(t-T_1) - x_s(t)) \\ &\quad + D_{2s}(\dot{x}_m(t-T_1) - \dot{x}_s(t)) - D_{1s}\dot{x}_s \ . \end{aligned} \tag{4.2}$$

The elements of the impedance matrix are

$$\begin{aligned} z_{11} &= m_m s + b_m + D_{1m} + D_{2m} + \frac{K_m}{s} \\ z_{12} &= (\frac{K_m}{s} + D_{2m})e^{-sT_2} \\ z_{21} &= (\frac{K_s}{s} + D_{2s})e^{-sT_1} \\ z_{22} &= m_s s + b_s + D_{1s} + D_{2s} + \frac{K_s}{s} \ . \end{aligned} \tag{4.3}$$

Again, for simplicity, we consider the above to be a symmetrical system, i.e. $K_m = K_s = K, D_{1m} = D_{1s} = D_1, D_{2m} = D_{2s} = D_2$, and $T_1 = T_2 = T$.

Applying Llewellyn's criteria to (4.3), the teleoperator is stable for passive terminations if the following conditions are satisfied at all frequencies:

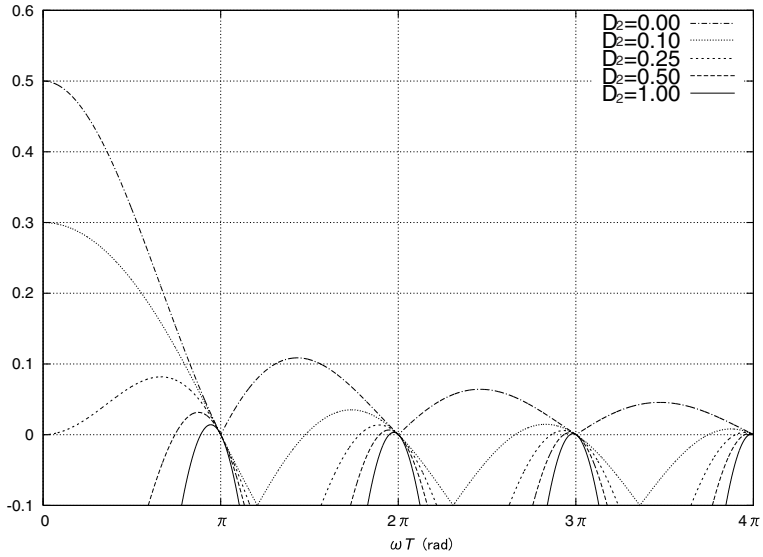

Figure 4.3: Numerical calculation results on the right side of eq. (4.6) (T=0.05 s, K=10.0 N/m).

$$D_1 + b + D_2 \geq 0 \tag{4.4}$$

$$(D_1 + b + D_2)^2 \geq (D_2 \cos \omega T - \frac{K}{\omega} \sin \omega T)^2 \ . \tag{4.5}$$

Eq. (4.5) can be rewritten as follows:

$$D_1 + b \geq |D_2 \cos \omega T - \frac{K}{\omega} \sin \omega T| - D_2 \ . \tag{4.6}$$

By solving (4.6) numerically, we find parameters D_1 and D_2 satisfy (4.4) and (4.6) under given K, T, and b .

In Fig. 4.3, the numerical calculation results on the right side of (4.6) are shown. In this calculation, the parameters used are T = 0.05 s, K = 10.0 N/m, and D_2 =0.00, 0.10, 0.25, 0.50 and 1.00 N·s/m. The case D_2 = 0.00 corresponds to a PD controller with only grounded damping, see Section 2.4. The calculation shows that the grounded damping gain D_1 can be set smaller as a relative damping gain D_2 increases from zero. It should be noted that, in order to satisfy inequality (4.6) with $K > 0$, $D_1 + b$ cannot be zero no matter how large we set D_2.

Table 4.1: $\boldsymbol{H}$ and $\boldsymbol{G}$ matrix elements, physical interpretations and ideal values.

Element of $\boldsymbol{H}$ and $\boldsymbol{G}$ matrix	Physical interpretation					Ideal value
	Condition	Input port	Output port	Interpretation	Conceptual figure	
$h_{12} = \left.\frac{V_m}{V_s}\right\|_{I_m=0}$	Master arm is constrained	Master	Slave	Reverse force gain	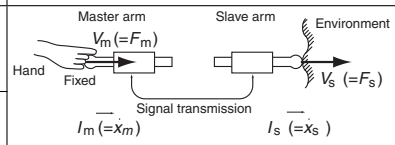	1
$h_{22} = \left.\frac{-I_s}{V_s}\right\|_{I_m=0}$				1/(Output impedance)		0
$h_{11} = \left.\frac{V_m}{I_m}\right\|_{V_s=0}$	Slave arm is free			Input impedance	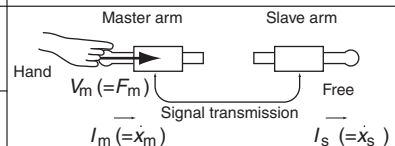	0
$h_{21} = \left.\frac{-I_s}{I_m}\right\|_{V_s=0}$				Velocity gain		-1
$g_{12} = \left.\frac{I_m}{-I_s}\right\|_{V_m=0}$	Master arm is free	Slave	Master	Velocity gain	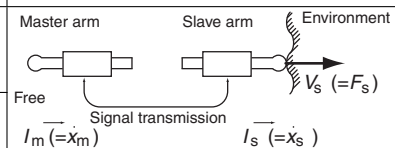	-1
$g_{22} = \left.\frac{V_s}{-I_s}\right\|_{V_m=0}$				Input impedance		0
$g_{11} = \left.\frac{I_m}{V_m}\right\|_{I_s=0}$	Slave arm is constrained			1/(Output impedance)	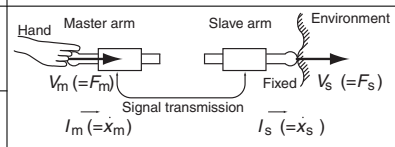	0
$g_{21} = \left.\frac{V_s}{V_m}\right\|_{I_s=0}$				Reverse force gain		1

4.3 Teleoperator transparency as a performance measurement and evaluation using hybrid matrix and inverse hybrid matrix

In this section, we study the performance measurement of bilateral teleoperators with two PD controllers, as shown in the previous section.

For bilataral teleoperation, a completely transparent teleoperation system is ideal, i.e., the operators feel that they are directly interacting with the remote task [15]. If this ideal is achieved, $V_m = V_s$ and $I_s = I_m$ are satisfied.

To measure the performance of the teleoperator quantitatively, Lawrence [15] calculated z_t/z_e and compared it to the ideal value $1+0j$, where z_t is the impedance felt by the operator ($= V_m/I_m$) and z_e is the task impedance ($= V_s/I_s$). Using this

method, we evaluated how operator feeling is similar to the remote task, expressed as z_e.

At first, we used the above quantitative method to measure the performance of a teleoperator by PD controller. When the task dynamics and the master arm dynamics are the same, z_e approaches z_t as the frequency increases. Therefore, the ratio z_t/z_e approaches the ideal value $1 + 0j$, even though the slave arm does not follow the master arm because of the high frequency motion of the master arm and the delay between the master and the slave. In this situation, even if the index z_t/z_e is apparently equal to $1+0j$, the slave arm actually cannot follow the master arm. So the situation is not ideal. The affect of delay between master and slave is not reflected by the index z_t/z_e. The interaction and tracking of the master and slave sides are not reflected by the index z_t/z_e.

According to the discussion above, the performance of our teleoperator with time delay cannot adequately be evaluated by this method. Therefore, we have come to the following conclusions.

Teleoperator performance is basically limited by master arm dynamics and slave arm dynamics. This is remarkable, especially in a high-frequency region. Next, we must discern how transmission characteristics from master to slave and from slave to master effect performance. Therefore, by evaluating each of these four characteristics, performance can be precisely measured. This can be executed by performance evaluation with the hybrid matrix $\boldsymbol{H}$, as proposed by Hannaford [7].

In the next section, we introduce the hybrid matrix expression of the teleoperator [7]. The four elements of the hybrid matrix are input impedance, reverse force gain, velocity gain, and 1/output impedance. These elements are derived from the master arm dynamics, the transmission characteristics from master to slave, the transmission characteristics from slave to master, and the slave arm dynamics.

Performance measurement using $\boldsymbol{H}$ matrix

The teleoperator can be expressed by a hybrid matrix

$$\begin{bmatrix} V_m \\ -I_s \end{bmatrix} = \begin{bmatrix} h_{11} & h_{12} \\ h_{21} & h_{22} \end{bmatrix} \begin{bmatrix} I_m \\ V_s \end{bmatrix} \tag{4.7}$$

where $\boldsymbol{H} = [h_{ij}]$ is the hybrid matrix of the teleoperator. The physical interpretation of h_{ij} is shown in Table 4.1.

If complete teleoperator transparency is achieved, the hybrid matrix becomes as follows:

$$\boldsymbol{H}_{ideal} = \begin{bmatrix} 0 & 1 \\ -1 & 0 \end{bmatrix} . \tag{4.8}$$

Therefore, teleoperator performance can be evaluated by how close the elements of the hybrid matrix are to the ideal values of $\boldsymbol{H}_{ideal}$.

From (4.3), the elements of the hybrid matrix of the teleoperator, see Section 4.2, are calculated as follows:

$$\begin{aligned} h_{11} &= M_m s + D_{2m} + D_{1m} + b_m + \frac{K_m}{s} \\ &\quad - \frac{(D_{2s} + \frac{K_s}{s})(D_{2m} + \frac{K_m}{s})e^{-s(T_1+T_2)}}{M_s s + D_{1s} + b_s + D_{2s} + \frac{K_s}{s}} \end{aligned} \tag{4.9}$$

$$h_{12} = \frac{(D_{2m} + \frac{K_m}{s})e^{-sT_2}}{M_s s + D_{1s} + b_s + D_{2s} + \frac{K_s}{s}} \tag{4.10}$$

$$h_{21} = -\frac{(D_{2s} + \frac{K_s}{s})e^{-sT_1}}{M_s s + D_{1s} + b_s + D_{2s} + \frac{K_s}{s}} \tag{4.11}$$

$$h_{22} = \frac{1}{M_s s + D_{1s} + b_s + D_{2s} + \frac{K_s}{s}} . \tag{4.12}$$

The values of $h_{11}, \cdots, h_{22}$ depend upon the frequency ω. We calculate the limit of $h_{11}, \cdots, h_{22}$ as $\omega \to 0$ and $\omega \to \infty$ limit as shown in Table 4.2. In the far right column, the ideal values are shown. In case of the teleoperation with a time delay, the manipulation speed becomes slower because of the delay, therefore $h_{ij}(\omega \to 0)$ values are important. From the $h_{ij}(\omega \to 0)$ value in Table 4.2, K_m should be set equal to K_s in order to achieve $|h_{12}| \to 1$ at $\omega \to 0$. Larger values of $K_m (= K_s)$ yields smaller $|h_{22}|$ and larger $|h_{11}|$. This relationship is a tradeoff. Longer delays cause a larger damping gain D_1, a larger $|h_{11}|$ and result in performance degradation. This means that the master arm responds in a resistant manner, even when the slave arm is free.

Performance measurement using $\boldsymbol{G}$ matrix

Using $\boldsymbol{H}$ matrix, the performance can be evaluated more precisely than the simple index of z_t/z_e. However, as shown in Table 4.1, we can evaluate the performance with $\boldsymbol{H}$ matrix if the master arm is constrained or the slave arm is free. Here, we study the performance evaluation of other conditions.

Table 4.2: Limit value of hybrid matrix elements and ideal value achieved by perfect transparency.

Matrix	Elements	$\omega \to 0$		$\omega \to \infty$		Ideal value
		Gain	Phase	Gain	Phase	
$\boldsymbol{H}$	h_{11}	$D_{1m} + \dfrac{K_m(D_{1s}+b_s)}{K_s} + K_m(T_1+T_2)$	0	$M_m\omega$	$\dfrac{\pi}{2}$	0
	h_{12}	$\dfrac{K_m}{K_s}$	0	$K_m/M_s\omega^2$ (if $D_{2m}=0$) $D_{2m}/M_s\omega$ (if $D_{2m}\neq 0$)	$-\infty$	1
	h_{21}	1	π	$K_s/M_s\omega^2$ (if $D_{2s}=0$) $D_{2s}/M_s\omega$ (if $D_{2s}\neq 0$)	$-\infty$	-1
	h_{22}	$\dfrac{\omega}{K_s}$	$\dfrac{\pi}{2}$	$\dfrac{1}{M_s\omega}$	$-\dfrac{\pi}{2}$	0
$\boldsymbol{G}$	g_{11}	$\dfrac{\omega}{K_m}$	$\dfrac{\pi}{2}$	$\dfrac{1}{M_m\omega}$	$-\dfrac{\pi}{2}$	0
	g_{12}	1	π	$K_m/M_m\omega^2$ (if $D_{2m}=0$) $D_{2m}/M_m\omega$ (if $D_{2m}\neq 0$)	$-\infty$	-1
	g_{21}	$\dfrac{K_s}{K_m}$	0	$K_s/M_m\omega^2$ (if $D_{2s}=0$) $D_{2s}/M_m\omega$ (if $D_{2s}\neq 0$)	$-\infty$	1
	g_{22}	$D_{1s} + \dfrac{K_s(D_{1m}+b_m)}{K_m} + K_s(T_1+T_2)$	0	$M_s\omega$	$\dfrac{\pi}{2}$	0

In another expression, the teleoperator can be expressed using the $\boldsymbol{G}$ matrix:

$$\begin{bmatrix} I_m \\ V_s \end{bmatrix} = \begin{bmatrix} g_{11} & g_{12} \\ g_{21} & g_{22} \end{bmatrix} \begin{bmatrix} V_m \\ -I_s \end{bmatrix} \tag{4.13}$$

where $\boldsymbol{G} = [g_{ij}]$ is the inverse hybrid matrix of the teleoperator.

Using $\boldsymbol{G}$ matrix, we can evaluate the performance when the master arm is free and the slave arm is constrained, see Table 4.1.

If the complete transparency of the teleoperator is achieved, the inverse hybrid matrix becomes as follows:

$$\boldsymbol{G}_{ideal} = \begin{bmatrix} 0 & -1 \\ 1 & 0 \end{bmatrix} . \tag{4.14}$$

The limits of $g_{11}, \cdots, g_{22}$ as $\omega \to 0$ and $\omega \to \infty$ are shown in Table 4.2.

The relationship between $\boldsymbol{G}$ matrix and $\boldsymbol{H}$ matrix is

$$\boldsymbol{G} = \boldsymbol{H}^{-1} = \begin{bmatrix} \dfrac{h_{22}}{\Delta H} & -\dfrac{h_{12}}{\Delta H} \\ \\ -\dfrac{h_{21}}{\Delta H} & \dfrac{h_{11}}{\Delta H} \end{bmatrix} \tag{4.15}$$

where

$$\Delta H = h_{11}h_{22} - h_{12}h_{21} \ . \tag{4.16}$$

Using the elements of the impedance matrix, ΔH is rewritten as

$$\Delta H = \frac{z_{11}}{z_{22}}. \tag{4.17}$$

When $z_{11} = z_{22}$, we obtain the following equation

$$\begin{bmatrix} g_{11} & g_{12} \\ g_{21} & g_{22} \end{bmatrix} = \begin{bmatrix} h_{22} & -h_{12} \\ -h_{21} & h_{11} \end{bmatrix}. \tag{4.18}$$

Therefore, if the arm dynamics and the controller designs are the same as the master and the slave, and $z_{11} = z_{22}$ is true, the performance of the teleoperator under the four conditions shown in Table 4.1 can be evaluated by computing either the $\boldsymbol{H}$ or $\boldsymbol{G}$ matrix. In this situation, if $\boldsymbol{H}$ is equal to the ideal values of $\boldsymbol{H}$, the ideal response is realized. However, it is impossible to realize the ideal value with all 4 elements of $\boldsymbol{H}$. For example, if we select high position gain to improve the performance of the slave constraint condition, the performance of the slave free condition degrades. Therefore, the designer must choose important factors and design gains in consideration of the task characteristics.

On the other hand, if the parameters or gain settings between master and slave are different, the evaluation of $\boldsymbol{G}$ includes information different from the evaluation of $\boldsymbol{H}$. Therefore, both $\boldsymbol{H}$ and $\boldsymbol{G}$ have to be considered to evaluate the performance. In the case of a scaled teleoperator with force or position scaling, the ideal values of $\boldsymbol{H}$ and $\boldsymbol{G}$ are not the values shown in Table 4.2. They are the values determined by its scaling factor. The performance measurement of a scaled teleoperator with a hybrid matrix is discussed in Appendix 4A.

Table 4.3: Gain settings for both controllers: Type A and Type B.

Type	K [N/m]	D_1 [N·s/m]	D_2 [N·s/m]	Description
A	10.0	0.5	0.0	PD controller with grounded damping
B	10.0	0.02	1.0	PD controller with grounded damping and relative damping

4.4 1-DOF simulation and controller design

4.4.1 Controlled system and controller design

In this section we show the results of 1-DOF numerical simulations. We assume a linear master slave system as shown in Figs. 2.1 and 4.1. To confirm the effect of relative damping, we compare the two controller types. In the simulations, we assume the time delay $T_1 = T_2 = T = 0.05$ s, the arm inertia $M_m = M_s = M = 1$ kg, and the mechanism viscous coefficient $b_m = b_s = b = 0$ N·s/m.

We designed two controllers. Type A controller is a PD controller with grounded damping, as shown in Section 2.4. Type B controller is a PD controller with grounded and relative damping, as shown in Section 4.2. With both types, we set the controller proportional gain, $K_m = K_s = K = 10$ N/m. With type A, we set D_2 to satisfy condition (2.34). With type B controller, we set D_2 gain, $D_{2m} = D_{2s} = D_2 = 1.0$ N·s/m. Using numerical calculation, we set $D_{1m} = D_{1s} = D_1 = 0.02$ N·s/m to satisfy the stability condition (4.6). Fig. 4.4 shows the result of numerical calculation with D_1 gain setting.

Table 4.3 shows the controller gains. Fig. 4.5 shows the bode plot of each element of the hybrid matrix for both types of controller. In the low-frequency area, $|h_{11}|$ is closer to the ideal value for a type B controller. The magnitude of h_{11} at $\omega \to 0$ is 2.0 with a type A controller, while it is 1.04 with a type B controller. The ideal value is $|h_{11}| = 0.0$. This means that a type B controller is less conservative than a type A controller in the low frequency region, including direct current. By adding the relative damping gain, the grounded damping gain can be attenuated and overall conservativeness is reduced. Around $\omega = 3$ rad/s,

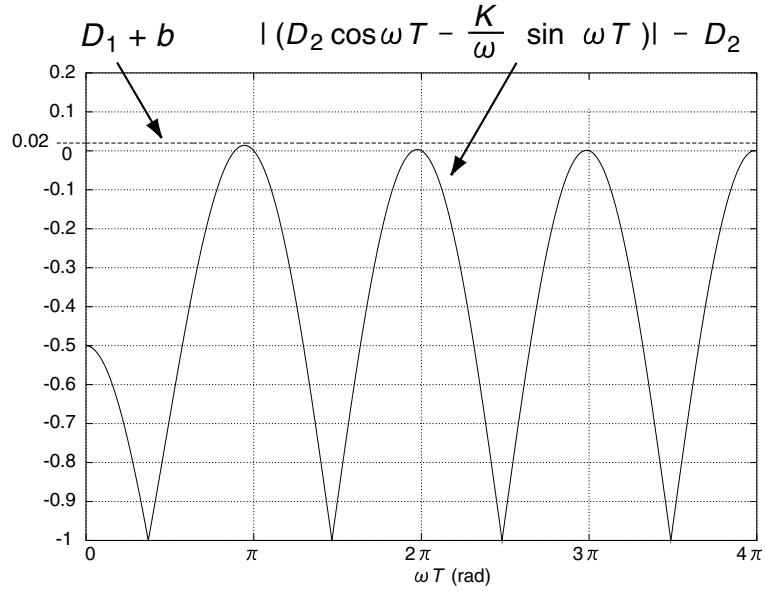

Figure 4.4: Plot of the stability condition and D_1 gain setting. The solid line is the right side of (4.6) and the dashed line is the left side of (4.6).

$|h_{22}|$ is closer to the ideal value in the a type B controller than the a type A. In the high frequency region, h_{11} and h_{22} approach $M_m\omega$ and $1/M_s\omega$, respectively, $M_m\omega$ and $1/M_s\omega$ represent the dynamics of master and slave.

4.4.2 Simulation cases

Using the control law designed in the previous section, we conducted simulations. The tasks were a mass pushing task and a wall pushing task. Table 4.4 shows the simulation cases and parameter settings. To compare the controller performance using two environmental settings, we calculated four simulation cases. In all cases, the initial state is $x_m = 0$, $x_s = 0$, $\dot{x}_m = 0$, and $\dot{x}_s = 0$.

In all cases, we assume that the operator applies a force of 1 N for 10 s to the master arm from $t = 10$ s to $t = 20$ s, see Figs. 4.6 and 4.7.

We set the slave environment as in Table 4.4. In cases 1 and 2, the slave environment is a simple mass hold. In case 3 and 4, the slave arm is constrained by an elastic wall. The natural position of the elastic wall is $x_s = 0$.

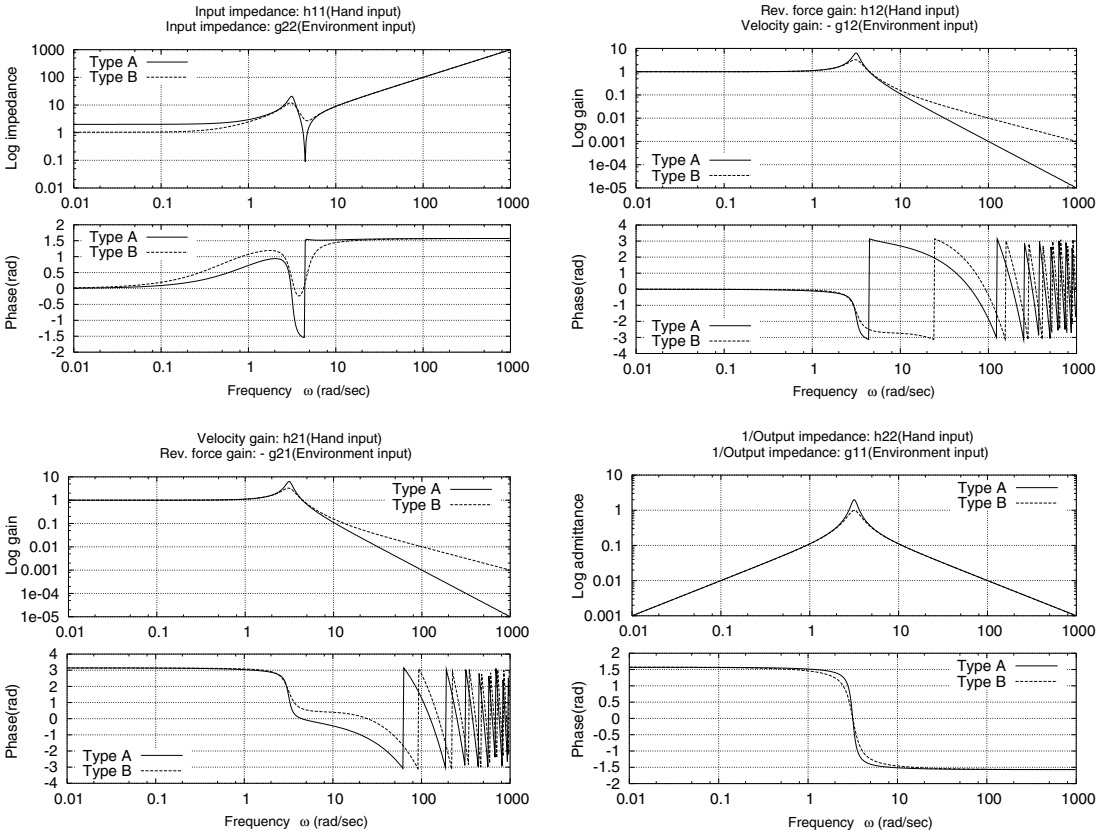

Figure 4.5: Frequency-dependent H and G matrix of a Type A controller (only grounded damping) and a Type B controller (with grounded and relative damping).

4.4.3 Simulation result and discussion

Figs. 4.6 and 4.7 show the simulation results of the mass pushing task and the wall pushing task. In Fig. 4.7, the ideal response is the master arm position and the slave position are the same, and the force at the master arm and the force at slave arm are the same. In the mass pushing task, the mass moves slower than the ideal response because of the viscous force of the damping gain and the inertia of the arms. However, the mass moves more quickly with the type B controller than the type A. This result agrees with the low-frequency h_{11} value in Fig. 4.5. The fluctuation of force at the slave arm is less with a type B controller, see Fig.4.6(b). In the wall pushing task, the fluctuation of the arm position is observed. Fluctuation of arm positions occurs around the frequency of 0.5 Hz and is smaller with a type B

Table 4.4: Simulation parameter settings.

Case No.	Controller type	Slave side environment	C_w [N/m]	M_w [kg]	b_w [N·s/m]
1	A	Mass hold	0.0	1.0	0.0
2	B	Mass hold	0.0	1.0	0.0
3	A	Constrained by elastic wall	100.0	0.0	0.0
4	B	Constrained by elastic wall	100.0	0.0	0.0

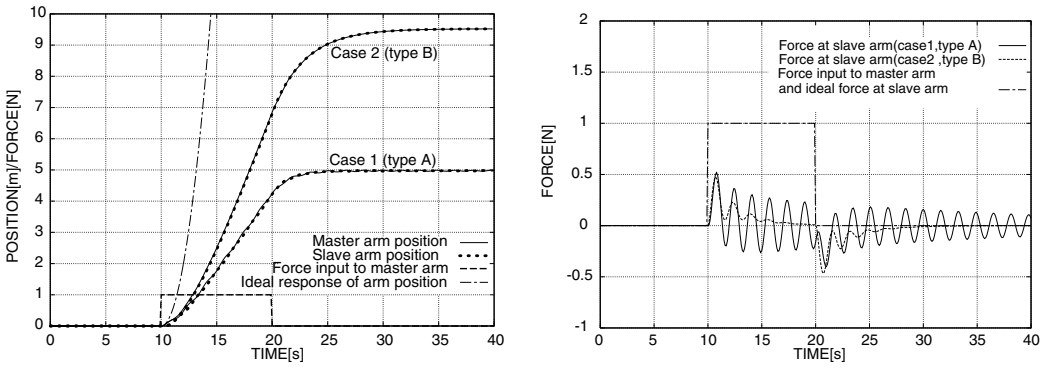

(a) (b)

Figure 4.6: Simulation results. The slave environment is mass hold. Operator force of 1N is inputted to the master arm for 10 s. Case 1 is PD with grounded damping and Case 2 is PD with grounded and relative damping.

controller. This result agrees with the g_{11} value in Fig. 4.5. The simulation results and performance evaluation results of $\boldsymbol{H}$ are consistent. Appendix 4B shows the simulation results on the slave side of the rigid wall environment.

4.5 1-DOF experiment

To confirm the effectiveness of the proposed controller and the validity of the simulation results, we conducted an experiment with a pair of manipulators.

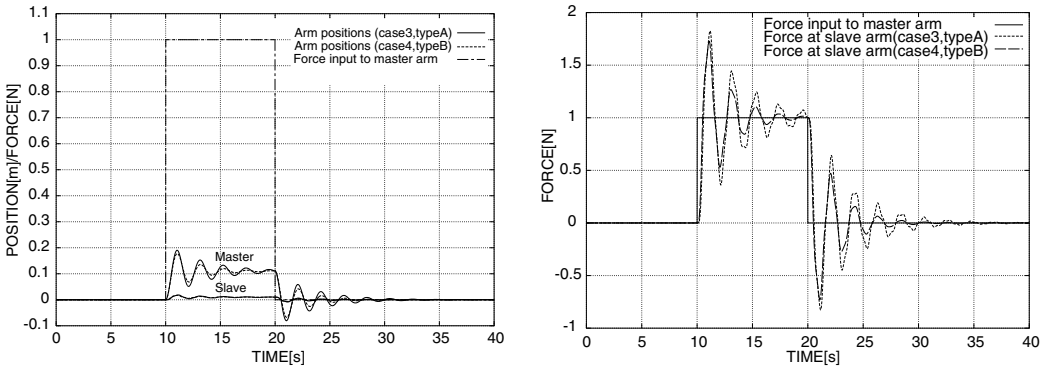

(a) (b)

Figure 4.7: Simulation results. The slave environment is an elastic wall. Operator force of 1N is inputted to the master arm for 10 s. Case 3 is PD with grounded damping and Case 4 is PD with grounded and relative damping.

4.5.1 Experimental System and Experimental Cases

Fig. 4.8 shows the experimental master-slave system. The master and slave arms are 3-DOF planar-type manipulators with electric motors, harmonic-drive reduction gears, and an encoder at each joint. In this experiment, the elbow and wrist joints (J2m,J2s,J3m,J3s) are fixed, and only 1 DOF is used. The arm length is 0.7 m. A torque sensor is attached to each joint and each joint is controlled by a Torque Servo Actuator (TSA) [19]. The measured torque error is fed back to the servo controller and a fine torque control of the output axis is achieved. Using TSA control, undesirable friction torque generated by the harmonic-drive gear is compensated and attenuated. TSA gain at the shoulder joint is 12. A PC with an Athlon microprocessor (1.9 GHz) is used to control both arms. The sampling period is 1.0 ms, and the control law calculation frequency is 1 kHz. Each time delay from master to slave and from slave to master is 50 ms. The time delay is calculated with software. The signals are buffered in the memory for the time delay. Inertial parameters of the master and the slave arms are $M_m = M_s = 1.27$ kg·m^2. Table 4.5 shows the experimental cases and gain settings. The cases and gain settings are similar to those shown in Section 4.4.2. In the case of an elastic wall environment, the slave arm tip is connected to an elastic cord, and the elastic constant is 48 N·m/rad at the shoulder joint. In order to apply a constant

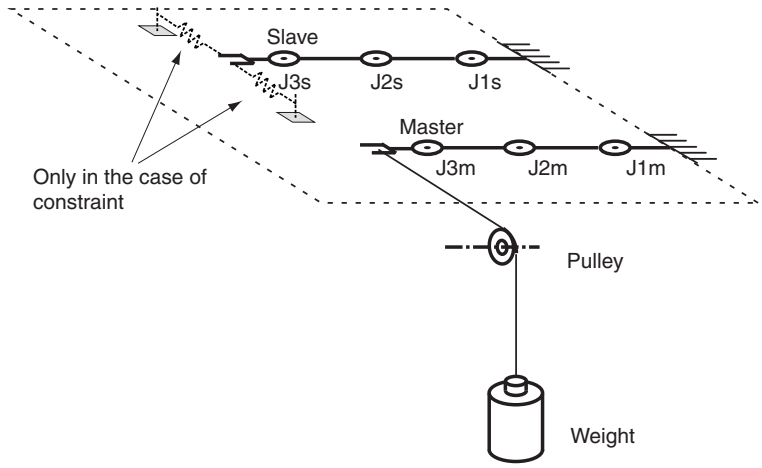

Figure 4.8: 1-DOF experimental setup.

force to the master, we used a pulley and a weight, see Fig. 4.8.

4.5.2 Experimental Results

Fig. 4.9 shows the experimental results. We conducted the same experiment three times. Fig. 4.10 shows the typical time response of a 1-DOF experiment. Fig. 4.11 shows the motor command. In Fig. 4.10, we plotted simulation results as well as experimental results. In the simulation, the joint friction of the real hardware 0.05 N·m is included. In the case of free motion, because of the viscous force of the damping gain, the arm movement is sticky. However, as shown in Figs. 4.9 and 4.10, the arm moves more quickly with a type B controller than a type A when the same force is applied to the master arm. In the case of an elastic wall environment, overshoot of the arm position at the moment of wall contact is observed. The overshoot is smaller with controller type B than type A. The simulation results and experimental results are consistent. In Fig.4.11, the motor command fluctuation in free motion is less with a type B controller.

Table 4.5: 1-DOF experiment cases and gain settings.

Case No.	K [N /rad]	D_1 [N·s /rad]	D_2 [N·s /rad]	Slave side environment	Force applied to the master arm		Result	Typical time response
					Tip force [gf]	Equivalent joint torque [N·m]		
1	10	0.5	0.0	Free	100	0.68	Fig. 4.9(a)	Fig. 4.10 (a)
2	10	0.02	1.0	Free	100	0.68		Fig. 4.10 (b)
3	10	0.5	0.0	Elastic wall	200	1.36	Fig. 4.9(b)	Fig. 4.10 (c)
4	10	0.02	1.0	Elastic wall	200	1.36		Fig. 4.10 (d)

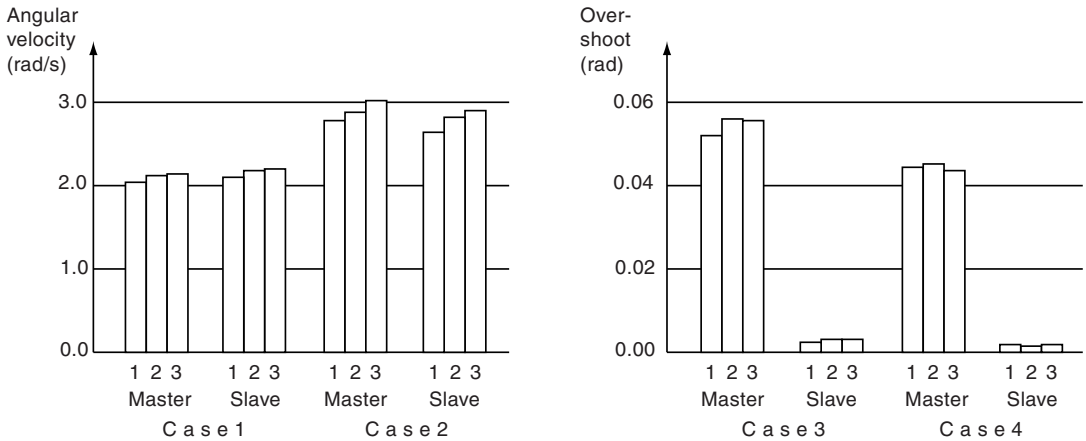

(a) Arm angular velocity in free motion (b) Overshoot upon contacting the wall

Figure 4.9: 1-DOF experimental result.

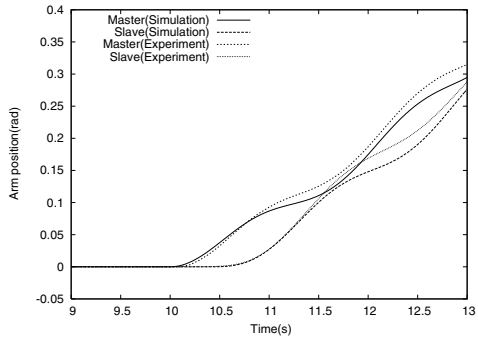

(a) Free motion with type A controller (Case 1)

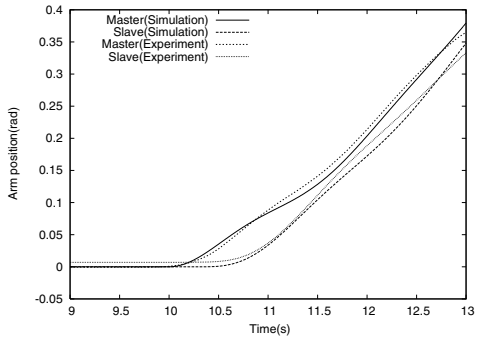

(b) Free motion with type B controller (Case 2)

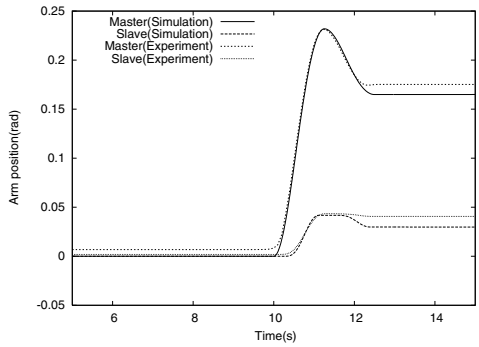

(c) Wall contact with type A controller (Case 3)

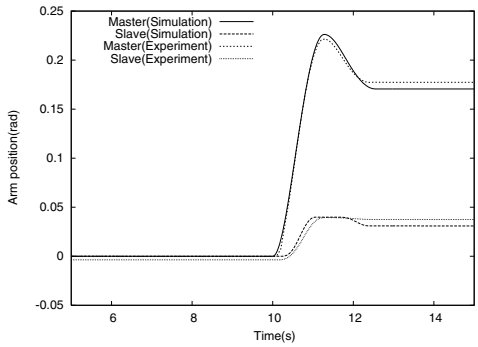

(d) Wall contact with type B controller (Case 4)

Figure 4.10: Typical time response in 1-DOF experiments: Type A an Type B controllers.

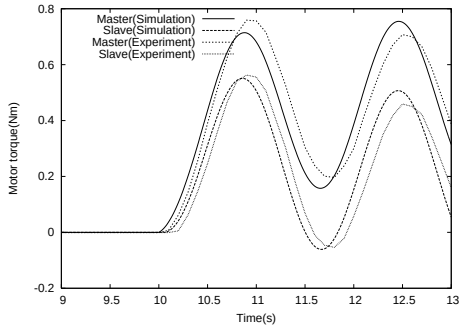

(a) Free motion with type A controller (Case 1)

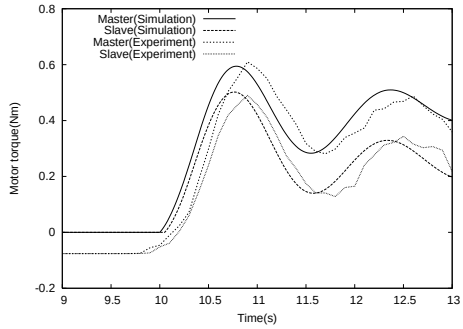

(b) Free motion with type B controller (Case 2)

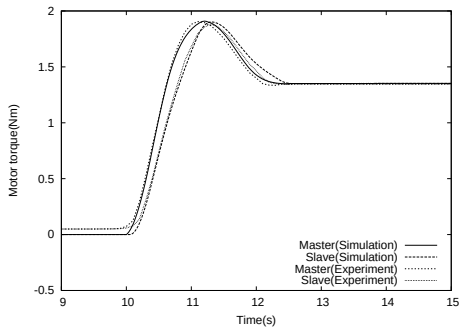

(c) Wall contact with type A controller (Case 3)

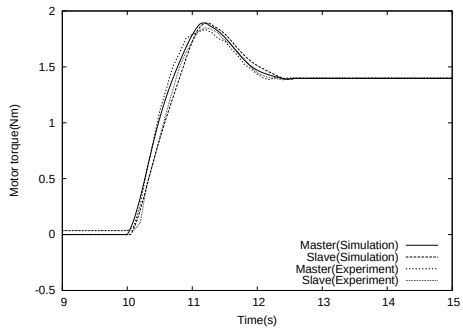

(d) Wall contact with type B controller (Case 4)

Figure 4.11: Motor command of 1-DOF experiment.

Table 4.6: 2-DOF peg-in-hole experiment test cases and results.

Case No.	Controller type	K [N/rad]	D_1 [N·s/rad]	D_2 [N·s/rad]	Visual information	Task completion time	Position deviation	Typical arm tip trajectory	Motor command deviation
1	A	50.0	2.5	0.0	Yes	Fig. 4.14(a)	Fig. 4.14(b)	Fig. 4.15	Fig. 4.19
2	B	50.0	0.1	5.0	Yes			Fig. 4.16	
3	A	50.0	2.5	0.0	No			Fig. 4.17	
4	B	50.0	0.1	5.0	No			Fig. 4.18	

4.6 2-DOF peg-in-hole experiment

4.6.1 Experimental system and experimental cases

To confirm the effectiveness of the proposed control law in a realistic multi-DOF plant, we conducted a 2-DOF peg-in-hole task. The passivity of a 2-DOF system is discussed in Appendix 4C. Fig. 4.12 shows the experiment setup, the same hardware as in 4.5.1. As shown in Fig. 4.12, the master and the slave arms move symmetrically, therefore the direction of x_m and x_s are opposite. Table 4.6 shows the experiments and their gain settings. The controller gain of joint 1 and 2 are the same. Each time delay from master to slave and from slave to master is 50 ms. The control law calculation frequency is 1 kHz. As a peg, an aluminum disk of 74 mm diameter is attached at the slave arm tip. The hole, an opening of 74 mm gap is in a wall, see Fig. 4.12. The desired task is to push the wall in +y direction, trace the wall toward −x direction, and insert the peg into the hole. The arm lengths are shown in Fig. 4.12. The parameters of the master and the slave are the same. The hole is located at the position of $x = -0.3$ m. In cases 1 and 2, the operator can see the slave side. In cases 3 and 4, a screen is located between master and slave. Therefore, the operator cannot see the slave, and the operator operates with only force information. The operator's view is shown in Fig. 4.13.

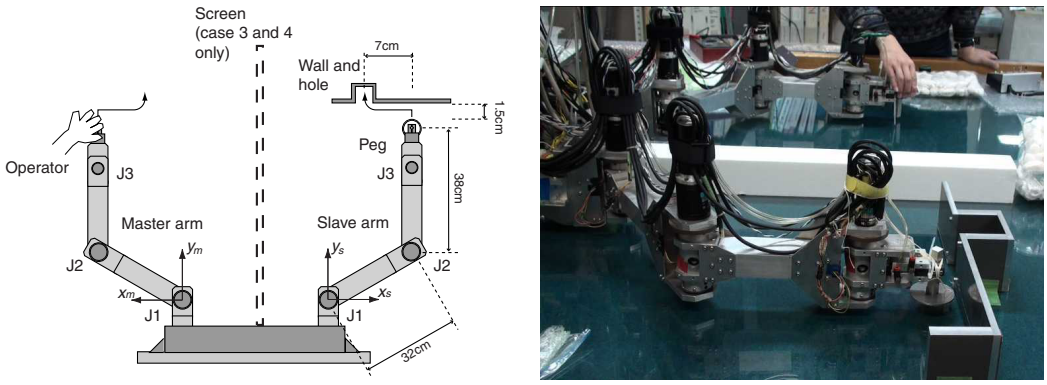

(a) Task and initial position (b) Experiment

Figure 4.12: Setup of 2-DOF peg-in-hole experiment.

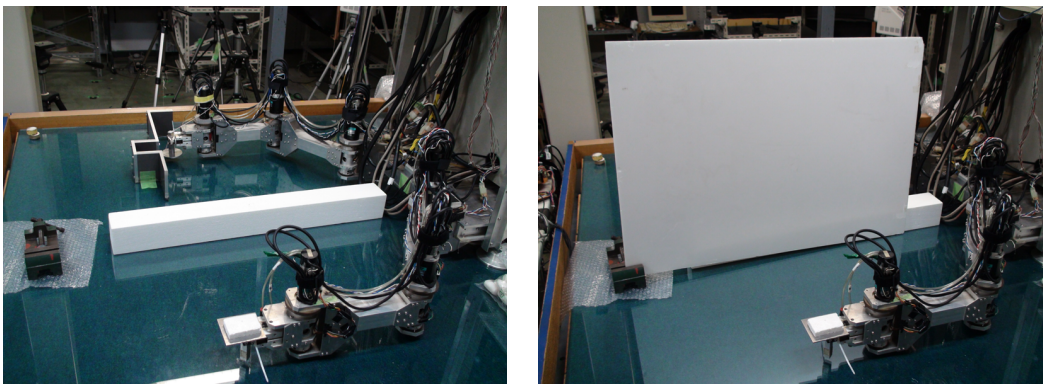

(a) Cases 1 and 2 (b) Cases 3 and 4

Figure 4.13: Operator's view of slave side.

4.6.2 Experimental result and discussion

Fig. 4.14 shows experimental results. Figs. 4.15 to 4.18 show typical arm tip trajectory and motor command time plots. Along the lines illustrating the arm tip trajectories, the circles represent the arm tip positions at the time of adjacent numbers. The time is from the beginning of the experiment. As seen in Figs. 4.15 to 4.18, tasks can be completed even without transmitting visual information to the operator. From this, we can tell that the force information to the operator is effective. In Fig. 4.14, task completion time is shown. When the peg insertion on the slave side reaches the bottom of the hole, we consider the task completed. In cases with visual information, the task completion times are shorter than in cases without visual information. As shown in Fig. 4.14, a type B controller completes the task more quickly than a type A.

As for position tracking, ideally, the trajectory of the master arm and the slave arm are the same. In Fig. 4.14, the average position tracking error of master tip and slave tip during the operation is shown. The position tracking performance is better with a type B controller than a type A. The position difference in x direction during the peg insertion is smaller with a type B controller. Therefore, the operator can acknowledge the position of the hole more accurately with a type B controller.

A force sensor is not attached at the arm tip. Therefore we cannot measure the arm tip force and evaluate the force tracking. However, the transparency of the control law itself can be evaluated by the motor command error between master and slave. The result is shown in Fig.4.19. The error during the task is smaller with a type B controller than a type A controller. The transparency of control law is better with type B.

4.7 Conclusion

The stabilizing effect and performance improvement by introducing a relative damper to a PD-based teleoperator with time delay has been studied. First, we derived the stability condition of a PD-based controller with only grounded damping, and with both grounded and relative damping. By introducing the relative damping, the system maintained stability with attenuated grounded damping. Second, performance evaluation was conducted using a hybrid matrix. As a result, we

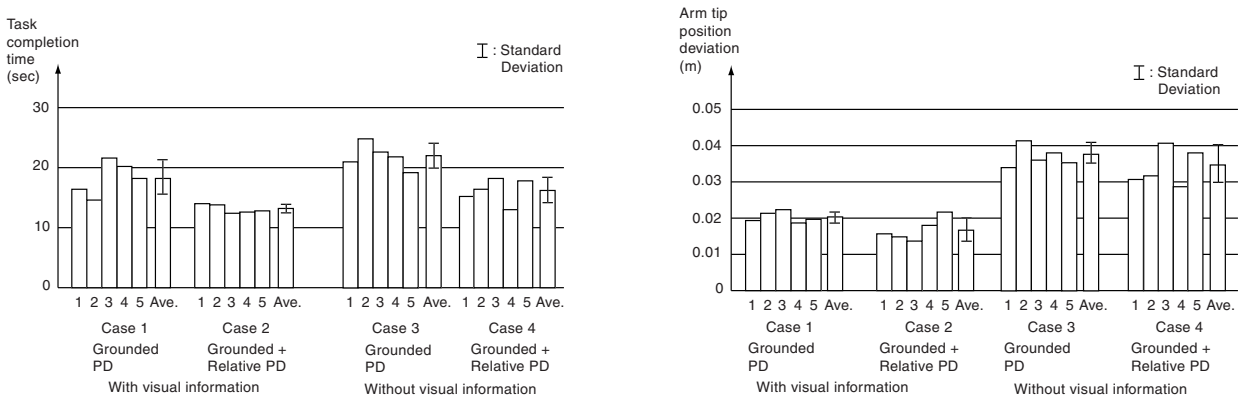

(a) Task completion time (b) Position deviation between master and slave arm

Figure 4.14: 2-DOF experimental results. Task completion time and arm tip position deviation: 5 time trials and their average value is shown.

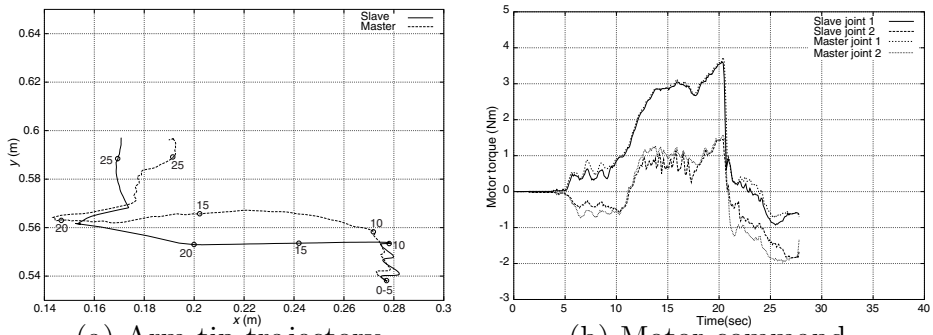

(a) Arm tip trajectory (b) Motor command

Figure 4.15: 2-DOF peg-in-hole experiment results with visual information (Type A controller).

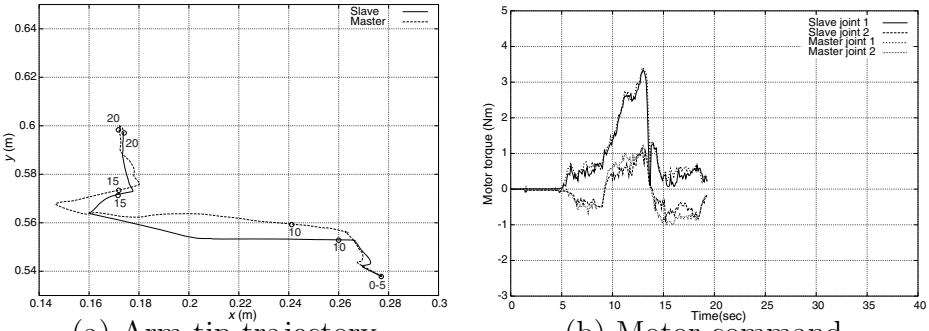

(a) Arm tip trajectory (b) Motor command

Figure 4.16: 2-DOF peg-in-hole experiment results with visual information (Type B controller).

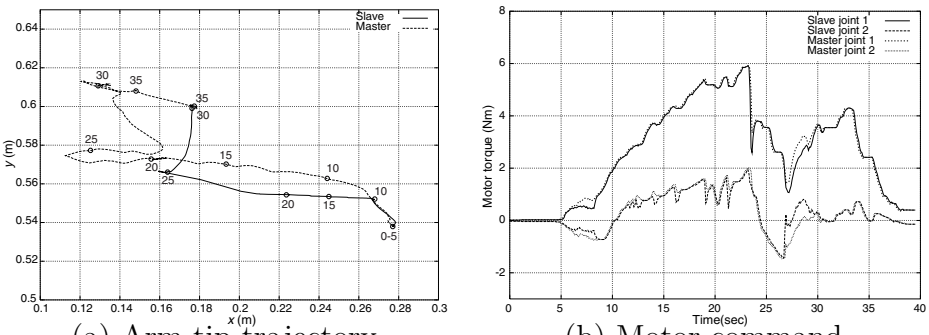

(a) Arm tip trajectory (b) Motor command

Figure 4.17: 2-DOF peg-in-hole experiment results without visual information (Type A controller).

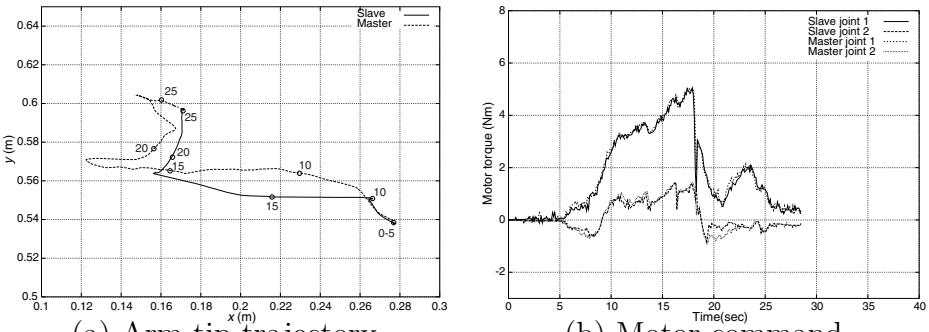

(a) Arm tip trajectory (b) Motor command

Figure 4.18: 2-DOF peg-in-hole experiment results without visual information (Type B controller).

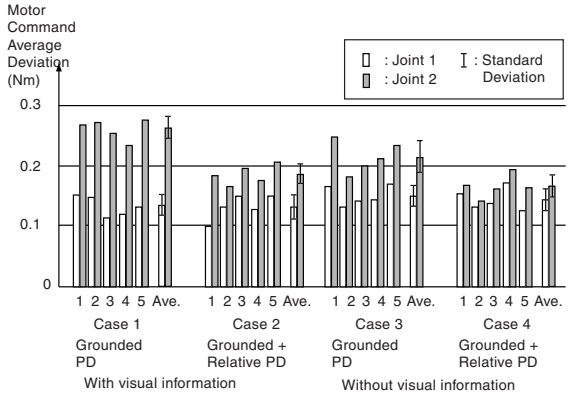

Figure 4.19: 2-DOF experimental results. Motor command average deviation between master and slave (5 time trials and average values) are illustrated. The deviation is smaller with Type B controller than Type A controller.

showed that introducing relative damping into a PD-based controller improved the performance of the teleoperator. Third, to evaluate teleoperator performance, we conducted 1-DOF simulations, 1-DOF experiments and 2-DOF peg-in-hole experiments. The teleoperator performance was evaluated using these simulations and experiments. These results showed performance improvement with a PD controller with relative damping.

With regard to the consistency of the evaluation with $\boldsymbol{H}$ and simulation/experimental results, the validity of performance evaluation with the $\boldsymbol{H}$ matrix was demonstrated. By iterating the stable gain setting and performance evaluation using the $\boldsymbol{H}$ matrix as shown in this paper, a controller design that guarantees both stability and performance has been achieved.

The design methodology of optimum gain balance of relative and grounded damping, performance comparison with other control law, such as a passivity based approach, and stability analysis with time-variant delay will be investigated in future research.

Appendix 4A. Performance measurement of asymmetrical teleoperator using a hybrid matrix

When designing an asymmetrical teleoperator, (4.9) $\sim$ (5.12) can be applied, but (4.18) does not hold true. This means, not only $\boldsymbol{H}$ but also $\boldsymbol{G}$ has to be considered to evaluate the performance under the 4 constraint conditions shown in Table 4.1. In order to evaluate $\boldsymbol{H}$ and $\boldsymbol{G}$, we have to consider no fewer than 8 elements, a complicated procedure. However, performance evaluation can be simplified and can be judged with only the $\boldsymbol{H}$ matrix under the following conditions.

Assume the asymmetrical teleoperator illustrated in Fig. 4.20 whose position scaling is n and force scaling is k.

From the meaning of the scaling factor, $\boldsymbol{H}$ and $\boldsymbol{G}$ for the ideal responses are:

$$\boldsymbol{H}_{ideal} = \begin{bmatrix} 0 & k \\ -1/n & 0 \end{bmatrix}, \quad \boldsymbol{G}_{ideal} = \begin{bmatrix} 0 & -n \\ 1/k & 0 \end{bmatrix}. \tag{4.19}$$

If we set the gain and arm dynamics according to scaling factor k and n

$$\begin{bmatrix} m_m \\ b_m \\ D_{1m} \\ D_{2m} \\ K_m \end{bmatrix} = \frac{k}{n} \begin{bmatrix} m_s \\ b_s \\ D_{1s} \\ D_{2s} \\ K_s \end{bmatrix}, \tag{4.20}$$

the impedance matrix is calculated by

$$\boldsymbol{Z} = \begin{bmatrix} \frac{k}{n}(m_s s + b_s + D_{1s} + \frac{K_s}{s}) & kK_s e^{sT_2}/s \\ \frac{1}{n}K_s e^{sT_1}/s & m_s s + b_s + D_{1s} + \frac{K_s}{s} \end{bmatrix}. \tag{4.21}$$

and results in

$$\Delta H = \frac{k}{n}. \tag{4.22}$$

Here, ΔH is constant for any ω. Considering (4.15), the evaluation with $\boldsymbol{H}$ has the same meaning as that with $\boldsymbol{G}$. Therefore, when we set the gain and arm

dynamics according to (4.20), asymmetrical teleoperator performance under the 4 constraint conditions (master free / fixed, slave free / fixed) can be evaluated by either the $\boldsymbol{H}$ or the $\boldsymbol{G}$ matrix.

Appendix 4B. Simulation on other conditions

We conducted a 1-DOF simulation with a rigid wall. The slave environment is a stiff elastic wall ($C_w = 10000$ N/m). An operator force with 1 N is inputted to the master arm for 10 s. Case 5 is a PD controller with grounded damping (Type A controller) and Case 6 is a PD controller with grounded and relative damping (Type B controller). The gain setting is the same as section 4.4.2. Fig. 4.21 shows the simulation results. Fig. 4.21 is similar to Fig. 4.7. No significant difference can be seen.

In Fig. 4.7, significant oscillation can be seen. In the simulation of Fig. 4.7, we set the damping of the operator dynamics and slave side environment to be 0 to demonstrate clear and simple teleoperator performance. In practice these conditions are not realistic. Here, we conducted a 1-DOF simulation with more realistic conditions. We added damping to both operator dynamics and environment dynamics. Fig. 4.22 shows the simulation results. The oscillation is significantly less than Fig. 4.7. Therefore, in a realistic condition with damping in the operator and environment sides, the oscillation, as seen in Fig. 4.7, does not occur, and the operator can conduct the teleoperation.

Appendix 4C. The passivity of a 2-DOF Teleoperator

In this section, we see the stability of a 2-DOF teleoperator is derived from utilization of the passivity of the 1-DOF teleoperator discussed in the text. Fig. 4.23 shows a block diagram of the 2-DOF master-slave system. In Fig. 4.23, M_{ii} is effective inertia, M_{ij} is coupling inertia, h_{ijj} is the centrifugal acceleration coefficient and $h_{ijk}(j \neq k)$ is the coriolis acceleration coefficient of each arm. The 1-DOF teleoperator analyzed in the text is shown in the box with a dashed line. The dynamics of the coupling between links 1 and 2 are shown within the box with a dotted line.

From the passivity of a 1-DOF teleoperator, the arm coupling dynamics and the slave side environment, we obtain the following equations:

$$\int_0^\infty (\tau'_{m1}(t)\dot{\theta}_{m1}(t) - \tau'_{s1}(t)\dot{\theta}_{s1}(t))dt \geq 0 \tag{4.23}$$

$$\int_0^\infty (\tau'_{m2}(t)\dot{\theta}_{m2}(t) - \tau'_{s2}(t)\dot{\theta}_{s2}(t))dt \geq 0 \tag{4.24}$$

$$\int_0^\infty (\tau'_{m1}(t)\dot{\theta}_{m1}(t) + \tau'_{m2}(t)\dot{\theta}_{m2}(t) - \tau''_{m1}(t)\dot{\theta}_{m1}(t) - \tau''_{m2}(t)\dot{\theta}_{m2}(t))dt \geq 0 \tag{4.25}$$

$$\int_0^\infty (\tau'_{s1}(t)\dot{\theta}_{s1}(t) + \tau'_{s2}(t)\dot{\theta}_{s2}(t) - \tau''_{s1}(t)\dot{\theta}_{s1}(t) - \tau''_{s2}(t)\dot{\theta}_{s2}(t))dt \geq 0 \tag{4.26}$$

$$\int_0^t (\tau''_{s1}(t)\dot{\theta}_{s1}(t) + \tau''_{s2}(t)\dot{\theta}_{s2}(t))dt \geq 0 \ . \tag{4.27}$$

We used the definition of passivity in the $n-$port network in Anderson and Spong [1]. From (4.23) $\sim$(4.27), we derive

$$\int_0^t (\tau''_{m1}(t)\dot{\theta}_{m1}(t) + \tau''_{m2}(t)\dot{\theta}_{m2}(t))dt \geq 0 \ . \tag{4.28}$$

Equation (4.28) indicates the 2-DOF master-slave system is passive with regard to input by the operator. Thus, we come to the conclusion that 2-DOF master slave systems are stable.

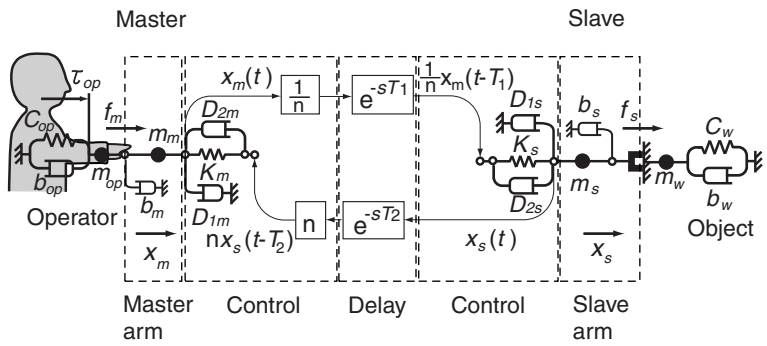

Figure 4.20: Scaled bilateral master slave system with PD controller.

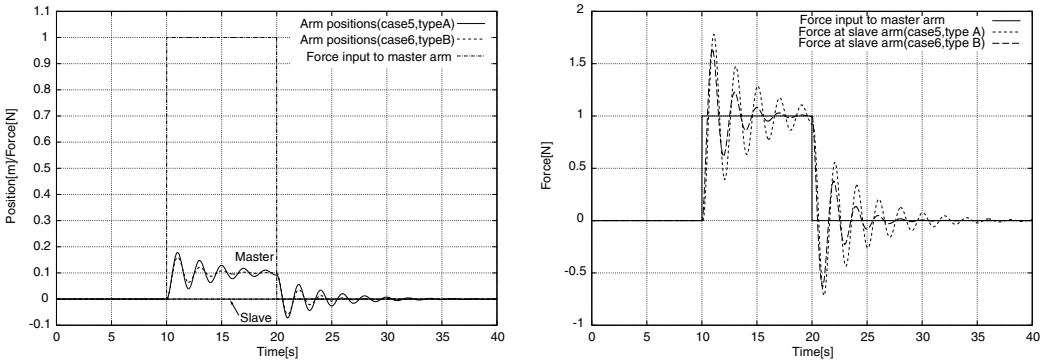

(a) (b)

Figure 4.21: Simulation results of rigid wall contact ($C_w = 10000N/m$).

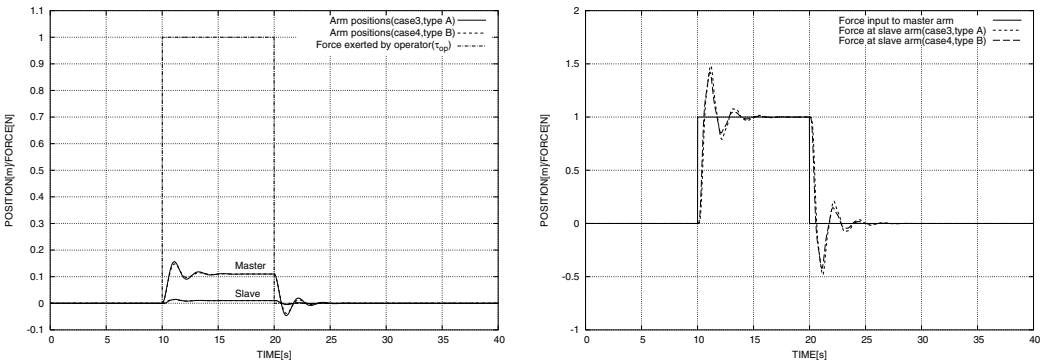

(a) (b)

Figure 4.22: Simulation results of operator dynamics with damping (C_w =100 N/m, b_w = 1 N·s/m, b_{op} = 1 N·s/m).

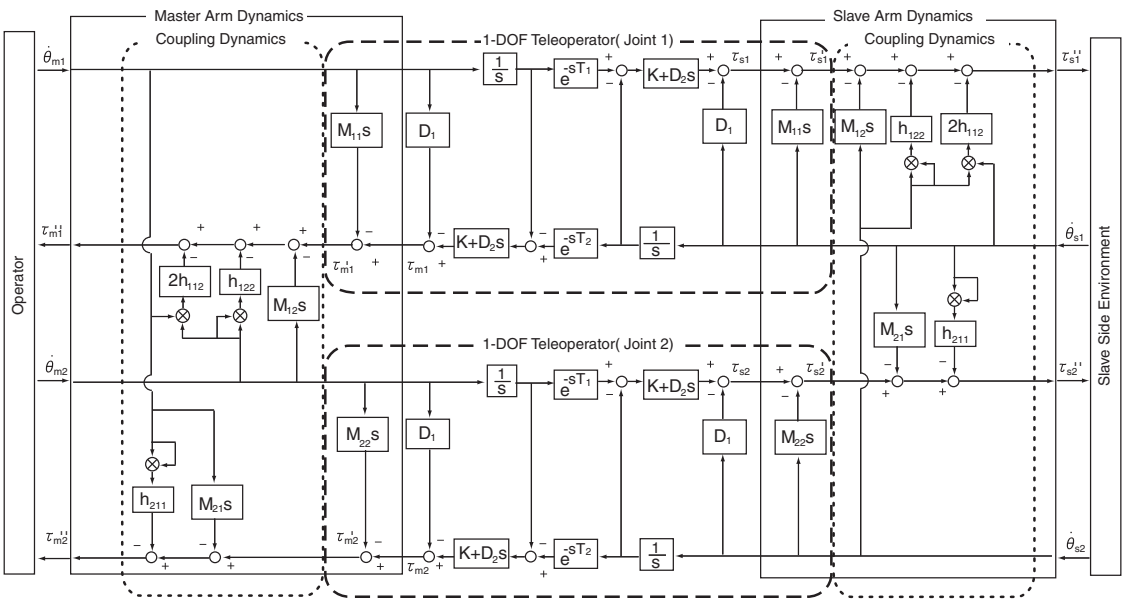

Figure 4.23: 2-DOF master slave system with PD controller.

Appendix 4D. Stability with various time delay conditions

In the stability analyses, simulations and experiments in the text, we assume T_1=T_2, and they are constant and known delays. From the discussion in sections 2.4 and 4.2 as well as (2.32) and (4.6), the stability with other delay conditions is shown in Table 4.7.

As shown in the (*) column in Table 4.7, with a type B controller, if the real time delay T (=T_1=T_2) is shorter than the delay T_e used in the stability derivation, the system stability is maintained as shown in the following.

Assume a stable master slave system under delay T_e. From (24), we obtain

$$D_1 + b_2 \geq \max_{\omega>0} |D_2 \cos \omega T_e - \frac{KT_e}{\omega T_e} \sin \omega T_e| - D_2 \ . \tag{4.29}$$

Let

$$T_e > T \tag{4.30}$$

$$\max_{\omega>0} |D_2 \cos \omega T - \frac{KT}{\omega T} \sin \omega T| = M_1 \tag{4.31}$$

$$\max_{\omega>0} |D_2 \cos \omega T_e - \frac{KT_e}{\omega T_e} \sin \omega T_e| = M_2 \ . \tag{4.32}$$

From $D_2 \cos \omega T - \frac{KT}{\omega T} \sin \omega T = \sqrt{{D_2}^2 + (\frac{KT}{\omega T})^2} \cos(\omega T + \alpha)$, we obtain

$$M_1 > D_2 \tag{4.33}$$

where

$$\cos \alpha = D_2 / \sqrt{{D_2}^2 + (\frac{KT}{\omega T})^2} \tag{4.34}$$

$$\sin \alpha = \frac{KT}{\omega T} / \sqrt{{D_2}^2 + (\frac{KT}{\omega T})^2} \ . \tag{4.35}$$

Assume ω_0 is the value which brings the maximum value of (4.31), see Fig. 4.24. Then

$$|D_2 \cos \omega_0 T - \frac{KT}{\omega_0 T} \sin \omega_0 T| = M_1 \ . \tag{4.36}$$

We introduce ω_1 and assume $\omega_0 T = \omega_1 T_e$, and we have

$$|D_2 \cos\omega_1 T_e - \frac{KT_e}{\omega_1 T_e}\sin\omega_1 T_e| = |D_2 \cos\omega_0 T - \frac{KT_e}{\omega_0 T}\sin\omega_0 T| \tag{4.37}$$

$$= |D_2 \cos\omega_0 T - \frac{KT}{\omega_0 T}\sin\omega_0 T - \frac{K(T_e - T)}{\omega_0 T}\sin\omega_0 T| \ . \tag{4.38}$$

From (4.33) and (4.36), $D_2 \cos\omega_0 T$ and $-\frac{KT}{\omega_0 T}\sin\omega_0 T$ have the same sign. Then, $-\frac{K(T_e - T)}{\omega_0 T}\sin\omega_0 T$ has the same sign. Therefore,

$$|D_2 \cos\omega_1 T_e - \frac{KT_e}{\omega_1 T_e}\sin\omega_1 T_e| = |D_2 \cos\omega_0 T - \frac{KT}{\omega_0 T}\sin\omega_0 T| + |\frac{K(T_e - T)}{\omega_0 T}\sin\omega_0 T| \tag{4.39}$$

$$> |D_2 \cos\omega_0 T - \frac{KT}{\omega_0 T}\sin\omega_0 T| = M_1 \ . \tag{4.40}$$

From (4.32) and inequality (4.40), we obtain

$$M_2 > M_1 \ . \tag{4.41}$$

From (4.29), (4.31), (4.32) and (4.41), we have

$$D_1 + b_2 > \max_{\omega > 0} |D_2 \cos\omega T - \frac{KT}{\omega T}\sin\omega T| - D_2 \ . \tag{4.42}$$

Therefore, we conclude that the system is stable even if the real delay T is shorter than the delay T_e used in the stability derivation.

Table 4.7: Stability of Type A and Type B controller with various time delay conditions

condition		Type A controller (PD controller with only grounded damping)	Type B controller (PD controller with grounded and relative damping)
T_1 and T_2 are constant	$T_1 \neq T_2$	Not T_1 and T_2 but $T_1 + T_2$ decides the stability.	When $T_1 \neq T_2$, the stability condition is not simple as shown in eq.(23) and (24).
	T_1,T_2 are unknown	Gains can be calculated with only $T_1 + T_2$.	The stability is affected by T_1 and T_2. Therefore, the values T_1,T_2 must be acquired.
	There is a difference between T_1 and T_2 used in the stability derivation and actual values of T_1 and T_2	Stability is maintained $T_1 + T_2$(actual) $\leq$ $T_1 + T_2$(used in stability derivation)	In general, the stability is not guaranteed. If T_1=T_2=T and T is shorter than the delay used in stability derivation, the stability is maintained.(*)
T_1,T_2 are time-variant		Not assumed in this work.	Not assumed in this work.

(*) Derivation is shown in Appendix.D.

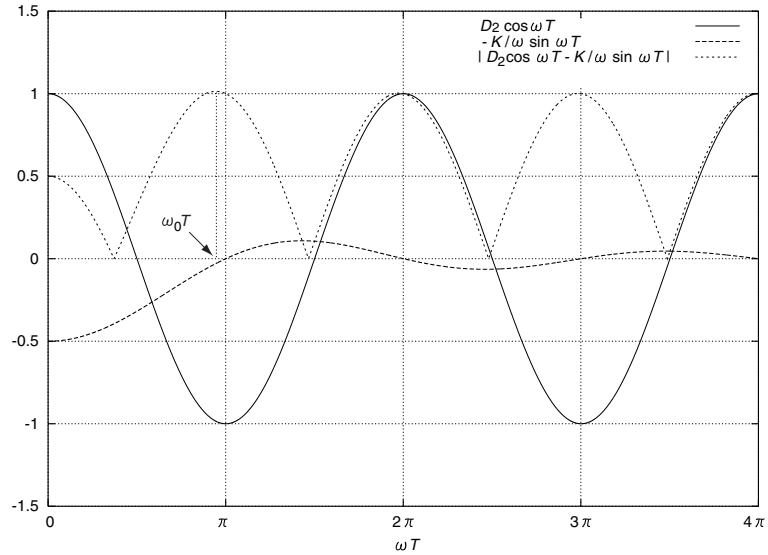

Figure 4.24: Numerical calculation results. The elements of stability condition (24) are shown. $K = 10$ N/m, $D_2 = 1.0$ N· s/m, $T = 0.05$ s.

Chapter 5

Performance improvement of PD-based bilateral teleoperator with time delay by introducing high pass filter

5.1 Introduction

With the well-known approach of delayed bilateral teleoperator by Anderson and Spong, further developed by Niemeyer and Slotine, large inertial characteristic of the control law degrade the performance as the delay become large, see Appendix A. On the other hand, even under large time delay such as several seconds, PD-based controller does not show such a behavior. Therefore, PD control is potentially applicable under long time delay and we focused on PD controllers. However, with PD control approach, as the delay becomes large, the damping gain become large and the conservativeness of the control law is a problem and it needs to be improved to utilize the bilateral control.

In the previous chapters, we derived the stable PD controller conditions with grounded and relative damping, improved the performance of PD control and clarified the effect of the addition of relative damping.

This chapter studies the performance improvement by introducing high pass filter into PD controller. Teleoperator stability condition of new PD controller with

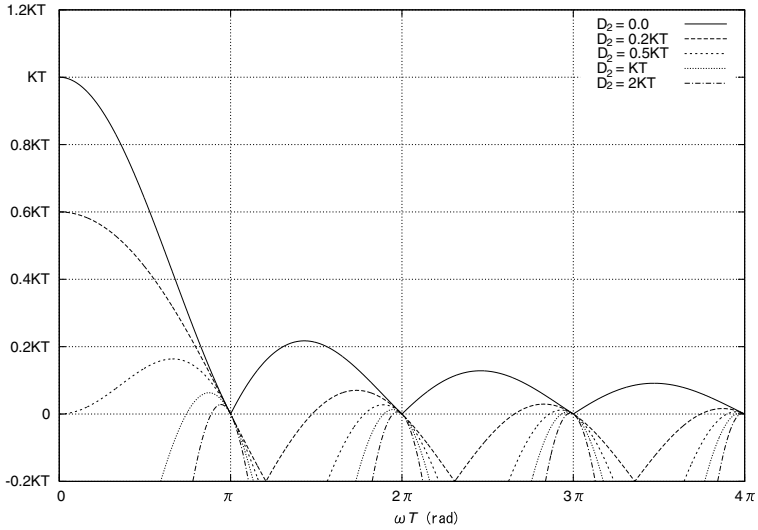

Figure 5.1: Numerical calculation results on the right side of eq. (4.6) (T=1.0 s, K=10.0 N/m).

HPF is derived. We will show that the introduction of HPF improves the performance of teleoperator and maintains the stability of a system, with less grounded damping viscousness. The teleoperator performance is studied by a transparency analysis using hybrid matrices expression and 1-DOF simulations. Finally, peg-in-hole experiments are conducted to evaluate the validity of these methods in a realistic multi-DOF condition.

In this chapter, we assume the delay is constant, the delay value is known, and the delay from master to slave and the delay from slave master are equal.

5.2 Performance improvement by introducing high pass filter into PD-controller

With the controller shown in sections 2.4 and 4.2, large grounded damping degrades the performance of the teleoperator. Therefore, in this section, we study the performance improvement by optimizing the frequency characteristics of the grounded damping.

In Fig. 5.1, the numerical calculation results on the right side of (4.6) are shown. In this calculation, the parameters used are D_2 =0.0, $0.2KT$, $0.5KT$,

KT and $2KT$ N·s/m. The case $D_2 = 0.0$ corresponds to a PD controller with only grounded damping, see Section 2.4. The calculation shows that the grounded damping gain D_1 can be set smaller as a relative damping gain D_2 increases from zero.

As shown in Fig.5.1, if we set $D_2 \geq 1/2KT$, ground damping gain at $\omega \to 0$ can be attenuated to zero with maintained stability, if the grounded damping gain is set large enough at $\forall\omega > 0$ such that the stability condition(4.6) is satisfied. Therefore, we newly introduce high pass filter into the PD-controller shown in section 4.2. Here, we derive the stability condition of PD-type controller with grounded damping and relative damping with HPF. The physical interpretation of this controller is shown in Fig. 5.2. The block diagram of the teleoperator is shown in Fig. 5.3. As shown in Figs. 5.2 and 5.3, we inserted a velocity HPF into the velocity input of grounded damping.

This type of PD-type controller is given by the following equations:

$$\begin{aligned} \tau_m &= -K_m(x_m(t) - x_s(t - T_2)) \\ &\quad -D_{2m}(\dot{x}_m(t) - \dot{x}_s(t - T_2)) - D_{1m}\mathcal{H}(\dot{x}_m) \end{aligned} \tag{5.1}$$

$$\begin{aligned} \tau_s &= K_s(x_m(t - T_1) - x_s(t)) \\ &\quad +D_{2s}(\dot{x}_m(t - T_1) - \dot{x}_s(t)) - D_{1s}\mathcal{H}(\dot{x}_s) \end{aligned} \tag{5.2}$$

where $\mathcal{H}(\ )$ denotes the high pass filter.

As high pass filter, we used washout filter $\frac{\tau s}{1+\tau s}$. Then elements of the impedance matrix are

$$\begin{aligned} z_{11} &= m_m s + b_m + \frac{\tau s}{1+\tau s} D_{1m} + D_{2m} + \frac{K_m}{s} \\ z_{12} &= (\frac{K_m}{s} + D_{2m})e^{-sT_2} \\ z_{21} &= (\frac{K_s}{s} + D_{2s})e^{-sT_1} \\ z_{22} &= m_s s + b_s + \frac{\tau s}{1+\tau s} D_{1s} + D_{2s} + \frac{K_s}{s} \ . \end{aligned} \tag{5.3}$$

For simplicity, we consider the above to be a symmetrical system, i.e. $K_m = K_s = K, D_{1m} = D_{1s} = D_1, D_{2m} = D_{2s} = D_2$, and $T_1 = T_2 = T$.

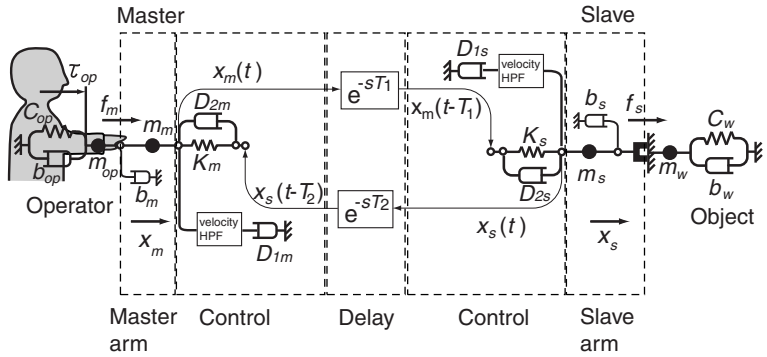

Figure 5.2: Master slave system with PD controller with grounded and relative damping gain. The velocity input to the grounded damping gain is high pass-filtered.

Applying Llewellyn's criteria to (5.3), the teleoperator is stable for passive terminations if the following conditions are satisfied at all frequencies:

$$\frac{\tau^2\omega^2}{1+\tau^2\omega^2}D_1 + b + D_2 \geq 0 \tag{5.4}$$

$$(\frac{\tau^2\omega^2}{1+\tau^2\omega^2}D_1 + b + D_2)^2 \geq (D_2\cos\omega T - \frac{K}{\omega}\sin\omega T)^2 \ . \tag{5.5}$$

Eq. (5.5) can be rewritten as follows:

$$\frac{\tau^2\omega^2}{1+\tau^2\omega^2}D_1 + b \geq |D_2\cos\omega T - \frac{K}{\omega}\sin\omega T| - D_2 \ . \tag{5.6}$$

By solving (5.6) numerically, we find parameters D_1 and D_2 satisfy (5.4) and (5.5) under given K, T, and b .

In Fig. 5.4, the numerical calculation results on the left and right side of (5.6) are shown. In this calculation, the parameters used are $T = 1.0$ s, $K = 10.0$ N/m, D_1 =2.00 N·s/m, D_2 =5.00 N·s/m, $\tau = 1.5$ s and $b = 0.00$ N·s/m. From Fig. 5.4, the stability condition is satisfied and we can design the stable controller.

By adding HPF into grounded damping, the conservativeness of the controller is improved. The performance will be discussed in the following sections.

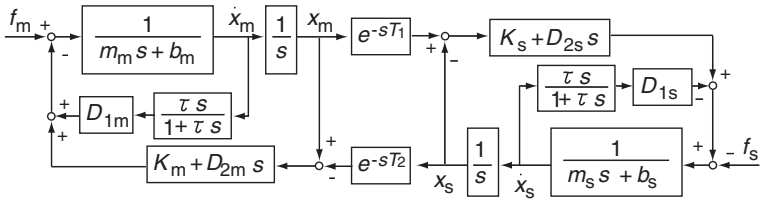

Figure 5.3: Block diagram of master slave system with PD controller with high pass filter.

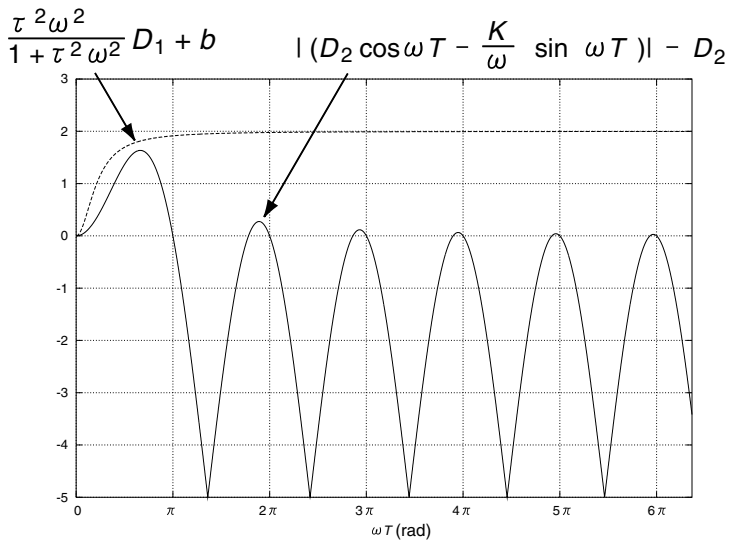

Figure 5.4: calculation result of stability condition with PD control law with HPF

5.3 Teleoperator transparency as a performance measurement and evaluation using hybrid matrix

In this section, we introduce the performance measurement by hybrid matrix expression and evaluate the improvement of PD controllers with HPF.

To measure the performance of the teleoperator with time delay quantitatively, we use the performance evaluation with the hybrid matrix $\boldsymbol{H}$, as proposed by Hannaford [7] as in the previous chapter.

5.3.1 Performance measurement using $\boldsymbol{H}$ matrix

The teleoperator can be expressed by a hybrid matrix

$$\begin{bmatrix} V_m \\ -I_s \end{bmatrix} = \begin{bmatrix} h_{11} & h_{12} \\ h_{21} & h_{22} \end{bmatrix} \begin{bmatrix} I_m \\ V_s \end{bmatrix} \tag{5.7}$$

where $\boldsymbol{H} = [h_{ij}]$ is the hybrid matrix of the teleoperator. The physical interpretation of h_{ij} is shown in Table 4.1.

If complete teleoperator transparency is achieved, the hybrid matrix becomes as follows:

$$\boldsymbol{H}_{ideal} = \begin{bmatrix} 0 & 1 \\ -1 & 0 \end{bmatrix} . \tag{5.8}$$

Therefore, teleoperator performance can be evaluated by how close the elements of the hybrid matrix are to the ideal values of $\boldsymbol{H}_{ideal}$.

From (5.3), the elements of the hybrid matrix of the teleoperator, see Section 5.2, are calculated as follows:

$$\begin{aligned} h_{11} &= M_m s + D_{2m} + \frac{\tau s}{1+\tau s} D_{1m} + b_m + \frac{K_m}{s} \\ &\quad - \frac{(D_{2s} + \frac{K_s}{s})(D_{2m} + \frac{K_m}{s}) e^{-s(T_1+T_2)}}{M_s s + \frac{\tau s}{1+\tau s} D_{1s} + b_s + D_{2s} + \frac{K_s}{s}} \end{aligned} \tag{5.9}$$

$$h_{12} = \frac{(D_{2m} + \frac{K_m}{s}) e^{-sT_2}}{M_s s + \frac{\tau s}{1+\tau s} D_{1s} + b_s + D_{2s} + \frac{K_s}{s}} \tag{5.10}$$

$$h_{21} = -\frac{(D_{2s} + \frac{K_s}{s}) e^{-sT_1}}{M_s s + \frac{\tau s}{1+\tau s} D_{1s} + b_s + D_{2s} + \frac{K_s}{s}} \tag{5.11}$$

$$h_{22} = \frac{1}{M_s s + \frac{\tau s}{1+\tau s} D_{1s} + b_s + D_{2s} + \frac{K_s}{s}} . \tag{5.12}$$

The values of $h_{11}, \cdots, h_{22}$ depend upon the frequency ω. We calculate the limit of $h_{11}, \cdots, h_{22}$ as $\omega \to 0$ and $\omega \to \infty$ limit as shown in Table 5.1. In Table 5.1, the limits of the PD-controller without the HPF are also shown. In the far right column, the ideal values are shown. In case of the teleoperation with a time delay, the manipulation speed becomes slower because of the delay, therefore $h_{ij}(\omega \to 0)$ values are important. Longer delays cause a larger damping gain D_1, a larger $|h_{11}|$ and result in performance degradation. This means that the master arm responds in a resistant manner, even when the slave arm is free. We know that, by introducing

HPF into PD-controller, $h_{11}(\omega \leftarrow 0)$ value become smaller by $D_{1m} + \frac{K_m(D_{1s}+b_s)}{K_s}$. From this, we know that, the transparency under the slave arm free condition is significantly improved by introducing the HPF.

5.3.2 Performance measurement using $\boldsymbol{G}$ matrix

In another expression, the teleoperator can be expressed using the $\boldsymbol{G}$ matrix:

$$\begin{bmatrix} I_m \\ V_s \end{bmatrix} = \begin{bmatrix} g_{11} & g_{12} \\ g_{21} & g_{22} \end{bmatrix} \begin{bmatrix} V_m \\ -I_s \end{bmatrix} \tag{5.13}$$

where $\boldsymbol{G} = [g_{ij}]$ is the inverse hybrid matrix of the teleoperator.

Using $\boldsymbol{G}$ matrix, we can evaluate the performance when the master arm is free and the slave arm is constrained, see Table 4.1.

If the complete transparency of the teleoperator is achieved, the inverse hybrid matrix becomes as follows:

$$\boldsymbol{G}_{ideal} = \begin{bmatrix} 0 & -1 \\ 1 & 0 \end{bmatrix} . \tag{5.14}$$

The limits of $g_{11}, \cdots, g_{22}$ as $\omega \to 0$ and $\omega \to \infty$ are shown in Table 5.1.

We know that, by introducing HPF into PD-controller, $g_{22}(\omega \leftarrow 0)$ value become smaller by $D_{1s} + \frac{K_s(D_{1m}+b_m)}{K_m}$ and approaches the ideal value.

5.4 Controller design and performance comparison study using frequency-dependent $\boldsymbol{H}$ matrix

In this section, we design two controllers. One is PD controller without HPF and the other is PD controller with HPF. Then, we calculate $\boldsymbol{H}$ matrix for each controller numerically and compare the performances.

5.4.1 Controller design

We assume the time delay $T_1 = T_2 = T = 1.0$ s, the arm inertia $M_m = M_s = M = 1$ kg, and the mechanism viscous coefficient $b_m = b_s = b = 0$ N·s/m.

We designed two controllers. Type A controller is a PD controller with grounded and relative damping, as shown in Section 4.2. Type B controller is a PD controller with grounded and relative damping with HPF, as shown in Section 5.2. With both types, we set the controller proportional gain, $K_m = K_s = K = 10$ N/m. With type A, we set D_2 to satisfy condition (4.6). With type B controller, we set D_1, D_2 and τ as shown in Section 5.2.

Table 5.2 shows the controller gains.

5.4.2 Performance comparison study using frequency-dependent $\boldsymbol{H}$ matrix

Fig. 5.5 shows the bode plot of each element of the hybrid matrix for both types of controller. In the low-frequency area, $|h_{11}|$ is closer to the ideal value for a type B controller. The magnitude of h_{11} at $\omega \to 0$ is 23.4 with a type A controller, while it is 20.0 with a type B controller. The ideal value is $|h_{11}| = 0.0$. This means that a type B controller is less conservative than a type A controller in the low frequency region, including $\omega \to 0$. By adding the HPF, the grounded damping can be attenuated and less conservative controller is achieved.

5.4.3 Optimum gain settings of PD controller

Here, we think on the optimum controller design of PD controller. In Fig. 5.6(a), stability gain condition for the PD controller with grounded and relative damping, see section 4.2, is shown. If we set the relative damping gain D_2 higher, grounded damping gain D_1 can be set smaller with maintained stability. However, higher damping gain requires high resolution velocity sensor and there is a limit from hardware performance.

In Fig. 5.6(b), the value $h_{11}(\omega \to 0)$ with the controller in 4.2 is shown with a solid line. D_1 is set so that the controller is on the stability limit (on the line in Fig. 5.6(a)).

As we set D_2 higher, $h_{11}(\omega \to 0)$ become smaller. In Fig 5.6(b), $h_{11}(\omega \to 0)$ value with PD controller with HPF, see section 5.2, is also shown with a dashed line. From Fig 5.6(b), we know that, by introducing HPF in PD controller, $h_{11}(\omega \to 0)$ approaches the ideal value and the performance of teleoperator is improved. If D_2

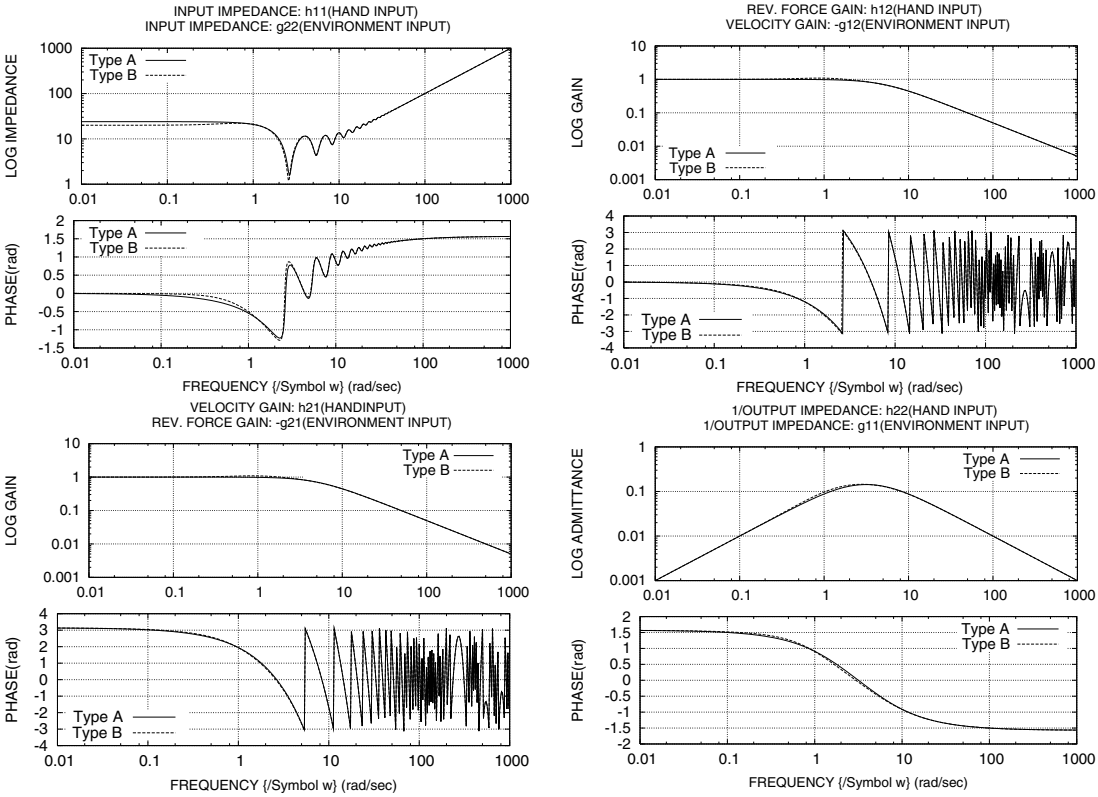

Figure 5.5: Frequency-dependent $\boldsymbol{H}$ and $\boldsymbol{G}$ matrix of a Type A controller (without HPF) and a Type B controller (with HPF).

gain is smaller than 5, the stability is not maintained by the PD-controller with HPF. Therefore, the dashed line starts from $D_2 = 5$ in Fig 5.6(b).

5.5 1-DOF Simulation

5.5.1 Controlled system and controller design

In this section we show the results of 1-DOF numerical simulations. We assume a linear master slave system as shown in Figs. 4.1 and 5.2. To confirm the effect of high pass filter, we compare the two controller types. In the simulations, we assume the same time delay ($T_1 = T_2 = T = 1.0$ s) , the same arm inertia ($M_m = M_s = M = 1$ kg), the same mechanism viscous coefficient ($b_m = b_s = b = 0$ N·s/m) and the same controller gains (Table 5.2) as section 5.4.

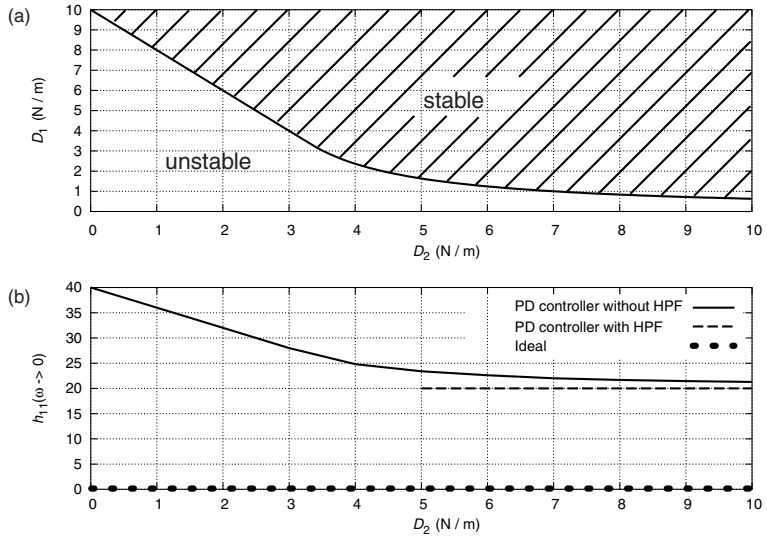

Figure 5.6: Stable gain setting and $h_{11}(\omega \to 0)$ (T=1.0 s, K=10.0 N/m). (a) The grounded damping gain D_1 can be set smaller with large relative damping gain D_2. (b) When D_2 gain is larger than 5.0 ($\frac{1}{2}KT$) (Ns/m), HPF can be applied to the PD control law and the performance evaluated by $h_{11}(\omega \to 0)$ is improved.

5.5.2 Simulation cases

Using the control law designed in the previous section, we conducted simulations. The tasks were a mass pushing task and a wall pushing task. Table 5.3 shows the simulation cases and parameter settings. To compare the controller performance using two environmental settings, we calculated four simulation cases. In all cases, the initial state is $x_m = 0$, $x_s = 0$, $\dot{x}_m = 0$, and $\dot{x}_s = 0$.

We set the slave environment as in Table 5.3. In cases 1 and 2, the slave environment is a simple mass hold. In case 3 and 4, the slave arm is constrained by an elastic wall. The natural position of the elastic wall is $x_s = 0$.

5.5.3 Simulation result and discussion

Figs. 5.7 and 5.8 show the simulation results of the mass pushing task and the wall pushing task. In Figs. 5.7 and 5.8, the ideal response is the master arm position and the slave position are the same, and the force at the master arm and

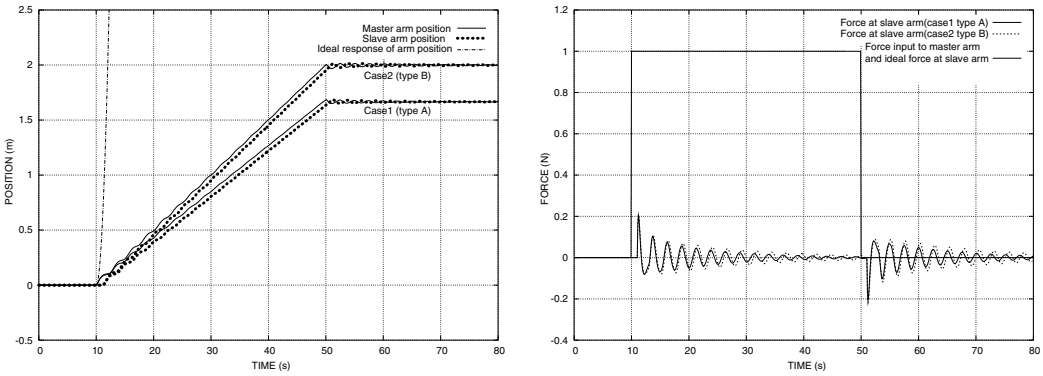

(a) (b)

Figure 5.7: Simulation results. The slave environment is mass hold. Operator force of 1N is inputted to the master arm from 10 s until 50s. Case 1 is PD without HPF and Case 2 is PD with HPF.

the force at slave arm are the same. With both controller, the task is completed with stability even under the long delay of 1 sec. In the mass pushing task, the mass moves slower than the ideal response because of the viscous force of the damping gain and the inertia of the arms. However, the mass moves more quickly with the type B controller than the type A. This result agrees with the low-frequency h_{11} value in Fig. 5.5. The simulation results and performance evaluation results of $\boldsymbol{H}$ are consistent. As for wall pushing task, the overshoot is a little larger with type B controller, however, there is not a significant difference.

5.6 2-DOF peg in hole experiment

5.6.1 Experimental system and experimental cases

To confirm the effectiveness of the proposed control law in a realistic multi-DOF plant, we conducted a 2-DOF peg-in-hole task. Fig. 5.9 shows the experiment setup. The master and slave arms are 3-DOF planar-type manipulators with electric motors, harmonic-drive reduction gears, and an encoder at each joint. In this experiment, the wrist joints (J3) are fixed, and only 2 DOFs are used. We used the same robot and computer hardware as in section 4.5.1. The time delay is calculated with software. The signals are buffered in the memory for the time

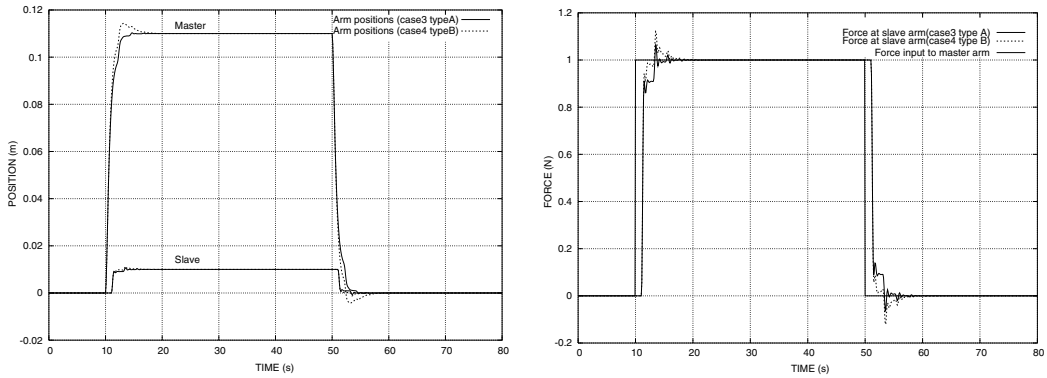

(a) (b)

Figure 5.8: Simulation results. The slave environment is an elastic wall. Operator force of 1N is inputted to the master arm from 10 s until 50s. Case 3 is PD without HPF and Case 4 is PD with HPF.

delay. As shown in Fig. 5.9, the master and the slave arms move symmetrically, therefore the direction of x_m and x_s are opposite. Table 5.4 shows the experimental cases and their gain settings. The controller gain of joint 1 and 2 are the same. Each time delay from master to slave and from slave to master is 1 s. The control law calculation frequency is 1 kHz. With type B controller, the high pass filter is realised by tustin (bilinear) transformation. As a peg, an aluminum disk of 74 mm diameter is attached at the slave arm tip. The hole, an opening of 74 mm gap is in a wall, see Fig. 5.9. The desired task is to push the wall in +y direction, trace the wall toward −x direction, and insert the peg into the hole. The arm lengths are shown in Fig. 5.9. The parameters of the master and the slave are the same. The operator's view is shown in Fig. 5.10.

5.6.2 Experimental results and discussions

In each cases, we conduct the same experiment 3 times. With all 6 trials, we could successfully complete the peg in hole task with stability. In Fig.5.11, task completion time and average position deviation between master arm tip and slave arm tip are shown. In Figs.5.12 and 5.13, typical arm tip trajectories of master and slave are shown. In Fig. 5.14, motor command average deviations between

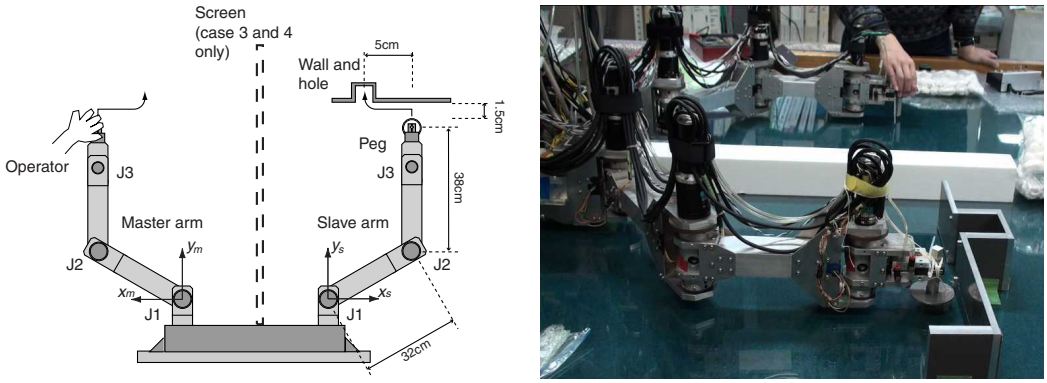

(a) Task and initial position (b) Experiment

Figure 5.9: Setup of 2-DOF peg-in-hole experiment.

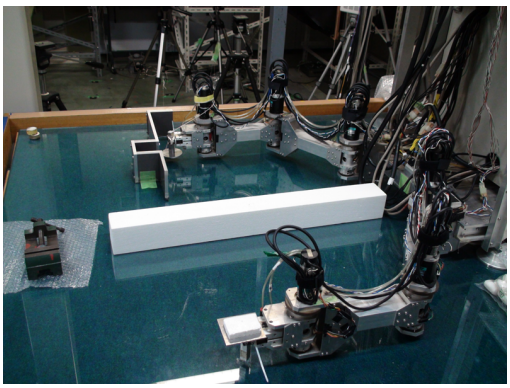

Figure 5.10: Operator's view of slave side.

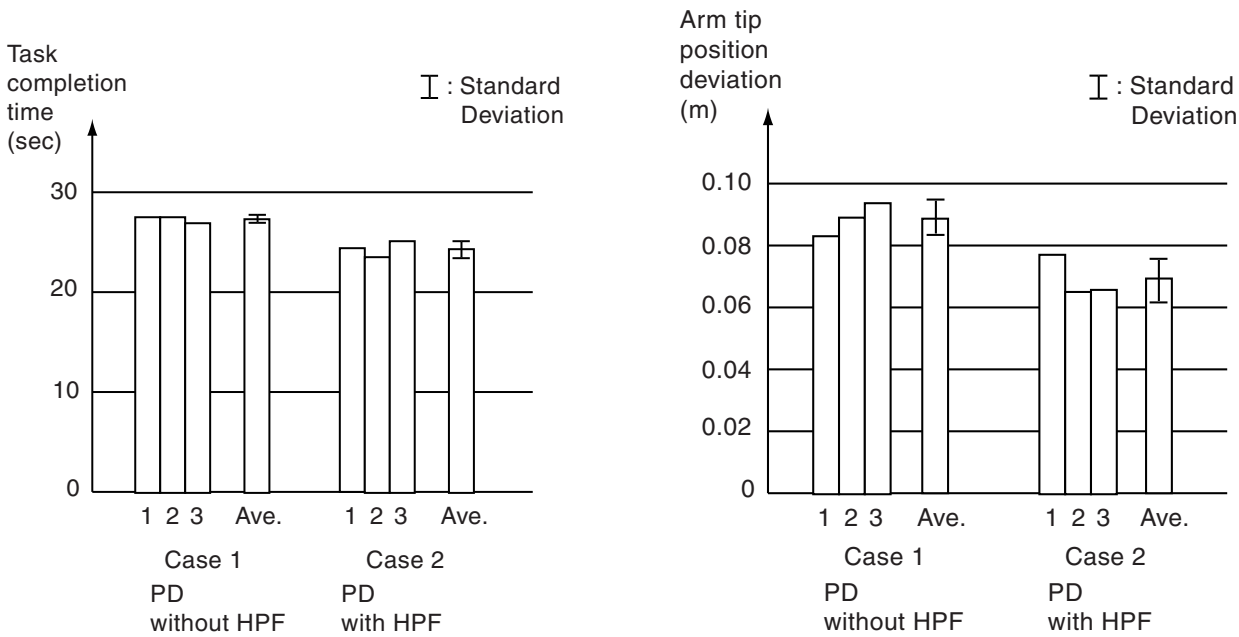

(a) Task completion time (b) Position deviation between master and slave arm

Figure 5.11: 2-DOF experimental results. Task completion time and arm tip position deviation: 3 time trials and their average value is shown. Task completion time and arm position deviation are smaller with type B controller than type A controller.

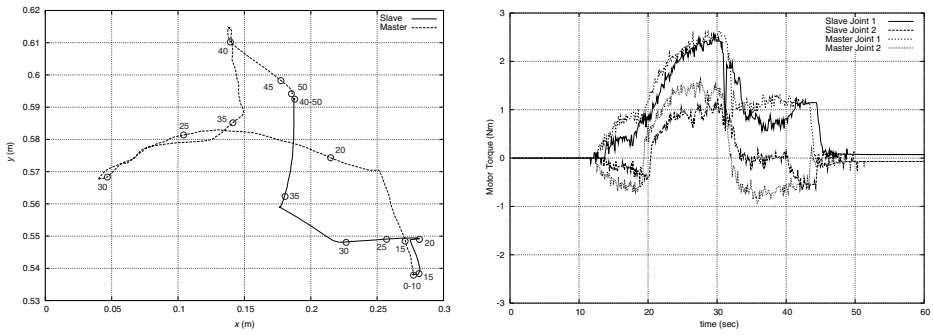

(a) Arm tip trajectory (b) Motor command

Figure 5.12: 2-DOF peg-in-hole experiment results (Type A Controller). The adjacent numbers of circles in figure (a) are the experimental time from the beginning.

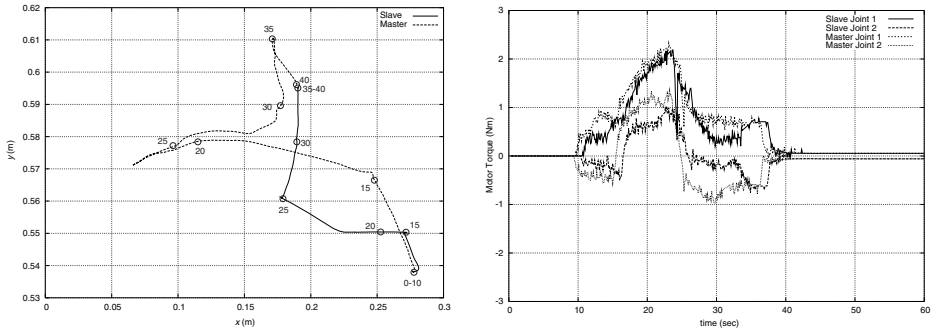

(a) Arm tip trajectory (b) Motor command

Figure 5.13: 2-DOF peg-in-hole experiment results (Type B controller). The adjacent numbers of circles in figure (a) are the experimental time from the beginning.

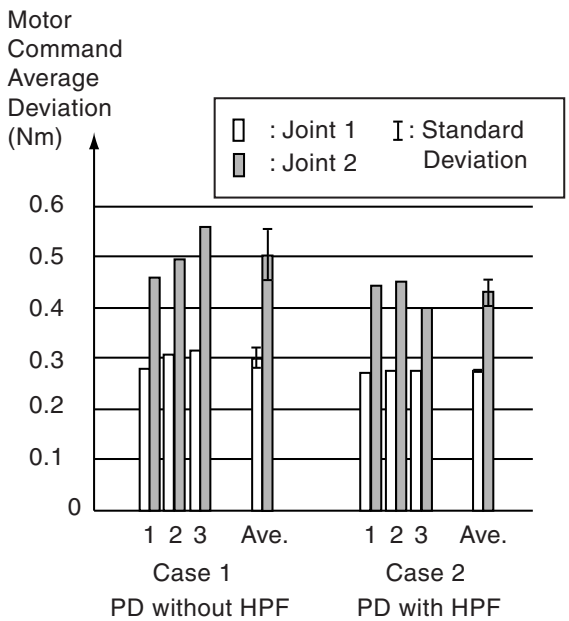

Figure 5.14: 2-DOF experimental results. Motor command average deviation between master and slave (3 time trials and average values) are illustrated. The deviation is smaller with Type B controller than Type A controller.

master and slave are shown. As known from Figs. 5.11 and 5.14, type B controller shows better performance than type A for task completion time, position tracking error and force tracking error.

5.7 Conclusion

The performance improvement by introducing a HPF into relative damper in a PD-based teleoperator with time delay has been studied. First, we derived the stability condition of a PD-based controller with HPF. Second, performance evaluation was conducted using a hybrid matrix. As a result, we showed that introducing HPF into a PD-based controller improved the performance of the teleoperator, especially in low frequency region. Third, optimum gain setting for grounded and relative damping was discussed. Finally, to evaluate teleoperator performance, we conducted 1-DOF simulations and 2-DOF peg-in-hole experiments. The teleoperator performance was evaluated using these simulations and experiments. These results showed performance improvement was achieved by introducing HPF into PD controller.

Table 5.1: Limit value of hybrid matrix elements of PD-controller shown in Section 4.2 and 5.2 and ideal value achieved by perfect transparency. The values except $h_{11}(\omega \leftarrow 0)$ and $g_{22}(\omega \leftarrow 0)$ are same with both controller.

Matrix	Elements	$\omega \to 0$		$\omega \to \infty$		Ideal value
		Gain	Phase	Gain	Phase	
$\boldsymbol{H}$	h_{11}	$D_{1m} + \frac{K_m(D_{1s}+b_s)}{K_s} + K_m(T_1+T_2)$ (without HPF)	0	$M_m\omega$	$\frac{\pi}{2}$	0
		$K_m(T_1+T_2)$ (with HPF)				
	h_{12}	$\frac{K_m}{K_s}$	0	$K_m/M_s\omega^2$ (if $D_{2m}=0$)	$-\infty$	1
				$D_{2m}/M_s\omega$ (if $D_{2m}\neq 0$)		
	h_{21}	1	π	$K_s/M_s\omega^2$ (if $D_{2s}=0$)	$-\infty$	-1
				$D_{2s}/M_s\omega$ (if $D_{2s}\neq 0$)		
	h_{22}	$\frac{\omega}{K_s}$	$\frac{\pi}{2}$	$\frac{1}{M_s\omega}$	$-\frac{\pi}{2}$	0
$\boldsymbol{G}$	g_{11}	$\frac{\omega}{K_m}$	$\frac{\pi}{2}$	$\frac{1}{M_m\omega}$	$-\frac{\pi}{2}$	0
	g_{12}	1	π	$K_m/M_m\omega^2$ (if $D_{2m}=0$)	$-\infty$	-1
				$D_{2m}/M_m\omega$ (if $D_{2m}\neq 0$)		
	g_{21}	$\frac{K_s}{K_m}$	0	$K_s/M_m\omega^2$ (if $D_{2s}=0$)	$-\infty$	1
				$D_{2s}/M_m\omega$ (if $D_{2s}\neq 0$)		
	g_{22}	$D_{1s} + \frac{K_s(D_{1m}+b_m)}{K_m} + K_s(T_1+T_2)$ (without HPF)	0	$M_s\omega$	$\frac{\pi}{2}$	0
		$K_s(T_1+T_2)$ (with HPF)				

Table 5.2: Gain settings for both controllers: Type A and Type B.

Type	K [N/m]	D_1 [N·s/m]	D_2 [N·s/m]	τ [s]	Description
A	10.0	2.0	5.0	-	PD controller without HPF
B	10.0	2.0	5.0	1.5	PD controller with HPF

Table 5.3: Simulation parameter settings.

Case No.	Controller type	Slave side environment	C_w [N/m]	M_w [kg]	b_w [N·s/m]
1	A	Mass hold	0.0	1.0	0.0
2	B	Mass hold	0.0	1.0	0.0
3	A	Constrained by elastic wall	100.0	0.0	0.0
4	B	Constrained by elastic wall	100.0	0.0	0.0

Table 5.4: 2-DOF peg-in-hole experimental test cases, gain settings and results.

Case No.	Controller type	K [N/rad]	D_1 [N·s/rad]	D_2 [N·s/rad]	τ [sec]	Task completion time	Position deviation	Typical arm tip trajectory	Motor command deviation
1	A	10.0	2.0	5.0	-	Fig. 5.11(a)	Fig. 5.11(b)	Fig. 5.12	Fig. 5.14
2	B	10.0	2.0	5.0	1.5			Fig. 5.13	

Appendix 5A. Characteristics of passivity based controller with long time delay

As well-known stable bilateral controller under time delay condition, there is a passivity based bilateral controller by Niemeyer and Slotine, see Fig.5.15 [21]. In this appendix, we study the performance of this passivity based controller and compare it with PD-controller. The hybrid matrix of their controller is shown in Fig.5.16. From h_{11} value, we know that the controller shows heavy inertial behavior (equivalent to approximately 10 kg) at delay time = 1 sec. In Fig.5.17, the simulation result of contacting wall is shown. The parameters are shown in Table 5.5 and Table 5.6. We selected the proportional gain of the passivity based control law to be the same value as PD-controller in section 5.5. Master dynamics model and slave side environment model are same as section 5.5. Because of the inertia of the controller, it takes long time (about 40sec) to converge the overshoot and vibration of arm position. Fig.5.8 is the corresponding case with PD-controller. In Fig.5.8, the overshoot on contacting the wall converges about 5 sec. Comparing Fig.5.8 and Fig.5.17, we know that the arm positions converge more quickly with PD controller than the control law shown in Fig.5.15.

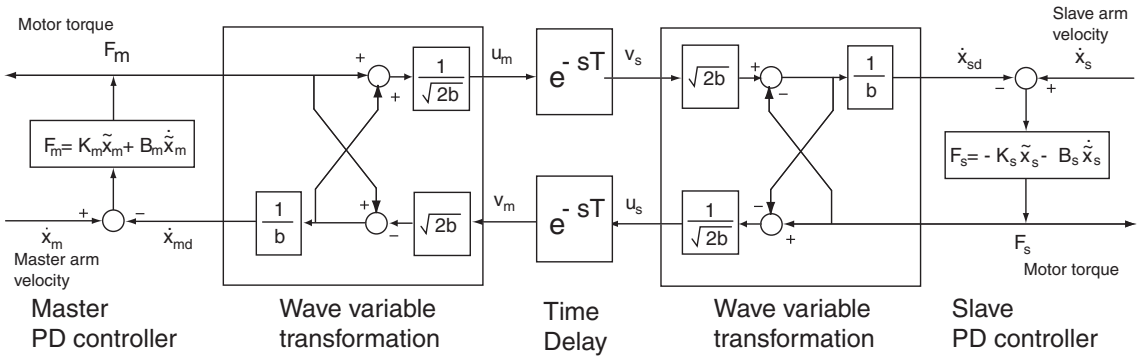

Figure 5.15: Passivity based bilateral controller by Niemeyer and Slotine.

Table 5.5: Parameters of arm dynamics, and gain settings of passivity based controller by Niemeyer and Slotine.

M_m	Master arm inertia	1.0 kg
M_s	Slave arm inertia	1.0 kg
K_m	Master controller proportional gain	10 N/m
K_s	Slave controller proportional gain	10 N/m
B_m	Master controller damping gain	10 Ns/m
B_s	Slave controller damping gain	10 Ns/m
b	Characteristic Impedance of controller	10 N·s/m
b_m	Mechanical viscous coefficient of master arm	0 Ns/m
b_s	Mechanical viscous coefficient of slave arm	0 Ns/m

Table 5.6: Parameters of operator and slave side environment model

C_{op}	Stiffness of operator	0 N/m
B_{op}	Damping of operator	0 N/m · s
M_{op}	Inertia of operator	0 kg
C_w	Stiffness of Slave side environment	100 N/m
B_w	Damping of Slave side environment	0 N/m · s
M_w	Inertia of Slave side environment	0 kg

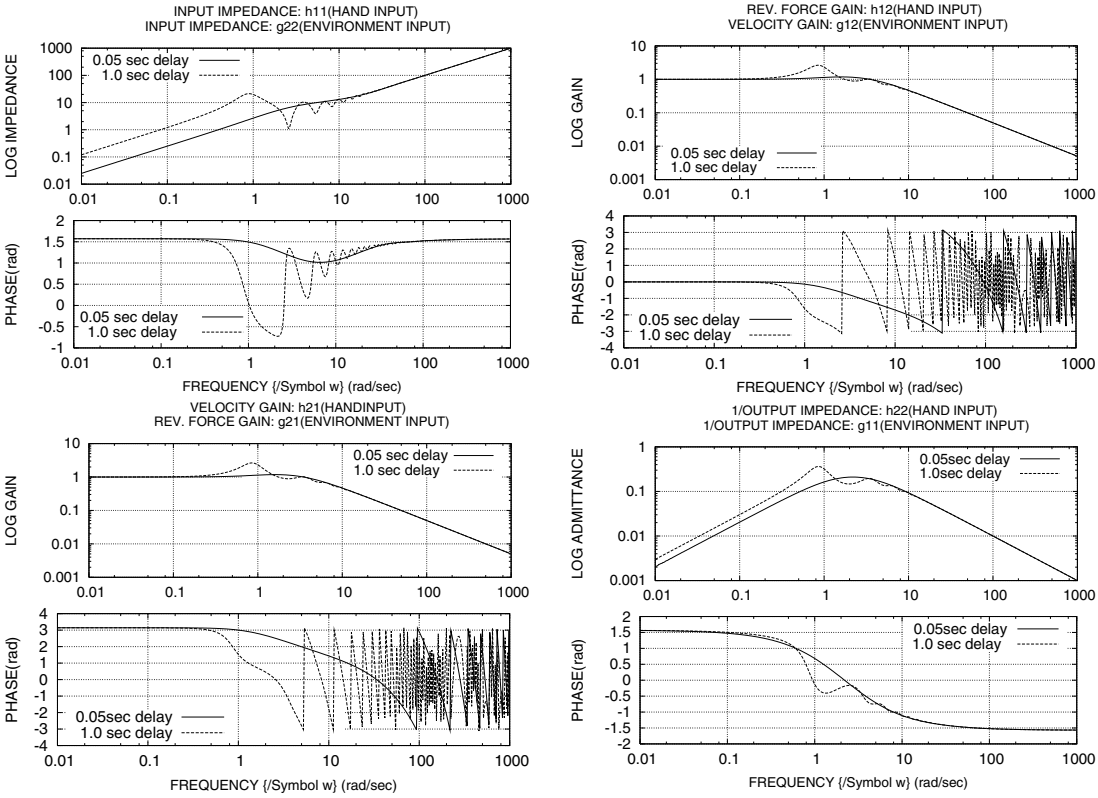

Figure 5.16: Frequency-dependent H and G matrix of passivity-based controller.

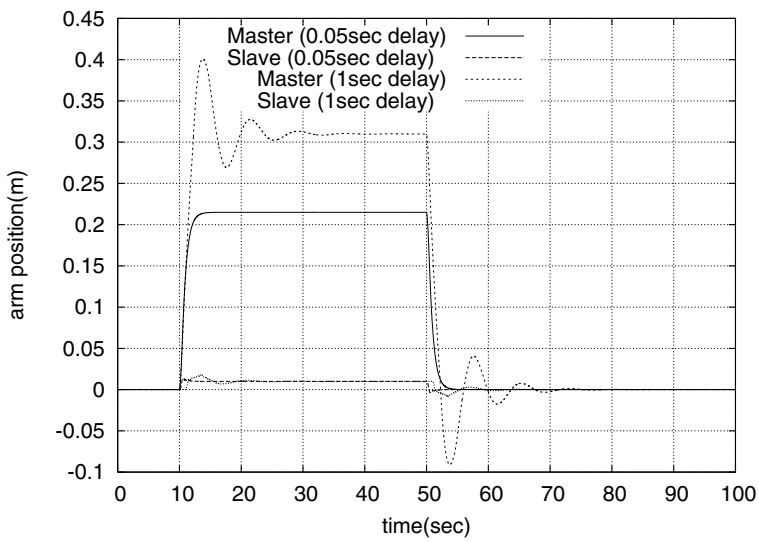

Figure 5.17: Simulation result of passivity-based controller.

Chapter 6

Summary

The major accomplishment of the present thesis is fourfold.

1. Stability condition for a simple PD-type bilateral controller was derived.

2. The results of a ground-space teleoperation experiment using a robot arm mounted on the ETS-VII were shown. Several tasks, such as a slope-tracing task and a peg-in-hole task, were carried out under 6-7 s time-delay conditions. All the tasks were possible by using the direct bilateral control, even without using any visual information. The experimental results demonstrate that force feedback to the operator is still helpful, even under such a long time delay.

3. Performance improvement of PD-type bilateral controller with grounded damping and relative damping are shown. The stability condition is derived. The improvement was evaluated by hybrid matrix and demonstrated by simulation, 1-dof experiment and 2-dof peg-in-hole experiment.

4. The performance improvement of PD-type bilateral controller with high pass filter is shown. The stability condition is derived. The improvement was evaluated by hybrid matrix and demonstrated by simulation and 2-dof peg-in-hole experiment.

The author hopes that some of the difficulties which obstruct the application of the bilateral teleoperation under time delay to practical problems, have been overcome by the present research. However, it is needless to say that further

research should be devoted to this field. The extension of the theory to variable time delay and the further improvement of the conservativeness of PD-control law should be studied.

References

[1] R. J. Anderson and M. W. Spong, "Bilateral Control of Teleoperators with Time Delay," *IEEE Trans. Autom. Control*, vol. 34, no. 5, pp. 494–501, 1989.

[2] E. Folke Bolinder, "Survey of Some Properties of Linear Networks," *IRE Trans. Circuit Theory*, pp. 70–78, 1957.

[3] R. C. Dorf and J. A. Svoboda, *Introduction to Electric Circuits.* 5th ed. John Wiley and Sons, 2001.

[4] W. R. Ferrell, "Delayed force feedback, " Human Factors, pp. 449–455, 1966.

[5] J. Funda et al., "Teleprogramming: Toward delay-invariant remote manipulation, "PRESENCE, Teleoperators, Virtual Environ., vol. 1, no. 1, pp. 29–44, 1992.

[6] C. M.Gewertz, "Synthesis of a finite, four-terminal network from its prescribed driving-point function and transfer function, "J. Math. Phys., vol. 12, pp. 1-257;January, 1933.

[7] B. Hannaford, " A Design Framework for Teleoperators with Kinesthetic Feedback", *IEEE Trans. Robot. Autom.*, vol. 5, no. 4, pp. 426–434, 1989.

[8] G. Hirzinger et al., "Sensor-based space robotics.ROTEX and its telerobotic features, " IEEE Trans. Robot. Automat., vol. 9, pp. 649–663, Oct. 1993.

[9] P. Hokayem and M. W. Spong, " Bilateral teleoperation: An historical survey, " Automatica, vol. 42, pp. 2035-2057, 2006. Conf. Robotics and Automation, 2001, pp. 1031–1038.

[10] H. Kawada, T. Nakerikawa,"Bilateral Control of Nonlinear Teleoperation with Time Varying Communication Delays" *Proceedings, American Control Conference*, pp. 189–194, 2008.

[11] W. S. Kim et al., "Force reflection and shared compliant control in operating telemanipulators with time delay, " IEEE Trans. Robot. Automat., vol. 8, pp. 176–185, Apr. 1992.

[12] K. Kosuge et al., "Bilateral feedback control of telemanipulators via computer network, "in Proc. IEEE/RSJ Int. Conf. Intelligent Robots and Systems, 1996, pp. 1380–1385.

[13] T. Kotoku, "A predictive display with force feedback and its application to remote manipulation system with transmission time delay, " in Proc. IEEE/RSJ Int. Conf. Intelligent Robots and Systems, 1992, pp. 239–246.

[14] C. A. Lawn and B. Hannaford, "Performance testing of passive communication and control in teleoperation with time delay, " in Proc. IEEE Int. Conf. Robotics and Automation, vol. 3, 1993, pp. 776–783.

[15] D. A. Lawrence, "Stability and Transparency in Bilateral Teleoperation," *IEEE Trans. Robot. Autom.*, vol. 9, no. 5, pp. 624–637, 1993.

[16] D. Lee and M. W. Spong, "Passive Bilateral Teleoperation with Constant Time Delay," *IEEE Trans. Robotics*, vol. 22, no. 2, pp. 269–281, 2006.

[17] G. M. H. Leung, Bruce A. Francis, and Jacob Apkarian, "Bilateral controller for teleoperators with time delay via μ-synthesis," *IEEE Trans. Robot. Autom.*, vol. 11, no. 1, pp. 105–116, 1995.

[18] F. B. Llewellyn, "Some Fundamental Properties of Transmission Systems," *Proc. IRE*, vol. 40, pp. 271–283, 1952.

[19] Y .Murotsu, K .Senda, A .Mitsuya, K .Yamane, T .Nunohara"Theoretical and experimental Studies for Continuous Path Control of Flexible Manipulator Mounted on a Free-Flying Space Robot," *Proceedings, AIAA Guidance, Navigation and Control Conference AIAA-93-3863*, pp. 1458–1471, 1993.

[20] G. Niemeyer and J. J. E. Slotine, "Designing force-reflecting teleoperators with large time delays to appear as virtual tools, "in Proc. IEEE Int. Conf. Robotics and Automation, 1997, pp. 2212–2218.

[21] G. Niemeyer and J. J. E. Slotine, "Stable Adaptive Teleoperation," *IEEE J. of Ocean. Eng.*, vol. 16, no. 1, pp. 152–162, 1991.

[22] G. Niemeyer and J. J. E. Slotine, "Towards Force-Reflecting Teleoperation Over the Internet," in *Proc. IEEE Int. Conf. Robotics and Automation* pp. 1909–1915, 1998.

[23] G. Niemeyer and J. J. E. Slotine, "Telemanipulation with Time Delays," *Int. J. of Robotics Res.*, vol. 23, no. 9, pp. 873–890, 2004.

[24] E. Nuno, R. Ortega, N. Barabanov, and L. Basanez, "A Globally Stable PD Controller for Bilateral Teleoperators," *IEEE Trans. Robot.*, vol. 24, no. 3, pp. 753–758, 2008.

[25] E. Nuno, R. Ortega, and M. Spong, "Position Tracking for Non-linear Teleoperators with Variable Time Delay," *Int. J. Robitics Res.*, vol. 28, no. 7, pp. 895–910, 2009.

[26] E. Nuno, L. Basanez, and M. Prada, "Asymptotic Stability of Teleoperators with Variable Time-Delays," *Proceedings, IEEE Int. Conference on Robotics and Automation*, pp. 4332–4337, 2009.

[27] E. Nuno, L. Basanez, and R. Ortega, "Passivity-based control for bilateral teleoperation: A tutorial," *Automatica*, vol. 47, pp. 485–495, 2011.

[28] R. Oboe and P. Fiorini, "A Design and Control Environment for Internet-Based Telerobotics," *Int. J. Robotics Res.*, vol. 17, no. 4, pp. 433–449, 1998.

[29] L. F. Penin, K. Matsumoto, and S. Wakabayashi, "Force reflection for time-delayed teleoperation of space robots, "in Proc. IEEE Int. Conf. Robotics and Automation, 2000, pp. 3120–3125.

[30] L. F. Penin and K. Matsumoto, "Teleoperation with Time Delay.A Survey and its Use in Space Robotics, "Nat. Aerosp. Lab., Tokyo, Japan, Rep. TR-1438T, 2002.

[31] G. Raju, G. Verghese, T. Sheridan, "Design Issues in 2-port Network Models of Bilateral Remote Manipulation," *Proceedings, IEEE Int. Conference on Robotics and Automation*, pp. 1316–1321, 1989.

[32] G. Sankaranarayanan, B. Hannaford,"Experimental Comparison of Internet Haptic Collaboration with Time-Delay Compensation Techniques" *Proceedings, IEEE Int. Conference on Robotics and Automation*, pp. 206–211, 2008.

[33] C. Seo, J-P. Kim, J. Kim, H. Ahn, J. Ryu,"Robustly stable bilateral teleoperation under time-varying delays and data losses: an energy-bounding approach" *Journal of Mechanical Science and Technology*, Vol. 25, Issue. 8, pp. 2089–2100, 2011.

[34] T. Sheridan, "Telerobotics," Automatica, vol. 25, no. 4, pp. 487–507, 1989.

[35] T. Sheridan, "Space Teleoperation Through Time Delay: Review and Prognosis," *IEEE Trans. Robot. Autom.*, vol. 9, no. 5, pp. 592–606, 1993.

[36] Y. Tsumaki et al., "Virtual-reality-based teleoperation which tolerates geometrical modeling errors, " in Proc. IEEE/RSJ Int. Conf. Intelligent Robots and Systems, 1996, pp. 1023–1030.

[37] Y. Tsumaki et al., "Verification of an advanced space teleoperation system using internet, "in Proc. IEEE/RSJ Int. Conf. Intelligent Robots and Systems, 2000, pp. 1167–1172.

[38] Y. Yokokohji, Y. Iida, and T. Yoshikawa, "Toy problem as the benchmark test for teleoperation systems, " Adv. Robot., vol. 17, no. 3, pp. 253–273, 2003.

Published papers by the author

[1] T. Imaida, Y. Yokokohji, T. Doi, M. Oda, T. Yoshikawa, "Ground.space bilateral teleoperation experiment using ETS-VII robot arm with direct kinesthetic coupling, " *in Proc. IEEE Int. Conf. Robotics and Automation*, 2001, pp. 1031–1038.

[2] T. Imaida, Y. Yokokohji, T. Doi, M. Oda, T. Yoshikawa, "Ground-Space Bilateral Teleoperation of ETS-VII Robot Arm by Direct Bilateral Coupling under 7-sec Time Delay Condition," *IEEE Trans. Robot. Autom.*, vol. 20, no. 3, pp. 499–511, 2004.

[3] T. Imaida, K. Senda,"Performance improvement of the PD-based bilateral teleoperators with time delay by introducing relative D-control" *Advanced Robotics* , vol. 29, no. 6, pp.385–400, 2015.

[4] T. Imaida, K. Senda,"Performance improvement of PD-based bilateral teleoperator with time delay by introducing high pass

fillter "*Robotica* (submitted).

[5] Y. Yokokohji, T. Imaida, T. Yoshikawa,"'Bilateral Control with Energy Balance Monitoring under Time-Varying Communication Delay, " *in Proc. IEEE Int. Conf. Robotics and Automation*, 2000, pp. 2684–2689.

[6] Y. Yokokohji, T. Imaida, Y. Iida, T.Doi, M. Oda, T. Yoshikawa,"'Bilateral Teleoperation: Toward Fine Manipulation with Large Time Delay, " *in Proc. Int. Symposium on Experimental Robotics*, 2000, pp. 11–20.

[7] Y. Yokokohji, T. Imaida, T. Yoshikawa,"'Bilateral teleoperation under time-varying communication delay, " *in Proc. Int. Conf. on Intelligent Robots and Systems*, 1999.